Universitat
de les Illes Balears

DOCTORAL THESIS

2022

LAGRANGIAN TRANSPORT OF SINKING PARTICLES. FROM THEORETICAL CHARACTERIZATION TO OCEANIC APPLICATIONS

Rebeca de la Fuente Marañón

Universitat
de les Illes Balears

DOCTORAL THESIS

2022

Doctoral Programme in Physics

LAGRANGIAN TRANSPORT OF SINKING PARTICLES. FROM THEORETICAL CHARACTERIZATION TO OCEANIC APPLICATIONS

Rebeca de la Fuente Marañón

Thesis Supervisor: Cristóbal López Sánchez

Thesis Supervisor:: Emilio Hernández García

Thesis Tutor: Raúl Toral Garcés

Doctor by the Universitat de les Illes Balears

List of publications

- de la Fuente, R., Drótos, G., Hernández-García, E., López, C., and van Sebille, E.: Sinking microplastics in the water column: simulations in the Mediterranean Sea, Ocean Science. 17, 431-453, https://doi.org/10.5194/os-17-431-2021, 2021.
- de la Fuente, R., Drótos, G., Hernández-García, E., and López, C. (2021a). Network and geometric characterization of three-dimensional fluid transport between two layers. Phys. Rev. E, 104:065111.

Acknowledgements

I want to thank my two directors Cristóbal López and Emilio Hernández-García for giving me the opportunity of doing this doctoral thesis and also Gábor Drótos for supporting me during all the trajectory of this work.
I also acknowledge the financial support no. BES-2016-078416 under the FPI program of MINECO, and the Agencia Estatal de Investigación (AEI) and the European Regional Development Funds (ERDF) for their support to the project MDM-2017-071, Maria de Maeztu Program for Units of Excellence in R&D.

Abstract

The vertical transport of particles plays a key role in the major mechanisms driving biogeophysical cycles in the ocean and contributes to the distribution of pollulants and its accumulation on the ocean bottom. Most of theoretical models analyzing the global patterns of ocean circulation are restricted to surface waters. While available data from satellite altimetry and sediment traps are scarce below surface waters, Lagrangian particle tracking over the three-dimensional space may cover some gaps in our knowledge and better address future experimental research. The aim of this thesis is to analyze the vertical transport of particles in the ocean with tools of Statistical Physics and Dynamical Systems, and by providing a theoretical characterization of transport for particles that are inmersed in a three-dimensional fluid and travel in a preferential direction of motion.

We start analyzing the vertical dispersion and distribution properties of idealized sinking microplastics in the Mediterranean sea. As a first step, we determine the dynamics describing the motion of typical microplastics and evaluate the importance of physical effects such as inertia, Coriolis force, small-scale turbulence and variable seawater density. As a second step, we apply the dynamical equations of motion to negatively buoyant rigid microplastics that sink from the sea surface and calculate their amount and distribution along the water column.

Next, we develop a general formalism to study transport structures of particles that move in a preferential direction. The three-dimensional structures of transport given by the so-called *Lagrangian Coherent Structures* are commonly analyzed from cross-sections as they intersect at specific layers. However, few measurements have been developed characterizing the Lagrangian motion of particles depending on spatial distances instead of time. To aim at this, we characterize the Lagrangian transport of sinking particles traveling between horizontal layers located at different depths of the flow domain. Consequently, the derived formalism is applied to particles that are released from one layer and reach a second one due to their sinking motion. We define a two-layer map describing the transport of particles between layers, and apply concepts from dynamical systems and network theory to analyze the structures behind the two-layer map. We define a novel measure, the

Finite Depth Lyapunov Exponent, which quantifies the horizontal dispersion of particles when traveling between two layers. This geometrical description is heuristically related to network measures, such as degrees and entropies associated to the two-layer map. Numerical results are obtained by using an analytic three-dimesional flow with chaotic behaviour: a modified version of the ABC flow, imposing fluid particles to travel in a preferential direction.

Finally, we apply the transport characterization between layers to sinking particles that are released from the ocean surface in the Canary Islands basin. Horizontal dispersion and connectivity between layers are analyzed from quantifiers previously developed. We also compare and analyze global properties when varying the settling velocity and the depth of the bottom layer. Furthermore, both layers are partitioned into almost isolated regions identified from a community detection algorithm. The resulting subdomains are characterized by low interconnectivity between them and high internal mixing.

Resumen

El transporte vertical de partículas desempeña un papel fundamental en los principales mecanismos que impulsan los ciclos biogeofísicos en el océano y contribuye a la distribución de contaminantes y a su acumulación en el fondo oceánico. La mayoría de los modelos teóricos que analizan los patrones globales de la circulación oceánica se limitan a las aguas superficiales. Mientras los datos disponibles procedentes de la altimetría por satélite y de las trampas de sedimentos son escasos por debajo de las aguas superficiales, el estudio lagrangiano de partículas en el espacio tridimensional puede aumentar nuestro conocimiento y abordar mejor la investigación experimental. El objetivo de esta tesis es analizar el transporte vertical de partículas en el océano a partir de herramientas de física estadística y sistemas dinámicos, y proporcionando una caracterización teórica del transporte para partículas que están inmersas en un fluido tridimensional y viajan en una dirección preferente.

En primer lugar, analizamos las propiedades de dispersión y distribución vertical de microplásticos idealizados que se hunden en el mar Mediterráneo. Como primer paso, determinamos la dinámica que describe el movimiento de los microplásticos típicos y evaluamos la importancia de efectos físicos como la inercia, la fuerza de Coriolis, la turbulencia a pequeña escala y la densidad variable del agua de mar. Como segundo paso, aplicamos las ecuaciones dinámicas de movimiento a microplásticos rígidos que se hunden desde la superficie del mar y calculamos la cantidad y distribución de las partículas a lo largo de la columna de agua.

En segundo lugar, desarrollamos un formalismo general para el estudio de las estructuras de transporte de las partículas que se mueven en una dirección preferente. Las estructuras tridimensionales de transporte dadas por las llamadas *Estructuras Coherentes Lagrangianas* caracterizan la estructura del movimiento que tiene lugar en un momento dado y son comúnmente analizadas a partir de cortes bidimensionales donde intersectan. Sin embargo, se han desarrollado pocas medidas que caractericen el movimiento lagrangiano de las partículas en función de distancias espaciales en lugar del tiempo. En esta dirección, caracterizamos el transporte lagrangiano de partículas que se hunden y viajan entre capas horizontales situadas

a diferentes profundidades del dominio del flujo. En consecuencia, el formalismo derivado es aplicado específicamente a partículas que se mueven desde una capa y alcanzan una segunda a lo largo de sus trayectorias debido a su movimiento de hundimiento. Definimos un mapa de dos capas que describe el transporte lagrangiano de partículas entre capas, y aplicamos conceptos de teoría de sistemas dinámicos y de redes para analizar las estructuras de transporte que hay detrás del mapa de dos capas. Definimos una medida novedosa, el Exponente de Lyapunov de Profundidad Finita, que cuantifica la dispersión horizontal de las partículas cuando viajan entre ambas capas. Además, esta descripción geométrica se relaciona heurísticamente con medidas de red, como grados y entropías, asociadas al mapa de dos capas. Los resultados numéricos se ilustran utilizando un flujo analítico tridimensional con comportamiento caótico: una versión modificada del flujo ABC, que impone a las partículas viajar en una dirección preferente.

Finalmente, aplicamos la caracterización del transporte entre capas a las partículas que se hunden tras liberarse desde la superficie del océano en la cuenca de las Islas Canarias. La dispersión horizontal y la conectividad entre capas se analizan a partir de los cuantificadores desarrollados previamente. También comparamos y analizamos las propiedades globales de la dinámica de las partículas al variar la velocidad de sedimentación y la profundidad de la capa de fondo. Además, ambas capas se dividen en regiones casi aisladas identificadas a partir de un algoritmo de detección de comunidades. Los subdominios resultantes se caracterizan por una baja interconectividad entre ellos y una elevada mezcla interna.

Resum

El transport vertical de partícules exerceix un paper fonamental en els principals mecanismes que impulsen els cicles biogeofísics en l'oceà i contribueix a la distribució de contaminants i a la seva acumulació en el fons oceànic. La majoria dels models teòrics que analitzen els patrons globals de la circulació oceànica es limiten a les aigües superficials. Mentre les dades disponibles procedents de l'altimetria per satèl·lit i de les trampes de sediments són escassos per sota de les aigües superficials, l'estudi lagrangià de partícules en l'espai tridimensional pot augmentar el nostre coneixement i abordar millor la recerca experimental. L'objectiu d'aquesta tesi és analitzar el transport vertical de partícules en l'oceà a partir d'eines de física estadística i sistemes dinàmics, i proporcionant una caracterització teòrica del transport per a partícules que estan immerses en un fluid tridimensional i viatgen en una direcció preferent.

En primer lloc, analitzem les propietats de dispersió i distribució vertical de microplàstics idealitzats que s'enfonsen en el mar Mediterràni. Com a primer pas, determinem la dinàmica que descriu el moviment dels microplàstics típics i avaluem la importància d'efectes físics com la inèrcia, la força de Coriolis, la turbulència a petita escala i la densitat variable de l'aigua de mar. Com a segon pas, apliquem les equacions dinàmiques de moviment a microplàstics rígids que s'enfonsen des de la superfície de la mar i calculem la quantitat i distribució de les partícules al llarg de la columna d'aigua.

En segon lloc, desenvolupem un formalisme general per a l'estudi de les estructures de transport de les partícules que es mouen en una direcció preferent. Les estructures tridimensionals de transport donades per les anomenades *Estructures Coherents Lagrangianes* caracteritzen l'estructura del moviment que té lloc en un moment donat i són comunament analitzades a partir de talls bidimensionals on intersecten. No obstant això, s'han desenvolupat poques mesures que caracteritzin el moviment lagrangià de les partícules en funció de distàncies espacials en lloc del temps. En aquesta direcció, caracteritzem el transport lagrangià de partícules que s'enfonsen i viatgen entre capes horitzontals situades a diferents profunditats del domini del flux. En conseqüència, el formalisme derivat és aplicat específicament a partícules que es mouen des d'una capa i arriben a una segona al llarg de les seves

trajectòries a causa del seu moviment d'enfonsament. Definim un mapa de dues capes que descriu el transport lagrangià de partícules entre capes, i apliquem conceptes de teoria de sistemes dinàmics i de xarxes per a analitzar les estructures de transport que hi ha darrere del mapa de dues capes. Definim una mesura nova, l'Exponent de Lyapunov de Profunditat Finita, que quantifica la dispersió horitzontal de les partícules quan viatgen entre totes dues capes. A més, aquesta descripció geomètrica es relaciona heurísticamente amb mesures de xarxa, com a graus i entropies, associades al mapa de dues capes. Els resultats numèrics s'il·lustren utilitzant un flux analític tridimensional amb comportament caòtic: una versió modificada del flux ABC, que imposa a les partícules viatjar en una direcció preferent.

Finalment, apliquem la caracterització del transport entre capes a les partícules que s'enfonsen després d'alliberar-se des de la superfície de l'oceà en la conca de les Illes Canàries. La dispersió horitzontal i la connectivitat entre capes s'analitzen a partir dels quantificadors desenvolupats prèviament. També comparem i analitzem les propietats globals de la dinàmica de les partícules en variar la velocitat de sedimentació i la profunditat de la capa de fons. A més, totes dues capes es divideixen en regions gairebé aïllades identificades a partir d'un algorisme de detecció de comunitats. Els subdominis resultants es caracteritzen per una baixa interconnectivitat entre ells i una elevada mescla interna.

Table of contents

Chapter 1

Introduction

1.1 Plan of the thesis

The focus of this doctoral thesis is to extend some well-known concepts from dynamical systems and network theory to analyze the transport structures present in the water column of the ocean. We consider cross-sections of the three-dimensional motion of particles as key elements to gather the essential information describing the dynamics along the vertical direction. In this Chapter we introduce the concepts that have served as the basis for the development of this thesis. In order to contextualize the results obtained from this work, an introduction is made to the general topics of fluid dynamics, dynamical systems and networks, as well as a brief description of the most important oceanic processes involved in the sinking of particles. The following chapters show the results obtained in this thesis, which are divided into two well differentiated parts. The first part is collected in Chapter 2, where we analyze the vertical dispersion and distribution of microplastic particles in the Mediterranean Sea. We first calculate the relevant terms in the dynamics of sinking microplastics, which allows us to quantify the amount and vertical distributions of microplastics on the water column. Appendices A, B and C provide specific analysis to support the methods that we use in Chapter 2. Specifically, in Appendix A we analyze the importance of considering a spherical shape in idealized particles. In Appendix B, we quantify the effect of different physical terms in the dynamics of sinking particles, and Appendix C analyzes the effect of the bathymetry on the vertical dispersion of particles. The second part of this thesis develops a new formalism to analyze the vertical structure of motion and a preliminary application to the Canary Islands basin. In particular, in Chapter 3 we characterize transport properties of sinking particles travelling between horizontal surfaces located at different depths. A novel measure, the Finite Depth Lyapunov Exponent (FDLE), is defined for analyzing dispersion and mixing properties of particles while sinking, and is heuristically related to a coarse-graining version

of transport. In Chapter 4 we apply the formalism to a realistic ocean model in the Canary Islands basin in order to identify horizontal barriers to transport, mixing patterns of sinking particles and connectivity properties through community detection methods. Appendix D provides a mathematical description of the different geometrical processes involved in the transport between two given layers. Finally, we gather the main conclusions that can be drawn from this work and identify future perspectives.

1.2 Lagrangian transport in three dimensional flows

1.2.1 The Lagrangian perspective

Fluid motion can be analyzed from two different perspectives. In the Eulerian description, fluid properties are functions of space and time. It is a field description, so fluid properties such as density and velocity are mathematically represented as $\rho(\boldsymbol{r},t)$ and $\boldsymbol{u}(\boldsymbol{r},t)$, respectively. On the other hand, the Lagrangian description of the flow follows individual particle trajectories. From this perspective, flow properties are determined by tracking the motion of particles as they evolve in time, so the density and velocity of particles are represented as $\rho_p(t)$ and $\boldsymbol{u}_p(t)$.

The Eulerian and Lagrangian descriptions of the flow velocity are related as:

$$\begin{aligned} \frac{d\boldsymbol{r}}{dt} &= \boldsymbol{u}(\boldsymbol{r},t), \\ \boldsymbol{r}(t_0) &= \boldsymbol{r}_0, \end{aligned} \tag{1.1}$$

where t denotes time and $\boldsymbol{r}(t)$ is the time-evolving position of a particle starting from the initial location $\boldsymbol{r}(t_0)$ at time t_0. We can recover the Lagragian description from the Eulerian by solving the differential equation that relates both interpretations (1.1).

Streamlines and pathlines are used in the visualization of the fluid flow. Streamlines are the curves tangent to the velocity field and show the direction of motion of a fluid particle at any point, whereas pathlines are the individual trajectories followed by particles when moving from one point to the next. The velocity at a path is determined by the streamlines of the flow at each time, but streamlines and pathlines only coincide in steady flows for which streamlines do not change with time.

The material derivative is a Lagrangian concept defined as the rate of change of some property following the fluid particle with time. By expressing the material derivative in terms of the spatial location of particles, the relation between the time derivatives within each description of motion is expressed as:

$$\underbrace{\frac{D}{Dt}}_{\text{Lagrangian}} = \underbrace{\frac{\partial}{\partial t} + \boldsymbol{u} \cdot \nabla}_{\text{Eulerian}}, \tag{1.2}$$

which allows us to apply the conservation laws in the Eulerian description.

We adopt the Lagrangian description of the flow because it provides a natural framework for analyzing transport properties in real-world flows where connectivity and sensitivity to initial conditions are hidden from the Eulerian point of view.

1.2.2 Dynamical Systems

Dynamical systems theory is the mathematical branch used to describe the state evolution of a system according to fixed rules, so fluid transport is well described in this framework by analyzing the Lagrangian evolution of fluid particles from Eq. (1.1). Trajectories are the corresponding solutions of the equation, so the evolution of each initial condition $\boldsymbol{r}(t_0) = \boldsymbol{r}_0$ traces the trajectory of a fluid particle, where $\boldsymbol{r}(t)$ represents the state of the system at time t. There is no general analytic method for solving equation (1.1). However, some dynamical system methods to analyze such systems exist, which are fundamentally different for time-dependent flows.

Most of the developed techniques assume a time-independent velocity field, referred as steady flows. In this case, streamlines and pathlines coincide and transport structures are well described by dividing the domain into regions of qualitatively different dynamical behavior. Flow patterns reveal idealized motions because each location has a unique trajectory crossing it, which allows us to analyze the flow geometry by identifying the invariant manifolds of the fixed points. The mathematical concept of a manifold is the abstraction of a n-dimensional space. Manifolds are spaces with similar characteristics in all their points, i.e, the local description around a point is analogous to the local description around any other point on the manifold, and to the local description of the euclidean n-dimensional space. In other words, the neighbourhood of each point of the manifold can be interpreted as a n-dimensional ball. Invariant manifolds are topological manifolds that are invariant under the action of the dynamical system. This means that any trajectory starting on the invariant manifold will remain on the manifold. Among all invariant manifolds, the stable and unstable ones

are crucial for idenfying the global structures of motion. A fixed point **r** is a point such that $\boldsymbol{u}(\boldsymbol{r}) = 0$, so the stable manifold of a fixed point is the set of all points that approach the fixed point as times goes to infinity forward in time and the unstable manifold is the set of all points that approach the fixed point as times goes to infinity backwards in time. The fixed points where both types of manifolds intersect are called hyperbolic fixed points. Because stable and unstable manifolds remain invariant under the flow and separate regions of different dynamical behavior, they are usually called separatrices (Hernández-Carrasco, 2013, Bettencourt, 2014). Nearby initial points located at each side of the stable manifold will diverge at the hyperbolic point due to the effect of the unstable manifold coming out of the hyperbolic point. Similarly, if time goes backwards, nearby points on either side of the unstable manifold will diverge at the hyperbolic point in the direction of the stable manifold. However, we are interested in analyzing flow structures of time-dependent dynamical systems where classical methods do not apply. Idealized structures characterized by invariant manifolds do not exist in real-world systems, so different approaches are generally adopted to find structures in atmospheric and oceanic flows (Haller, 2015). One approach consists in identifying similarities with idealized structures from steady analytical flows (Ottino and Ottino, 1989, Wiggins, 2013, 2005, Samelson and Wiggins, 2006). Other approach goes one step ahead and defines the idealized structures heuristically from geophysical models coupled with data and compares the results with real-life patterns (Provenzale, 1999, Boffetta et al., 2001, Peacock and Dabiri, 2010, Samelson, 2013). These two approaches focus on known idealized structures and try to locate them in aperiodic systems, so both can be interpreted as an extension of the traditional methods to identify stable and unstable manifolds in unsteady systems. Such techniques provide a practical application in some cases, but have inherent limits when the dynamical system is only known for a finite time interval, which is the typical case for geophysical models or approximations to the Navier-Stokes equation. Unsteady flows also divide the domain into regions of different dynamical behavior. However, these regions move with time, so separatrices in unsteady flows lose their analogy with invariant manifolds. The third approach consists in identifying such separatrices arising from the exact dynamics. In unsteady flows fluid particles do not necessarily follow instantaneous streamlines, so the phase space does not contain points that decay to hyperbolic fixed points, but rather there exists points that decay to hyperbolic trajectories that move with time. Therefore, these trajectories appear to be robust to transport and act as time-dependent separatrices, defined as the Lagrangian Coherent Structures (LCS) that form the skeleton of fluid motion. In particular, the LCSs define the repelling and attracting material curves of the flow (Haller, 2015, Shadden et al., 2005, Haller, 2001).

Locating these LCSs require the knowledge of the stability of the flow, so different approaches have been developed to identify them. One geometrical method identifies lines or surfaces that separate fluid regions of different dynamical behavior (M. Mancho et al., 2003). On the other hand, these structures can be identified from the fact that advection of individual particles exhibit sensitivity to initial conditions, computed from Lyapunov exponents or related Lagrangian descriptors (Haller, 2001, Shadden et al., 2005). Under some conditions, maximal values of Lyapunov exponents form ridges that are related to the LCSs. Other approach focuses on the statistical properties of the flow from a coarse-graining version of the phase space, the so-called set-oriented methods (Froyland and Dellnitz, 2003, Dellnitz et al., 2001). Dispersion and mixing properties of real-world flows can be characterized from these approaches.

1.3 Lyapunov Exponents

Chaotic advection is a phenomenon described by dynamical systems theory. A trajectory is said chaotic if it shows sensitivity to initial conditions, i.e, if infinitesimal neighboring points diverge exponentially with time. Given a point $\boldsymbol{r}(t_0)$ and the perturbation $\delta\boldsymbol{r}(t_0)$, the classical Lyapunov exponent is defined as

$$\lambda = \lim_{t \longrightarrow \infty} (\lim_{\delta\boldsymbol{r}(t_0) \longrightarrow 0} \frac{1}{t} log \frac{|\delta\boldsymbol{r}(t)|}{|\delta\boldsymbol{r}(t_0)|}). \tag{1.3}$$

Stable solutions of dissipative or non-conservative systems have negative Lyapunov exponents. On the other hand, positive values are indicators of chaotic motion. Because the Lyapunov exponent is theoretically defined in the asymptotic limit, it measures the global predictability of a system. In practice, its value can be approximated for large enough integration times if nearby trajectories do not scape from the chaotic regime and these perturbations remain within the validity of linearization. However, it usually happens that the flow velocity of real-world systems is only known for a time interval or it becomes an intractable problem from a computational point of view. In such cases, we may be interested in the local predictability around points in space. The local Lyapunov exponent characterizes stretching rates of trajectories for a finite time interval. As a local measure, it defines a function of space and time, and becomes a field measure. Two types of local Lyapunov exponents has been defined, the Finite-Size Lyapunov Exponent (FSLE) and the Finite-Time Lyapunov Exponent (FTLE).

1.4 Finite-Time Lyapunov Exponent

The Finite-Time Lyapunov Exponent characterizes the exponential growth rate of perturbations for a given finite integration time (Lacorata et al., 2001). Starting from the velocity field (1.1), the flow map $\phi_{t_0}^{\tau}(\boldsymbol{r}_0)$ is obtained by integrating the equation from the initial condition $\boldsymbol{r}_0$ at t_0 for a given integration time τ:

$$\phi_{t_0}^{\tau}(\boldsymbol{r}_0) = \boldsymbol{r}(t_0+\tau), \tag{1.4}$$

which gives the position of the fluid particle at time $t_0+\tau$. The application of the flow map to a compact fluid region $M(t_0) \subseteq S$ located in the fluid domain S results in the defomation of such fluid material evolving under the flow. This mapping funcion $M(\tau) = \phi_{t_0}^{\tau}(M(t_0))$ requires the integration of trajectories for each fluid particle in the set $M(t_0)$, where the corresponding vectors $\boldsymbol{y}$ of the tangent space $T_xM(t_0)$ are deformed locally along its trajectory under the evolution of the variational equation:

$$\dot{\boldsymbol{y}} = \nabla \boldsymbol{u}(\boldsymbol{r}(t))\boldsymbol{y}. \tag{1.5}$$

Assuming the smoothness of the flow velocity $\boldsymbol{u}(\boldsymbol{r},t)$, the Jacobian matrix of the flow $\boldsymbol{J} = \nabla\phi_{t_0}^{t}(\boldsymbol{r}_0)$ is an invertible matrix, solution of the variational equation (1.5), $\dot{\boldsymbol{J}} = \nabla \boldsymbol{u} \cdot \boldsymbol{J}$, with $\nabla\phi_{t_0}^{t_0}(\boldsymbol{r}_0) = I$. The geometrical interpretation of the equation is given by the growth of initially nearby particles along their trajectories, such that infinitesimal perturbations $\delta\boldsymbol{r}(t_0)$ of a point $\boldsymbol{r}_0$ evolve according to the Eq (1.5) as $\delta\boldsymbol{r}(t) = \boldsymbol{\nabla}\phi_{t_0}^{t}(r_0)\delta\boldsymbol{r}(t_0)$.

The Cauchy-Green strain tensor is the symmetric and definite positive matrix:

$$C(\boldsymbol{r}_0) = (\nabla\phi_{t_0}^{\tau}(\boldsymbol{r}_0))^T \nabla\phi_{t_0}^{\tau}(\boldsymbol{r}_0), \tag{1.6}$$

whose eigenvalues χ_i and corresponding eigenvectors ξ_i satisfy

$$C\xi_i = \chi_i\xi_i,\ |\xi_i| = 1, i = 1,...,n \tag{1.7}$$

where n denotes the dimensionality of space (Haller, 2015, Shadden et al., 2005). The eigendirections are orthogonal to each other and aligned with the normal basis of the tangent space, so the total number of eigenvalues equals the dimension n of the system. The singular values of $\nabla\phi$, $S_i = \sqrt{\chi_i}$, provide information about the ellipticity and hyperbolicity of trajectories. For incompressible flows, the total volume is conserved under chaotic advection, so $det(C) = \Pi_i S_i^2 = 1$. If $S_i = 1$ for all singular values, the trajectories are called elliptic, where local rotation takes place and no stretching happens. On the other hand, if $S > 1$ for

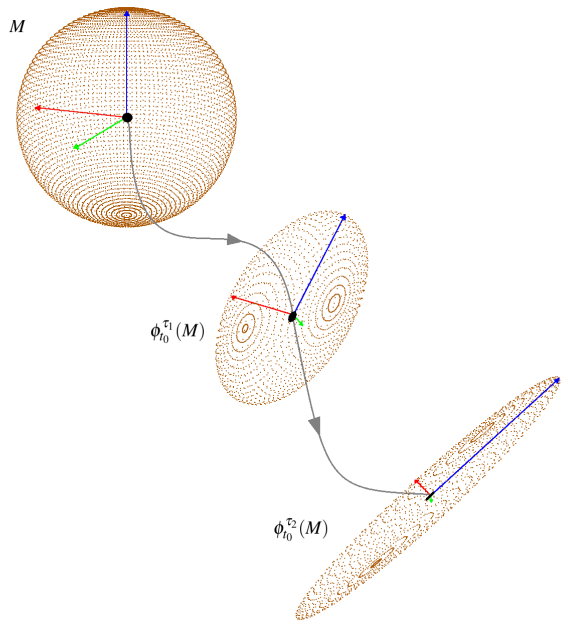

Fig. 1.1 Stretching of fluid material under the evolution of the flow map.

some singular value, the fluid material initially aligned with this eigendirection becomes stretched. In a n-dimensional system, the spectrum of singular values can be ordered as $0 < S_n \leq ... \leq S_2 \leq S_1$.

In Figure 1.1 we can look at the geometrical interpretation of the stretching factors given by the square root of eigenvalues of the Cauchy-Green strain tensor. In a three-dimensional space, an initial small sphere around $\boldsymbol{r}_0$ advected by an incompressible flow is stretched in an ellipsoide, whose principal axes are aligned with the vectors $\nabla\phi_{t_0}^{\tau}\xi_i(\boldsymbol{r}_0)$. The length of these axis has grown $S_i = \sqrt{\chi_i(\boldsymbol{r}_0)}$ times the initial radius length. Thus, the singular values of the Jacobian matrix, S_i, are the stretching factors of the evolving material. In two dimensional incompressible flows, the geometrical interpretation is analogous but considering initial fluid circunferences around the center point $\boldsymbol{r}_0$. Stretching factors with $S < 1$ indicate contraction in the correspoding eigendirection, whereas $S > 1$ corresponds to positive stretching. Furthermore, in a n-dimensional incompressible flow, we are usually interested in the maximal stretching factor S_{max}, which is always greater or equal than one, and aligns to the eigendirection of maximal growth. Since this maximal value dominates the local stretching of the fluid material around a point, it allows the characterization of chaotic advection taking place locally around the point.

The local exponential growth rate of nearby trajectories defined by the Finite Time Lyapunov Exponent is:

$$\lambda(\boldsymbol{r}_0, t_0; \tau) = \frac{1}{|\tau - t_0|} log(S_{max}), \tag{1.8}$$

where S_{max} is the square root of the maximal eigenvalue of the Cauchy-Green strain tensor given by the evolution of the flow map $\phi_{t_0}^{\tau}(\boldsymbol{r}_0)$. It integrates the separation between trajectories, so the FTLE takes into account the effect of the dynamics even for time-dependent flows. Geometrically, lines grow by a factor $e^{\tau\lambda_1}$, areas by a factor $e^{\tau(\lambda_1+\lambda_2)}$ and volumes by a factor $e^{\tau(\lambda_1+\lambda_2+\lambda_3)}$.

1.5 Lagrangian Coherent Structures

The identification of LCSs is extensively analyzed for two-dimensional incompressible flows, where the coherent structures appear as thin filaments through the stability behavior of the flow (Haller and Yuan, 2000). This means that fluid patches located around the coherent structures experience local stretching and contraction according to the presence of repelling and attracting material lines in the flow. Although a detailed study of the stability of material lines is necessary to the identification of the LCSs, coherent structures can be located from different approaches (Haller, 2015). FTLEs serve as a first-order approach to compute the skeleton of motion in terms of infinitesimal deformation of material lines. From this perspective, the local extrema of the FTLE field appear as ridges related to repelling curves. This approach is also extended to three-dimensional flows. In this case, the LCSs are two-dimensional structures embedded in the 3D space, so new methods are required to identify such surfaces in a straightforward and efficient way. Most of the developed methods for analyzing the three-dimensional LCSs draw cross-sections of the full structures or apply projections onto two-dimensional surfaces (Sulman et al., 2013, Haller, 2015, Bettencourt et al., 2012, 2013, 2017).

1.6 Set-Oriented Methods

1.6.1 A statistical perspective

Concepts from dynamical systems theory can be extended to a statistical perspective in order to detect global features of the flow that are not sensitive to the unpredictability of the system. While FTLE is a geometrical approach that makes use of invariant manifolds, probabilistic techniques attempt to approximate the so-called invariant or almost-invariant sets in terms of

transition rates (Froyland and Dellnitz, 2003, Dellnitz et al., 2001). Furthermore, concepts from network theory can be applied to this representation level of the dynamics and detect the transport properties in terms of connectivity.

1.6.2 Lagrangian flow networks

The transport matrix provides a coarse-graining version of the flow from which different patterns of transport can be analyzed. This operator allows to define a network that connects fluid boxes in terms of their physical interchanges. In general terms, a complex network display non-trivial topological features of a system that can be described by nodes and connections between them (Girvan and Newman, 2002, Newman, 2010, Caldarelli, 2007). Here we focus on flow neworks, a directed graph where each edge represents transport of an amount of fluid between two boxes (Ser-Giacomi et al., 2015a).

The domain is divided into N regular fluid boxes $B_i, i = 1,...,N$ which corresponds to the nodes of the network. Here we focus on regular box sizes having the same amount of fluid, but this restriction can be modulated. A link between two nodes is established when there exists an exchange of fluid between their boxes. Let μ denote the Lebesgue measure. Applying the flow map to the fluid contained in each box, the proportion of fluid travelling from box B_i to B_j is given by the transition transport matrix:

$$\boldsymbol{P}_{ij}(t_0,\tau) = \frac{\mu(B_i \cap \phi_{t_0+\tau}^{-\tau}(B_j))}{\mu(B_i)}, \tag{1.9}$$

which is the discretized version of the Perron-Frobenius operator. It defines the links between boxes by estimating the amount of fluid travelling from box B_i to box B_j. The link is called directed since it defines the fluid transport with a directional preference. Thus, $P_{ij} = P_{ji}$ for undirected fluid networks, whereas P_{ij} corresponds to the fluid travelling from one box to another one. The weight of the link corresponds to the amount of fluid transported.

If the same amount of fluid is initialized at each box, then the transport matrix has non-negative elements and is row-stochastic:

$$\begin{aligned} \sum_{j}^{N} P_{ij}(t_0,\tau) = 1, \quad \forall i \\ P_{ij}(t_0,\tau) \geq 0, \end{aligned} \tag{1.10}$$

which gives a probabilistic interpretation of the fluid transport. Specifically, P_{ij} is the probability that a trajectory started in a random location in box B_i ends in box B_j. If the flow $\boldsymbol{u}(\boldsymbol{r},t)$ is incompressible, the fluid transport mantains the fluid content at each box unalterable and the matrix is also column-stochastic, $\sum_i^N P_{ij}(t_0,\tau) = 1, \ \forall j$.

For a numerical evaluation, the Lagrangian map $\phi_{t_0}^{\tau}$ is applied over all particles uniformly distributed along the domain, with N the number of released particles at each box proportional to the Lebesgue measure $\mu(B_i)$. The flow map applied over each box B_i gives the final location of particles at box i after being advected by the flow for a given integration time τ, so the estimation in terms of particles of the fluid travelling from box B_i to box B_j after the integration time τ is given by:

$$P_{ij} = \frac{\#\ particles\ travelling\ from\ box\ i\ to\ box\ j}{N}. \tag{1.11}$$

Each entry matrix P_{ij} provides information about the initial and final location of particles from a probabilistic point of view with a dependence on initial release time t_0 and integration time τ. The resulting matrix $P_{ij}(t_0,\tau)$ is the adjacency matrix of a weighted and directed network, with P_{ij} denoting the weight of the link from node i to node j. Also, the size box Δ used for the discretization of the domain may introduce numerical errors, so robust features arise when the box size is large enough to not be affected by the unpredictability of the system while capturing the essential dynamical structure of the flow. If one is interested in transport properties covering the intermediate steps within the full time interval $[t_0, t_0+\tau]$, a Markovian approach may be taken (Ser-Giacomi et al., 2015b).

1.6.3 Network measures

The transport matrix contains information whose properties can be analyzed from network measures. The binary description of the adjacency matrix is defined as

$$A_{ij} = \begin{cases} 1 & \text{if } P_{ij} > 0 \\ 0 & \text{if } P_{ij} = 0 \end{cases} \tag{1.12}$$

i.e, it defines directed and unweighted links if an exchange of fluid from box i to box j takes place. The degree of a node corresponds to the number of links that conect it to other nodes, so in terms of Lagrangian flow networks it measures properties of fluid dispersion and mixing. In the case of directed networks, the degree of a node is splitted in the outcoming and incoming flux, which provides different characteristics of the flow pattern. The out-degree of

a node i provides dispersion properties in terms of connectivity. It is defined as

$$K_{OUT}(i) = \sum_{j=1}^{N} A(t_0)_{ij}, \tag{1.13}$$

which gives the number of nodes receiving some fluid content from node i. On the other hand, the in-degree of a node i informs about mixing properties, and is defined as the number of nodes from which the node receives some fluid content:

$$K_{IN}(j) = \sum_{i=1}^{N} A(t_0)_{ij}. \tag{1.14}$$

In a previous study (Ser-Giacomi et al., 2015a), the degree of a node is heuristically related to the Lyapunov exponent. For sufficiently long integration time τ, fluid patches contained in boxes are stretched into thin filaments characterized by their length. Stretching of initial lines $dl(t_0)$ around x_0 are quantified by the FTLE

$$dl(t_0+\tau) = dl(t_0)e^{\tau\lambda(r_0,t_0;\tau)}, \tag{1.15}$$

and averaging over the different initial locations in a box, the final length of lines stretched by the flow map initially located at B_i is estimated to be

$$L(t_0+\tau) \approx \frac{1}{\Delta}\int_{B_i} dx_0 e^{\tau\lambda(r_0,t_0;\tau)}. \tag{1.16}$$

Restricting to a two-dimensional flow, and denoting as $A(t_0+\tau)$ the total area of boxes with fluid content of $\phi(B_i)$, the relationship is described analytically as

$$\begin{aligned} K_{OUT}(i) = \frac{A(t_0+\tau)}{\Delta^2} \approx \frac{L(t_0+\tau)\Delta}{\Delta^2} \\ = \frac{1}{\Delta^2}\int_{B_i} dr_0 e^{\tau\lambda(r_0,t_0;\tau)} = \langle e^{\tau\lambda(r_0,t_0;\tau)}\rangle_{B_i}. \end{aligned} \tag{1.17}$$

With this characterization, dispersion properties of the flow are naturally described by Lyapunov exponents and related to the coarse-graining version of the stretching factor. Note however that the description of flow patterns in terms of Lyapunov exponents and network theory is valid if the flow map is dominated by strain, which requires large enough integration times. On the other hand, box sizes and numerical estimations of the Lyapunov exponents require sufficiently small fluid elements to avoid folding effects or non-exponential growth behavior.

Finally, network entropies provide a generalization to the degree which takes into account the weight distribution of the links (Aurell et al., 1997). They are defined as

$$H^q(i) \equiv \frac{1}{(1-q)|\tau|} log(\sum_j^N P_{ij}^q), \tag{1.18}$$

and quantify the diversity of the amount of fluid received by nodes from node i. In the limit of q approaching zero, we recover a characterization of the amount of received fluid,

$$H^0(i) \equiv \frac{1}{\tau} log(K_{OUT}(i)). \tag{1.19}$$

For q approaching one, the first-order network entropy is

$$H^1(i) = -\frac{1}{\tau} \sum_j^N P_{ij} log P_{ij}. \tag{1.20}$$

All these network measures are defined for closed flows, where the transport matrix is row-stochastic. For open flows, particles may scape from the predefined domain, so we can recover the standard network measures by defining the out-strength of a node as

$$S(i) = \sum_j^N P_{ij}, \tag{1.21}$$

which allows us to define the row-stochastic transport matrix with a well defined probability:

$$Q_{ij} = \begin{cases} \frac{P_{ij}}{S_i} & \text{if } S(i) \neq 0\,, \\ 0 & \text{if } S(i) = 0\,. \end{cases} \tag{1.22}$$

Mixing and dispersion are naturally defined from this description of the flow.

1.6.4 Communities

Local connectivity describes the skeleton of transport from dynamical properties of flow particles, and defines boundary manifolds that divide the domain into regions of different dynamical behavior. The global structure of transport is also analyzed by identifying the breaking up of the fluid domain into regions that display high intraconnectivity patterns but low interconnectivity between them. In terms of lagrangian flow networks, communities are generally defined as a network partition with high connectivity between nodes of a community and a low connectivity between them. The community detection problem becomes an

optimization problem that requires a methodological setup to reduce the computationally large cost of exploring all possible configurations, even for small networks. Furthermore, the number and sizes of real-world communities are generally unknown parameters. However, the methods developed depend on a definition of community, the interpretation of which may vary. This is the main reason why there are different types of methods and perspectives on a practical level. We briefly explain in the following the most used in the literature.

Different methods for community detection have been developed. Most of these algorithms measure a given partition with an objective function (Newman, 2004b, Newman and Girvan, 2004, Girvan and Newman, 2002), such the Girvan-Newman algorithm (Newman, 2004b, Girvan and Newman, 2002) that identifies communities optimizing betweenness centrality measure, or modularity maximization (Newman, 2004b, Blondel et al., 2008), which searches the network partition that fits better to a model. Other approach considers communities as invariant sets of the dynamical system. In terms of lagrangian flow transport, the transport matrix provides a statistical description of the flow dynamics and allows the identification of communities as coherent sets. The idea behind this approach is to detect the global structure of the flow by identifying dynamically isolated regions that are robust to the unpredictability of the flow. The Perron-Frobenius operator provides the required information to determine which regions are isolated with similar dynamical behavior. Their boundaries are expected to occur at the invariant manifolds of the flow analyzed from the geometrically point of view. This approach requires the discretization of the fluid domain and applies concepts from network theory. Communities are sets of boxes B_i that act as invariant sets. In particular, a set $A = \cup_i B_i$ is called an almost-invariant set in the time interval $[t_0, \tau]$ if it satisfies

$$\rho(A) = \frac{\mu(A \cap \phi_{t_0+\tau}^{-\tau}(A))}{\mu(A)} \approx 1. \tag{1.23}$$

For almost-invariant sets, the probability of a trajectory to not scape from the region A is very high. Thus, almost-invariant sets are considered as coherent structures of the flow (Froyland and Dellnitz, 2003, Dellnitz et al., 2001, Haller, 2000). The community detection becomes an optimization problem of finding almost-invariant sets A_k with values of $\rho(A_k)$ maximized. Different algorithms have been developed in order to find such a partition. The spectral method computes the first singular vectors of the transport matrix, and performs a clustering to find regions of maximal invariance (Froyland and Padberg, 2009, Froyland et al., 2007).

Here we focus on the Infomap algorithm, that minimizes a cost function and finds a partition based on the connectivity of the transport matrix (Ser-Giacomi et al., 2015a).

Infomap optimises an objective function, the map equation, and finds the partition that best compresses the information of the flow transport (Bohlin et al., 2014). A set of random walkers describe trajectories moving throught the nodes with a probability proportional to the weighted links of the network. The idea behind this algorithm is that the random walkers will be retained in modules, so the trajectories will move inside closed regions for long times. Concepts from information theory are used to describe the movement of random walkers and quantify the minimal information required to describe the network partition. Trajectories of random walkers are described by a sequence of words representing the nodes they cross, and the information cost is defined as the total information required for a random walker to describe a given network partition. The map equation uses transition rates of the transport matrix as a modular description of the walker's trajectory. Thus, community detection consists in minimising the information cost trought the map equation over possible network patitions. The length of the codeword given in terms of transition rates is

$$L = q_{\curvearrowright} H(Q) + \sum_{\alpha=1}^{m} p_{\circlearrowright}^{\alpha} H(p^{\alpha}), \tag{1.24}$$

where m is the number of communities. Given a network partition, the length L gives the minimum amount of information required to describe the average length displacement of a random walker. The equation is described in terms of the Shannon entropy H, which measures the transition diversity between communities α

$$H(Q) = -\sum_{\alpha=1}^{m} \frac{q_{\alpha\curvearrowright}}{q_{\curvearrowright}} log_2(\frac{q_{\alpha\curvearrowright}}{q_{\curvearrowright}}), \tag{1.25}$$

where $q_{\alpha\curvearrowright}$ denotes the probability for a random walker to leave the community α and $q_{\curvearrowright} = \sum_{\alpha=1}^{c} q_{\alpha\curvearrowright}$ is the absolute probability of jumping between communities. The second term of equation 1.24 defines the Shannon entropy value of the codebook of module α, i.e, it measures the entropy associated to the words required to describe the trajectories of random walkers inside the community and the word describing a jump leaving the community:

$$H(P^{\alpha}) = -\sum_{i\in\alpha} \frac{\pi_i}{p_{\circlearrowright}^{\alpha}} log_2(\frac{\pi_i}{p_{\circlearrowright}^{\alpha}}) - \frac{q_{\alpha\curvearrowright}}{p_{\circlearrowright}^{\alpha}} log_2(\frac{q_{\alpha\curvearrowright}}{p_{\circlearrowright}^{\alpha}}), \tag{1.26}$$

with π_i denoting the stationary distribution of the random walkers and $p_{\circlearrowright}^{\alpha} = p_{\alpha\curvearrowright} + \sum_{i\in\alpha} \pi_i$. This description of a network partition from information theory allows to minimize the map equation and find such partition that optimizes the information required to describe random walks inside and between communities. In practice, infomap algorithm improves other methods because it does not require a predefined community size and is not contraint to

a minimum community size. Furthermore, communities are not necesarily of similar size. As an illustration, we show in Fig. 1.2 a community partition of the Mediterranean Sea analyzed in Ser-Giacomi et al. (2015a).

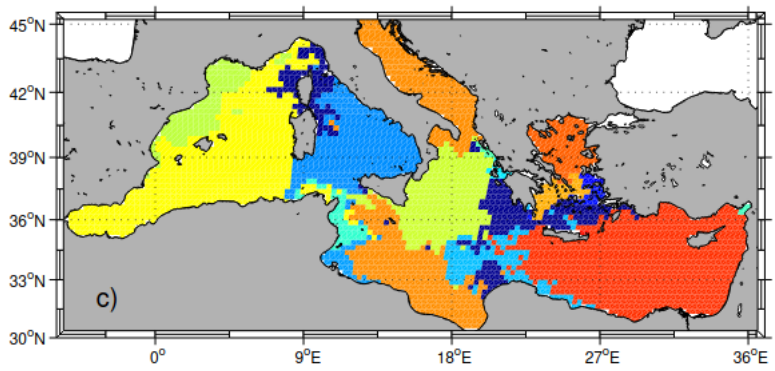

Fig. 1.2 Infomap partition of the Mediterranean Sea into communities after $\tau = 30$ days. (Source: Ser-Giacomi et al. (2015a))

1.7 Vertical transport of particles

1.7.1 Dynamics of inertial particles

Advection of finite-size particles is relevant in a variety of natural and engineering situations. In the ocean it plays a key role in the biogeophysical processes that allows the sustainability of life. Specifically, it plays a key role in natural phenomena such as primary production, marine aggregates, biological cycles or transport of pollulants. Particles are usually assumed to have negligible mass and size. In this case, the particle's velocity becomes identical to that of the fluid flow. Particles are passive tracers, with $\boldsymbol{r}(t)$ the particle's position, and satisfying the dynamical equation

$$\dot{\boldsymbol{r}}(t) = \boldsymbol{u}(r(t),t), \tag{1.27}$$

where $\boldsymbol{u}$ is the flow velocity. Tracer dynamics preserve volumes when the flow is incompressible and particles distribute homogeneously. Altough this assumption is a good approximation in some cases, it does not apply for finite-size particles where inertial forces do not allow instantaneous adaptation of the particle's velocity to that of the fluid (Maxey and Riley, 1983). In the latter case, particle dynamics is dissipative and transport can be described in terms of attractors dominated by regions with high accumulation rates.

Finite-size particle dynamics are well described by Navier-Stokes equation for moving boundaries. However, solving directly the partial differential equation presents some difficulties. Instead, the Maxey-Riley-Gatignol (MRG) equation (Maxey and Riley, 1983, Gatignol, 1983, Meccia et al., 2016, Cartwright et al., 2010) is an approximate differential equation that describes the motion of small spherical particles under some assumptions

$$\begin{aligned} m_p\dot{\boldsymbol{v}} = m_f\frac{D}{Dt}\boldsymbol{u}(\boldsymbol{r}(t),t) - \frac{1}{2}m_f(v - \frac{D}{Dt}[\boldsymbol{u}(\boldsymbol{r}(t),t) + \frac{1}{10}a^2\nabla^2\boldsymbol{u}(\boldsymbol{r}(t),t)]) \\ -6\pi a\rho_f\upsilon\boldsymbol{q}(t) + (m_p - m_f)\boldsymbol{g} - 6\pi a^2\rho_f\upsilon\int_0^t dt'\frac{d\boldsymbol{q}(t)/dt}{\sqrt{\pi\upsilon(t-t')}}, \end{aligned} \tag{1.28}$$

where a is the particle's radius, m_p its mass, and

$$\boldsymbol{q}(t) \equiv \boldsymbol{v}(t) - \boldsymbol{u}(\boldsymbol{r}(t),t) - \frac{1}{6}a^2\nabla^2\boldsymbol{u}. \tag{1.29}$$

The particle's velocity is denoted as $\boldsymbol{v}(t)$ and $\boldsymbol{u}(\boldsymbol{r}(t),t)$ is the flow velocity at particle's position $\boldsymbol{r}(t)$. m_f is the fluid mass displaced by the particle, υ the kinematic viscosity of the fluid. The fluid density is ρ_f, and $\boldsymbol{g}$ the gravitational acceleration. These terms represent different forces involved in the dynamics. The fluid acceleration is analytically described in the first right-hand side term and represents the force that the surrounding flow motion applies on the particle, disregarding the perturbation of the flow by the particle presence. The second term describes the added-mass effect from which an amount of fluid is displaced by particle's movement, and the two following terms describe the Stokes drag due to the fluid viscosity and the buoyancy force (Auton et al., 1988). Finally, the Basset-Boussinesq history term, associated to the vorticity diffusion. The term $a^2\nabla^2\boldsymbol{u}$ is the Faxén correction and accounts for the spatial variation of the flow around the particle (Faxén, 1922). The MRG equation is valid for particles with low Reynolds number, $Re_p = \frac{aW}{\upsilon} \ll 1$, where particle size represents the length scale and $W = |\boldsymbol{v} - \boldsymbol{u}|$ the velocity scale defined as the relative velocity between particle and the surrounding fluid. This implies that initial velocity differences between particle and the fluid must be small enough. Also, another condition for the equation validation is that the shear Reynolds number $Re = \frac{a^2U}{\upsilon L} \ll 1$ must be small, where L and U denote the characteristic length and velocity scales of the flow (Batchelor, 2000). This condition implies that typical gradients of the flow remain small.

The MRG equation can be simplified for very small particle sizes. Faxén corrections can be neglected if the typical length of the velocity field is much larger than particle's size. On the other hand, the Basset-Boussinesq term depends on the full history of the particle and may be difficult to compute in practise. Both terms are negligible under the assumption

$\frac{a}{\sqrt{\upsilon}} \ll 1$ (Maxey and Riley, 1983, Meccia et al., 2016, Haller and Sapsis, 2008), and the MRG equation simplifies to the ordinary differential equation

$$\frac{d\boldsymbol{v}}{dt} = \beta \frac{D\boldsymbol{u}}{Dt} + \frac{\boldsymbol{u} - \boldsymbol{v} + \boldsymbol{v}_s}{\tau_p}, \tag{1.30}$$

where $\beta = \frac{3\rho_f}{2\rho_p + \rho_f}$, with ρ_p, ρ_f denoting the particle and fluid densities, respectively. Particles denser than seawater have $\beta < 1$, whereas $\beta = 1$ for neutrally buoyant particles. The Stokes time, $\tau_p = \frac{a^2}{3\beta\upsilon}$, is the characteristic response time of the particle to changes in the flow, and the settling velocity is defined as $\boldsymbol{v}_s = (1-\beta)\tau_p \boldsymbol{g}$. This equation usually serves as a starting point for analyzing the dynamics of inertial particles of very small size, spherical shape and where interactions between particles are not taken into account (Maxey and Riley, 1983).

1.7.2 Typical sinking particles in the ocean

Vertical transport plays a key role in the major mechanisms driving biological cycles in the ocean and contributes to the distribution of pollulants and its accumulation on specific regions. Most of theoretical models analyzing the global scale patterns of ocean are restricted to the horizontal surface. However, there is a recent interest in the vertical structure of transport as it drives crucial biogeophysical processess involved in the sustainability of life. Until now, there are no sophisticated technologies that allow to collect experimental data in the full vertical domain, so available data from satellite altimetry and sediment traps are usually compared to theoretical models in order to fill gaps in our knowledge and better address experimental research (Buesseler et al., 2007). Taking into account the chemical composition of particles and their source, particles can be classified into biogenic particles (mostly composed by plankton, fecall pellets and marine snow) or polluting material, being polymer types of microplastics one of the most abundant.

1.7.3 Sinking biogenic particles

Marine biogeochemical cycles are the pathways of chemical elements travelling through the ocean. Although chemical elements have their cycles interconnected, the carbon cycle is one of the most studied as it forms the building block of life. In particular, a change in the carbon flux may have high impacts in ecosystems and climate. Carbon tends to enter the ocean as carbon dioxide and methane in a natural way. However, human activity has increased this greenhouse gas in the atmosphere due to the combustion of fossil fuel ((Stocker, 2014)). At least a quarter of this emitted CO_2 is taken up by the ocean. This is the reason why climate

change is usually analyzed from sensitiveness to dioxide of carbon sequestration that takes place in the ocean.

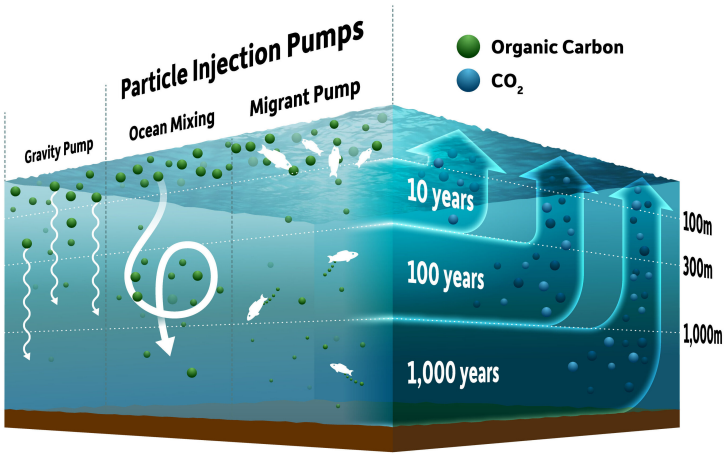

Fig. 1.3 Time scales of carbon storage through the vertical column. (Source: Michael Osadciw, University of Rochester.)

Carbon is introduced into the ocean as dissolved CO_2 or from phytosynthetic fixation. The process known as the Biological Carbon Pump describes the transport of carbon dioxide from the atmosphere to the deep ocean through biological activity, so the effect of the biological pump in the carbon cycle resides in the capacity for the microorganisms of taking carbon from the ocean surface and sequester it to the deep ocean as sediments. Marine organisms are involved in carbon transport and regulate the functionality of the carbon cycle through metabolic processes and chemical reactions. The depth to which the particles sink defines a time scale for their future return to the surface for its reuse, such that the deeper they go, the longer it takes for them to return to the surface (Passow and Carlson, 2012, Boyd et al., 2019). As illustrated in Fig. 1.3, carbon located at a scale of hundred meters takes about ten years to return to the atmosphere, whereas sinking particles reaching the deep ocean remain as a carbon storage for millenia before returning to the surface. There exists different processes by which carbon pump takes place, but also ocean mixing and its interaction with marine organisms play a key role (Honjo et al., 2014, Buesseler et al., 2007). The general pathways of the carbon cycle are schematized in Fig. 1.4. Along the euphotic zone, some organisms such as phytoplankton perform photosyntesis taking carbon dioxide from the ocean surface and generate organic matter, reducing the CO_2 from the surface and enhacing its absorption from the atmosphere. Part of this primary production is exported to the deep ocean as biogenic particles, being almost composed by dissolved organic carbon (DOC), fecal pellets and zooplankton as particulate organic matter (POC). Within a complex

food web interaction, zooplankton consumes organic carbon produced by phyplankton in the photosyntesis and transforms it into fecal pellets than sink very fast. These particles can be a new source of nutrients in the future through upwelling events. Therefore, the ocean regulates atmospheric CO_2 levels and prevents impacts from climate change. However, small changes in the carbon flux influence the oceanic storage capacity and may have impacts in the atmospheric CO_2 levels.

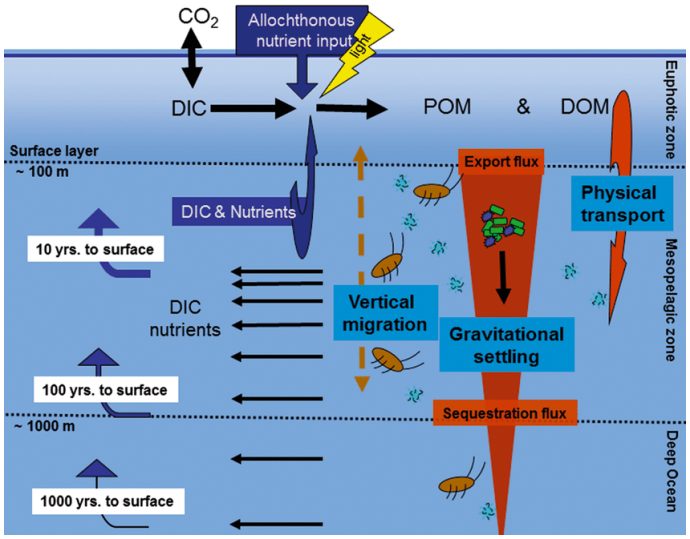

Fig. 1.4 Representation of the biological carbon pump. Source from (Passow and Carlson, 2012).

1.7.4 Sinking microplastics

Plastic has become indispensable in human life despite the fact that its accumulation in ecosystems generates devastating impacts on marine biota, biodiversity and human health (Solomon and Palanisami, 2016). There are different polymer types with different physical properties associated, mostly classfied as PET (Polyethylene Terephthalate), PP (Polypropylene), HDPE (High Density Polyethylene), LDPE (Low Density Polyethylene), VC (Polyvinyl) and PS (Polystyrene), so once disposed into the environment, risk assessment becomes a complex problem. Due to its physical and chemical properties, plastic is difficult to degrade by microorganisms and its duration in the environment can be extended from some years to centuries (Goldberg, 1997). In general, there are only two main mechanisms that lead to its degradation: mechanical abrasion, i.e, its erosion and fragmentation into smaller and smaller pieces, and degradation by exposure to UV rays from the sun light. Under the degradation

process, some scientists have already shown that plastic releases chemicals such as methane and ethylene, contribute as a powerful source of greenhouse gases.

From the beginning of its manufacturation in 1950, approximately 8 million tonnes of plastics end up in the oceans every year (Jambeck et al., 2015) and the annual production rate grows exponentially. It is estimated that only 2 % of the plastic produced closes the recycling cycle. A large amount is used for fossil fuels, while an estimated 32 % ends up into the environment. Plastic is a long-lived material with high resistance and low density, and its buoyancy makes it to be dispersed long distances. In general, it is transported by atmospheric factors ending at the ocean, mainly in coastal regions of high population density (Ivar do Sul et al., 2013, Jayasiri et al., 2013). The vast majority of plastic has a lower density than that of the water, so scientists believed that plastics remain floating on the ocean surface and were transported following the ocean currents of the surface. However, only 1% of the estimated plastic ending at the ocean was found at the surface (van Sebille et al., 2015, Choy et al., 2019), which led to a reconsideration of the processes involved in their transport. After an exhaustive research, some important processes has been identified, illustrated at Figure 1.5.

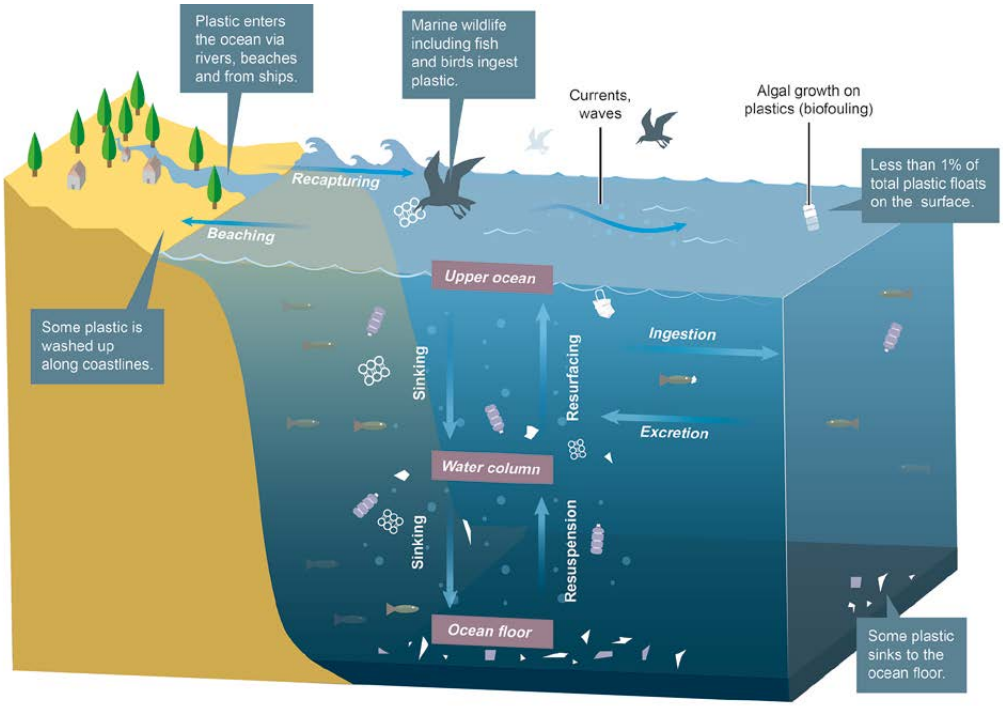

Fig. 1.5 Processes of plastic transport in the ocean. Source from (Van Sebille et al., 2016).

Plastic debris in aquatic environment are degraded until reaching a micro-size range. Microplastics are defined as such plastic particles with sizes smaller than 5mm (Kershaw

and Rochman, 2015), which has been identified in most aquatic habitats and along the water column (Ivar do Sul et al., 2013). The most important reported processes by which microplastics leave the ocean surface are beaching (Turner and Holmes, 2011), biofouling (Ye and Andrady, 1991, Chubarenko et al., 2016, Kooi et al., 2017), sinking (Erni-Cassola et al., 2019), wind-driven mixing or their introduction into the marine food web (Wright et al., 2013a,b). The technical complications for studying the distribution of subsurface microplastic takes us to a little known scenario. It is reported that wind-driven mixing generates an exponential decrease of pieces with depth. However, this vertical distribution only accounts for concentration rates of underway samples driven by wind, a few meters below the surface (Enders et al., 2015). High plastic concentrations are also reported in deeper waters, at 1000m depth in Monterey Bay, and at 2000 m below the North Pacific Garbage Patch, among many others (Choy et al., 2019, Thompson et al., 2004, Hidalgo-Ruz et al., 2012), and recent studies reveal continuous distribution of microplastic along the water colum (de la Fuente et al., 2021b).

Chapter 2

Sinking microplastics in the water column

2.1 Introduction

Approximately 8 million tonnes of plastics end up in the oceans every year (Jambeck et al., 2015). Nevertheless, only a very small percentage, around 1%, remains on the surface (van Sebille et al., 2015, Choy et al., 2019). The rest leaves the surface of the ocean (Ballent et al., 2013, van Sebille et al., 2020) through beaching (Turner and Holmes, 2011), biofouling (Ye and Andrady, 1991, Chubarenko et al., 2016, Kooi et al., 2017) or sinking (Erni-Cassola et al., 2019), but also wind-driven mixing presumably leads to an underestimation for the amount of particles remaining close to sea surface (Kukulka et al., 2012, Enders et al., 2015, Suaria et al., 2016, Poulain et al., 2018). The distribution of plastic pollution in the sea is poorly understood at present but would be crucial to properly evaluate the exposure of marine biota to this material, and formulate strategies for cleaning the oceans (Horton and Dixon, 2018).

Floating plastics and those that have beached or sedimented on the seafloor are relatively well studied through field campaigns (although explanation is missing for many findings; Andrady, 2017, Erni-Cassola et al., 2019, Kane and Clare, 2019). In contrast, the presence of plastics within the water column has received less attention, and many surveys in this realm are restricted to so-called underway samples, a few meters below the surface (e.g., Enders et al., 2015). However, e.g., Choy et al. (2019) reported that below the mixed layer and down to 1000 m depth in Monterey Bay, concentrations of plastics are larger than at the surface

The contents of this Chapter are based on de la Fuente et al. (2021b).

(Thompson et al., 2004, Hidalgo-Ruz et al., 2012). Egger et al. (2020) found more plastic between 5 m and 2000 m below the North Pacific Garbage Patch than at the surface. These findings turn out to mostly concern plastic pieces that, according to their nominal material density, would be classified as positively buoyant (Egger et al., 2020).

We focus on a certain class of plastic particles, negatively buoyant rigid microplastics, excluding very small size, and we estimate their vertical distribution through the water column and their amount in the Mediterranean Sea. Microplastic particles are among the most important contributors to marine plastic pollution (Arthur et al., 2009). Closely following the work of (Monroy et al., 2017) for sinking biogenic particles but choosing particle properties to correspond to those of negatively buoyant microplastics, we first justify the use of a simplified equation of motion, in which the plastic particle velocity is the sum of the ambient flow velocity and a sinking velocity depending on particle and water characteristics. In particular, we estimate the impact of some corrections to this simple dynamics and evaluate in detail the influence of the spatial variation of the seawater density on the plastic dispersion and sinking characteristics. For our Mediterranean case study, the impact of the varying seawater density on particle trajectories can be comparable to the estimated effect of the neglected small scales below the hydrodynamical model's resolution.

We then estimate the amount of microplastic particles in the water column of the open Mediterranean. Our estimates rely on a uniform vertical distribution, which is confirmed by our numerical simulations to be a good approximation for fast-sinking particles. This can be explained by a simple model in which released particles sink with a constant velocity. Detailed consideration of the transient dynamics identifies small non-Gaussian vertical dispersion around this simple sinking behavior, with transitions between anomalous and normal effective diffusion.

2.2 Types of microplastics in the water column

The dynamics and the fate of microplastics in the ocean are largely determined by their material density (Erni-Cassola et al., 2019). However, shape, size and rigidity are also relevant properties, characteristic transport pathways to the water column being different for different particle types.

Typically, positively buoyant plastic types will remain floating at the sea surface or close to it, and then will not contribute to the microplastic content in the water column, the topic we are interested in. However, it has been documented experimentally that biofouling may increase sinking rates of particles up to 81% and enhances sedimentation (Kaiser et al., 2017). So, a class of high abundance and mass may be represented by nearly neutrally buoyant

microplastic particles that are generated by biofouling (Ye and Andrady, 1991, Chubarenko et al., 2016) from positively buoyant plastic types or by other mechanisms of aggregation with organic matter, especially for small particle sizes (Kooi et al., 2017).

In fact, the fallout from the North Pacific Garbage Patch almost entirely consists of plastic types nominally less dense than water (Egger et al., 2020). Although some of these immersed particles finally reach the sea bottom, their proportion in sedimented plastic is minor except for the immediate vicinity of coasts where water is shallow. Most of these particles remain in the photic zone (Mountford and Morales Maqueda, 2019, Wichmann et al., 2019, Soto-Navarro et al., 2020). This suggests that reverse processes could also take place after biofouling and that the dynamics of such particles is complicated (Kooi et al., 2017, Erni-Cassola et al., 2019).

Particles denser than seawater dominantly accumulate at the sea bottom (Mountford and Morales Maqueda, 2019). A mechanism by which microplastics denser than water can also be present within the water column is the finite time taken by them to reach the bottom. Under continuous release at the surface and sedimentation at the bottom, the transient falling would lead to a steady distribution for the amount of plastic in the water column at any given time, and this distribution has never been estimated. Note that the Eulerian methodology of Mountford and Morales Maqueda (2019), treating sedimentation (i.e., deposition on the seafloor) by parametrization and thus leaving particles in the water column indefinitely long, is not suitable for this estimation. One aim is to explore this distribution by means of Lagrangian simulations.

There are different classes of microplastic particles denser than seawater. For example, dense synthetic microfibers have been found to strongly dominate in sediment samples far from the coast (Woodall et al., 2014, Fischer et al., 2015, Bergmann et al., 2017, Martin et al., 2017, Peng et al., 2018), and have been detected in large proportions in deep-water samples and sediment traps in the open sea as well (Bagaev et al., 2017, Kanhai et al., 2018, Peng et al., 2018, Reineccius et al., 2020). Mostly originating from land-based sources (Dris et al., 2016, Carr, 2017, Gago et al., 2018, Wright et al., 2020), it is not obvious to explain their abundance on abyssal oceanic plains (Kane and Clare, 2019). Maritime-activity sources (Gago et al., 2018) can contribute to that. Another reason could be that their special and deformable shape results in a strongly reduced settling velocity (Bagaev et al., 2017) that allows long distance horizontal transport (Nooteboom et al., 2020). In any case, it is difficult to estimate the amount of microfibers in the oceans due to sampling issues and to their absence from statistics of mismanaged plastic waste (Carr, 2017, Barrows et al., 2018), and we will not consider them. We also disregard films, which are only sporadically encountered in the open ocean (Bagaev et al., 2017) and thus have moderate importance.

We concentrate in the following on dense rigid microplastic particles. The most abundant particles of this class are fragments (e.g., Martin et al., 2017, Peng et al., 2018), which have an irregular shape, but their extension is usually comparable in the three dimensions. Experimental estimates for the settling velocities of irregular fragments or other nonspherical particles have suggested considerable deviations from values predicted by the Stokes law (Kowalski et al., 2016, Khatmullina and Isachenko, 2017, Kaiser et al., 2019), so that it is unclear how a precise full equation of motion should be constructed. For a qualitative exploration of particle transport through the water column, we will argue in Sect. 2.4.1 and App. A that the Maxey–Riley–Gatignol (MRG) equation (Maxey and Riley, 1983) should be appropriate for a reasonably wide range of such particles.

Whatever their precise equation of motion is, these sinking particles (directly detected by Bagaev et al. (2017) and Peng et al. (2018)) are thought to reach the seafloor relatively fast (Chubarenko et al., 2016, Kane and Clare, 2019, Soto-Navarro et al., 2020), landing within horizontal distances of tens of kilometers from their surface location of release (see Sect. 2.4.2 and App. B). One consequence of their fast sinking is the absence of almost any fragmentation after they leave the sea surface (Andrady, 2015, Corcoran, 2015), and the influence of biological processes on the particles' properties should also be moderate, leaving their size and shape intact during sinking. Note that, in contrast to the case of floating plastics (Kooi et al., 2017, Kvale et al., 2020), interaction of sinking plastics with particulate matter of biological origin appears to be moderate. This is according to the absence of a need to disassemble microplastic pieces from biological aggregates during sample processing as described by Bagaev et al. (2017). Note, however, that experimental results by Michels et al. (2018) indicate that aggregation with organic material might occur within a sufficiently short time at surface layers, which would likely lead to increased sinking velocities (Long et al., 2015). Transport by bottom currents (Kane and Clare, 2019, Kane et al., 2020) is important for explaining their distribution in sediments after coastal release. However, the statements above imply that the dense rigid microplastic content of samples from deep-sea trenches, abyssal plains (van Cauwenberghe et al., 2013, Fischer et al., 2015, Peng et al., 2018, Kane and Clare, 2019) must originate from sources at the surface of the open sea rather than from coastal inputs.

While methodological issues make the quantification of abundance difficult (Song et al., 2014, Andrady, 2015, Filella, 2015, Lindeque et al., 2020), negatively buoyant microplastic fragments have indeed been found in surface and near-surface samples of the open waters of the Mediterranean Sea (Suaria et al., 2016) and the Atlantic Ocean (Enders et al., 2015), respectively, from which they can contribute to microplastic content of the water column and deep-sea sediments (Fischer et al., 2015, Bagaev et al., 2017). Horizontal transport of these

particles can be carried out by marine organisms, and spontaneous attachment to pieces of positive buoyancy is a further possibility but is not yet discussed in the literature. Composite pieces of debris or those that contain trapped air (including foams in some cases) may also represent a source of microplastic ending at the water column (Andrady, 2015). However, most of such particles are presumably released by local maritime activity. An example of this are flakes of paint and structural material from boats and ships, which contain negatively buoyant alkyds and poly-(acrylate/styrene). Despite the particle's high density, large amounts of them may be found in the sea surface microlayer where surface tension keeps them floating (Song et al., 2014). The range of horizontal transport of these particles at the sea surface is unclear, but expected to be restricted to short distances because sinking from the sea surface microlayer is considerable, especially in waters disturbed by waves (Hardy, 1982, Stolle et al., 2010).

While the idea of Kooi and Koelmans (2019) to treat all plastic particles together by means of continuous distributions is appealing, the above considerations strongly favor the separate treatment of positively buoyant pieces, negatively buoyant microfibers, and negatively buoyant rigid particles of sufficiently big size, since these classes have very different dynamics and sources. In the following we concentrate on the properties, amount and dynamics of particles of the last class.

2.3 Considerations for modeling negatively buoyant rigid microplastics

2.3.1 Physical properties

From a meta-analysis of 39 previous studies, Erni-Cassola et al. (2019) established the proportion of the most abundant polymer types discharged into water bodies: PE (polyethylene, 23 %), PP (polypropylene, 13 %), PS (polystyrene, 4 %) and PP&A (group of polymer types formed by polyesters, PEST, polyamide, PA and acrylics, 13 %). Note that these proportions do not distinguish between different regions (e.g., coastal region or open water; even inland water bodies of urban environments are included in the analysis) and between the particle types (size range and shape) concerned in the different studies. We organize these polymer types according to their density (Chubarenko et al., 2016, Andrady, 2017, Erni-Cassola et al., 2019) in Fig. 2.1: PP between $850-920\ kg/m^3$, PE $890-980\ kg/m^3$, PS with $1040\ kg/m^3$ (excluding its foamed version), PEST in the range $1100-1400\ kg/m^3$, PA within $1120-1150\ kg/m^3$ and acrylic with $1180\ kg/m^3$. There is also some less abun-

dant plastic like polytetrafluoroethylene (PTFE) which has higher densities, in the range $2100 - 2300\ kg/m^3$.

Thus, the full range of microplastic particle densities in the ocean, denoted here as ρ_p, is $850 - 2300\ kg/m^3$, and most of them have densities within the interval $850 - 1400\ kg/m^3$. This has to be compared with the seawater density, which close to the surface has a conventional mean value of $\rho_f = 1025\ km/m^3$ (red line in Fig. 2.1) and changes around 1% from the surface to the sea bottom. Since we are interested in sinking material, and for the sake of maximal practicality, we restrict our study to microplastics of densities $1025\ kg/m^3 < \rho_f < 1400\ kg/m^3$.

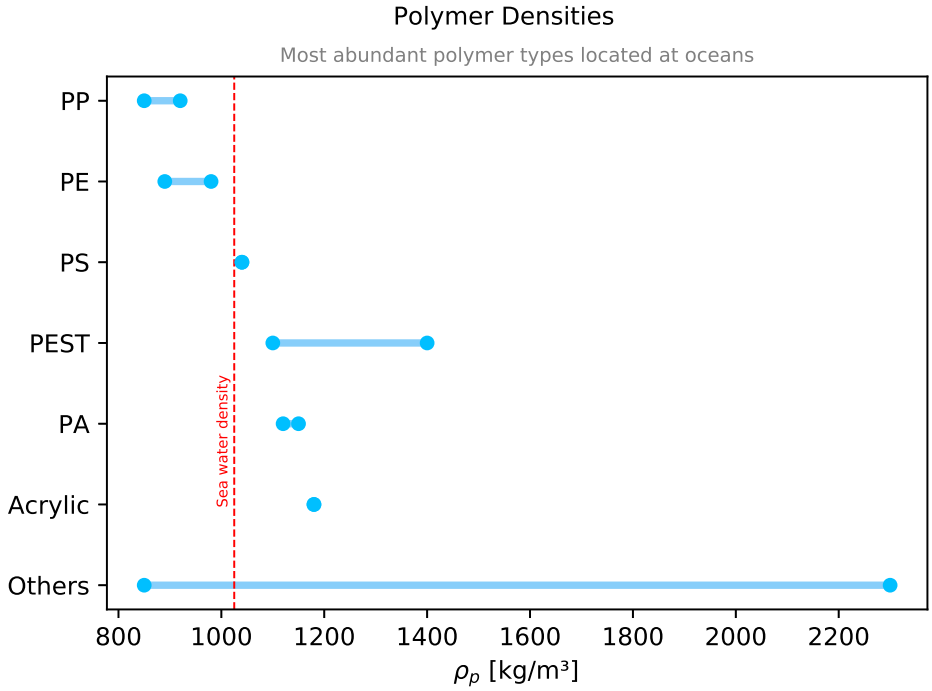

Fig. 2.1 Polymer densities for the most abundant microplastics identified in water bodies (Erni-Cassola et al., 2019).

Another relevant property of plastic particles is their size. By a widely accepted definition, microplastics are particles with a diameter less than 5 *mm* without any lower limit (Arthur et al., 2009). Some observations at the ocean surface show that the most common diameter is around 1 *mm* (Cózar et al., 2014, Cózar et al., 2015), with an exponential decay with increasing diameter up to 100 *mm*. However, the absence of this peak in other studies that show an increasing abundance with further decreasing size (Enders et al., 2015, Suaria et al., 2016, Erni-Cassola et al., 2017) suggests (Song et al., 2014, Andrady, 2015, Erni-Cassola et al., 2017, Bond et al., 2018, Lindeque et al., 2020) the need for new technologies in sampling methods (which usually use trawl nets with a mesh size around 0.3 *mm*) and

especially for the adaptation of careful and standardized analysis procedures to avoid artifacts (Filella, 2015).

Field data about distributions of size and quantifiers of shape for negatively buoyant rigid particles in the water column or deep-sea sediments are not available to date to the best of our knowledge, except in the Artic for Bergmann et al. (2017). However, their results may not apply to the majority of the oceans because of the very special dynamics provided by melting and freezing of sea ice (Bergmann et al., 2017). Data from Bergmann et al. (2017) and Song et al. (2014) about unspecified sedimented fragments and paint particles, respectively, exhibit an increasing abundance with decreasing size, most particles being smaller than 0.05 *mm*. Laboratory findings about surface degradation of individual particles also indicate such a tendency (Song et al., 2017). Thus, these findings seem to indicate the prominent presence of small pieces of plastic. Nevertheless the observations of Bagaev et al (2017), Kanhai et al. (2018) and Peng et al. (2018) do not indicate this abundance of small particles.

For these reasons, we will disregard particles of extremely small size. To keep our qualitative study sufficiently simple, we will consider all our modelled particles to have a radius $a = 0.05$ *mm* (a diameter of 0.1 *mm*). This is a rather small size, but still within the commonly measured ranges. As we will discuss in Section 2.4.1, this radius is well within the validity range of the MRG equation.

2.3.2 Source estimation

In this subsection we indicate the total amount of dense microplastics entering the water column in open waters of the Mediterranean. Despite the correlation of plastic source with coastal population density, the rapid fragmentation of small particles along the shoreline (Pedrotti et al., 2016) and the seasonal variability of spatial distribution of floating particles (Macias et al., 2019), we focus on local maritime activity and exclude direct release from surface accumulation areas or the coast, either from urban areas or from rivers. The estimations are based on the results of Kaandorp et al. (2020). They provide a total amount of yearly plastic release into the Mediterranean in the range $2200 - 4000$ tonnes, from which around 37% corresponds to negatively buoyant plastic, and 6% are due to maritime activity. This 37% agrees well with previous global estimations (Lebreton et al., 2018).

We will take these numbers, 4000 tonnes per year, 37% of sinking particles, and the proportion of direct release by maritime activity (6%) to obtain in Sect. 2.4.3 an estimate for the basin-wide yearly release of negatively buoyant sphere-like microplastics in the open Mediterranean. Note that we choose the upper bound, 4000 tonnes per year, in order to account for the considerable amount of unregistered particles.

2.3.3 Dynamics

A standard modeling approach (Siegel and Deuser, 1997, Monroy et al., 2017, Liu et al., 2018, Monroy et al., 2019) for the transport of noninteracting sinking particles is to consider the time-dependent particle velocity $\boldsymbol{v}$ as the combination of the ambient fluid flow $\boldsymbol{u}$ and a settling velocity $\boldsymbol{v}_s$ as:

$$\boldsymbol{v} = \boldsymbol{u} + \boldsymbol{v}_s \ , \tag{2.1}$$

with

$$\boldsymbol{v}_s = (1-\beta)\boldsymbol{g}\tau_p \ , \ \beta = \frac{3\rho_f}{2\rho_p + \rho_f} \ , \text{and } \tau_p = \frac{a^2}{3\beta\nu} \ . \tag{2.2}$$

$\boldsymbol{g}$ denotes the gravitational acceleration vector, pointing downwards; β is a parameter depending on the particle and the fluid densities, ρ_p and ρ_f, respectively. Particles heavier than water have $\beta < 1$, and $\beta = 1$ for neutrally buoyant particles. The expression given for β assumes spherical particles. τ_p is the Stokes time, i.e., the characteristic response time of the particle to changes in the flow, where a is the radius of the particle and ν the kinematic viscosity of the fluid. Although Eq. (2.1) is commonly used, we are not aware of a systematic justification of it in the microplastics context. This will be done in Section 2.4.1.

2.3.4 Numerical procedures

For the flow velocity $\boldsymbol{u}$ we use a 3D velocity field from NEMO (Nucleus for European Modelling of the Ocean), which implements a horizontal resolution of 1/12 degrees and 75 s-levels in the vertical with updates data every 5 days (Madec, 2008, Madec and Imbard, 1996). Salinity and temperature are also extracted from that model. The Parcels Lagrangian framework (Delandmeter and van Sebille, 2019) is used to integrate the particle trajectories from Eq. (2.1) or more complex ones to be considered in Sect. 2.4.1. Typical numerical experiments to obtain the results presented below consist of distributing a large number N of particles in a horizontal layer over the whole Mediterranean on the nodes of a sinusoidal-projection grid (Seong et al., 2002), so that their release is with uniform horizontal density. We locate this input source at 1 m depth to avoid surface boundary conditions. After particles are released at some initial date, in a so-called flash release, they evolve under equations of motion such as Eq. (2.1), and the statistics of the resulting particle cloud is analyzed.

2.4 Results

2.4.1 Dynamical equations of microplastics

We next show, closely following the treatment of Monroy et al. (2017) for biogenic particles, that possible inertial effects that would correct Eq. (2.1) are negligible for the sizes and densities of typical dense microplastics. To this end, similarly to many other studies (Michaelides, 2003, Balkovsky et al., 2001, Cartwright et al., 2010, Haller and Sapsis, 2008), we start by choosing the simplified standard form of the more fundamental Maxey–Riley–Gatignol (MRG) equation (Maxey and Riley, 1983), and analyze under which conditions it is valid for microplastic transport. After finding this simplified MRG equation to be valid for an important range of microplastic particles, we will explore its relationship with Eq. (2.1).

The simplified MRG equation gives the velocity $\boldsymbol{v}(t)$ of a very small spherical particle in the presence of an external flow $\boldsymbol{u}(\boldsymbol{r}(t),t)$ as

$$\frac{d\boldsymbol{v}}{dt} = \beta \frac{D\boldsymbol{u}}{Dt} + \frac{\boldsymbol{u} - \boldsymbol{v} + \boldsymbol{v}_s}{\tau_p}. \tag{2.3}$$

Beyond sphericity, two conditions are needed for the validity of Eq. (2.3) (Monroy et al., 2017, Maxey and Riley, 1983): a) the particle radius, a, has to be much smaller than the Kolmogorov length scale η of the flow, which has values in the range $0.3\ mm < \eta < 2\ mm$ for wind-driven turbulence in the upper ocean (Jiménez, 1997); b) the particle Reynolds number $Re_p = \frac{a|\boldsymbol{v}-\boldsymbol{u}|}{\nu} \approx \frac{av_s}{\nu}$ should satisfy $Re_p \ll 1$. Note that this last condition imposes restrictions on the values of the particles' density and size, partially via the settling velocity $v_s = |\boldsymbol{v}_s|$. For the most abundant sinking microplastics, i.e., with densities $\rho_p = 1025 - 1400\ kg/m^3$, we now determine the range of validity of Eq. (2.3) assuming $\nu = 1.15 \times 10^{-6}\ m^2/s$ and $\rho_f = 1025\ kg/m^3$ to be fixed. This gives β in the range $0.8 - 1$. The possibility of small changes in the seawater density as the particle sinks, which translates to variations in $\boldsymbol{v}_s$, will also be analyzed in Section 2.4.2.

In Fig. 2.2 we show a diagram with the settling velocities and particle sizes for which Eq. (2.3) is valid. We plot the minimal value of the Kolmogorov scale $\eta = 0.3\ mm$ with the red line (Jiménez, 1997), and $Re_p = 1$ with a black line, which bound the area of validity (shaded in the plot). We also indicate v_s as a function of a for $\beta = 0.8$ with the blue curve, corresponding to the upper bound to v_s for typical microplastic densities. In total, the zone with *soft* shading in Fig. 2.2 represents a parameter region where Eq. (2.3) applies for particles with $\beta < 0.8$ (i.e., particles falling faster than the typical ones), whereas the area of our interest, corresponding to $\beta \geq 0.8$, is represented by a *dark* shading, denoting the typical plastic sizes and corresponding settling velocities for which the equation is valid.

As a rule of thumb, in a typical situation, validity of Eq. (2.3) requires $v_s < 0.01\ m/s$ and $a < 0.3\ mm$. As discussed in Section 2.3.1, information about particles in the validity range is particularly sparse for surface waters because of the usual sampling techniques, but sediment data indicates the prevalence of sufficiently small particles. Furthermore, in sufficiently calm waters, the Kolmogorov scale is larger (of the order of millimeters, Jiménez (1997)), so that a can be increased to this size without compromising the equation validity. These estimates of the Kolmogorov scale anyway assume wind-driven turbulence and are thus restricted to the mixed layer (Jiménez, 1997), below which η is undoubtedly larger. Deviations from a spherical shape may lead to a more complicated motion than that described by the MRG equation, especially through particle rotation (Voth and Soldati, 2017). In App. A, we present quantitative arguments for the applicability of the MRG equation to rigid microplastic particles of common shapes in the parameter ranges of our interest.

The simplified MRG equation, Eq. (2.3) thus represents an appropriate basis for qualitative estimations of the transport properties of negatively buoyant rigid microplastics in the water column. Note that rigidity of the particles is an essential condition which is why the advection of microfibers is out of the scope of this research line.

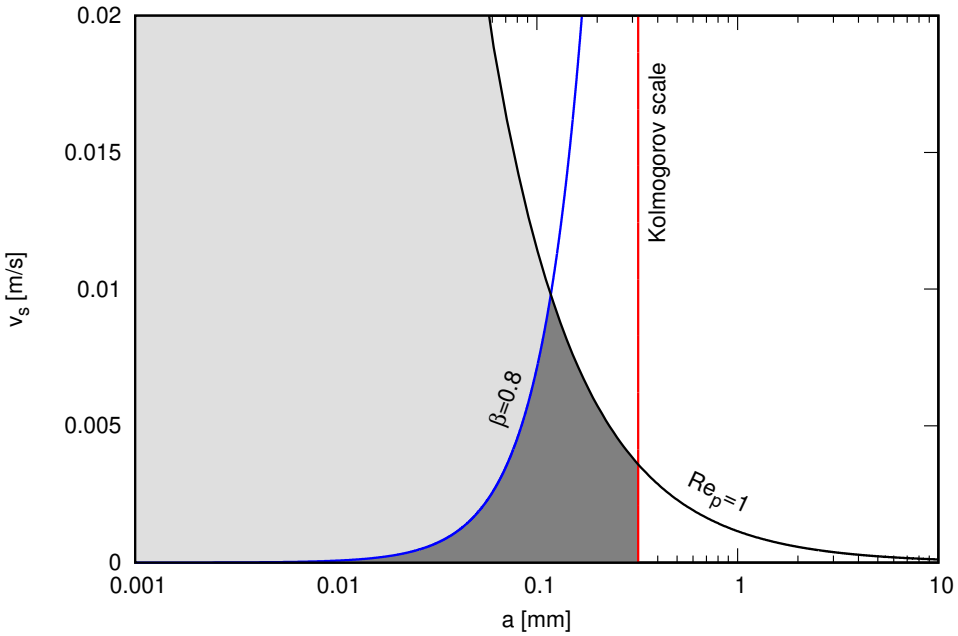

Fig. 2.2 Settling velocities and particle sizes for which Eq. (2.3) holds. Kolmogorov scale is represented by the red line and $Re_p = 1$ with a black line, which bound the area of validity. Blue curve corresponds to $v_s = v_s(\beta, a)$ for $\beta = 0.8$, the upper bound to v_s for typical microplastic densities. Dark shading denotes the plastic particle sizes and corresponding settling velocities for which application of Eq. (2.3) is valid.

The connection between Eq. (2.3) and its approximation Eq. (2.1) is made by noticing that $\tau_\eta \approx 1s$ in the ocean (Monroy et al., 2017, Jiménez, 1997), so that the Stokes number $St = \tau_p/\tau_\eta$, which measures the importance of particle inertia in a turbulent flow, is very small (of the order of $10^{-3} - 10^{-2}$). Thus an expansion of the MRG equation for small St (smallness of the Froude number, i.e. smallness of fluid accelerations with respect to gravity, is also required) can be performed. The expansion in its simplest form leads to (Balachandar and Eaton, 2010, Monroy et al., 2017, Drótos et al., 2019):

$$\boldsymbol{v} \approx \boldsymbol{u} + \boldsymbol{v}_s + \tau_p(\beta - 1)\frac{D\boldsymbol{u}}{Dt}. \tag{2.4}$$

We can now take the results of Monroy et al. (2017) for biogenic particles of sizes and densities similar to the microplastics considered here to show that the inertial corrections (the term proportional to τ_p) in Eq. (2.4) are negligible, so that the simpler Eq. (2.1) correctly describes sinking of microplastics in the considered parameter range. For completeness, we report in App. B the explicit numerical calculations showing this (in which the influence of the Coriolis force is also taken into account, since it is known to be of the same order or larger than the inertial term when a large-scale flow is used for $\boldsymbol{u}$). In particular we find from release experiments from 1 m below the surface of a large number of particles with β in the range $0.8 - 1$ in the whole Mediterranean that the difference between horizontal particle positions after 10 days of integration calculated from Eq. (2.4) and the simpler Eq. (2.1) is just a 0.26% of the horizontal displacements. For the vertical motions the difference is of about 0.05%. Thus, Eq. (2.1) provides a proper description of the dynamics.

Even if an equation of motion is accurate, the accuracy of its solution is limited by that of the input data. In particular, small-scale flow features are absent from oceanic velocity fields $\boldsymbol{u}$ simulated on large-scale domains, which is an important limitation of the respective solutions of Eq. (2.1). The NEMO velocity field of our choice is not an exception, but a rigorous evaluation of the corresponding errors of particle trajectories is not possible without knowing the actual small-scale flow. Nevertheless, one can roughly estimate the effect of these small scales by adding a stochastic term to Eq. (2.1) with statistical properties similar to the expected ones for a small-scale flow (Monroy et al., 2017, Kaandorp et al., 2020). Results similar to those by Monroy et al. (2017), summarized in App. B, indicate that after 10 days of integration the relative difference between particle positions given by Eq. (2.4) with and without this 'noise' term modeling small scales (using $\beta = 0.99$) is around 8% for the horizontal displacements and 5% for the vertical ones. The figures become 12% and 5%, respectively, when evolving the particles for 20 days. These errors are moderate, although they may be of importance under some circumstances (Nooteboom et al., 2020).

We consider these figures as a baseline to evaluate corrections to the simple Eq. (2.1): adding more complex particle-dynamics terms to it will not improve plastic-sedimentation modeling unless the effect of these corrections is significantly larger than the above estimations for the effect of the unknown small-scale flow. In the following we consider the simple Eq. (2.1), but we estimate the implications of assuming or not a constant value of the water density.

2.4.2 Effect of variable seawater density

In this section we analyze the role of a variable seawater density on the particle settling dynamics. Fluid density is calculated from the TEOS-10 equations, which is a thermodynamically consistent description of seawater properties derived from a Gibbs function, for which absolute salinity is used to describe salinity of seawater and conservative temperature replaces potential temperature (Pawlowicz, 2010). In the simulations described in this section, as particles move in the ocean they encounter different temperatures and salinities, as given by the NEMO model described in Sect. 2.3.4, and then they experience different values of the ambient-fluid density.

We consider particles of a fixed density $\rho_p = 1041.5\ kg/m^3$. This implies that for a nominal water density of $\rho_f = 1025\ kg/m^3$ the value of β would be $\beta = 0.99$, giving a sinking velocity $v_s = 6.2\ m/day$ for our particles of radius $a = 0.05\ mm$, but this sinking velocity will be increased or decreased in places where water density is lower or higher, respectively, so that we have a spatially- and temporally-dependent velocity in Eq. (2.1). The particle density and size have been chosen to be representative of the slowly-sinking microplastic particles, for which we expect the seawater density variations to have the largest impact. In this way we find some upper bound for the importance of variability in seawater density for particle trajectories.

We release $N = 78,803$ particles over the whole Mediterranean Sea, and monitor their trajectories under Eq. (2.1). The left panel of Fig. 2.3 shows the histogram of water densities encountered by the particles when the release is performed on July 8th 2000. On this summer date, the Mediterranean is well stratified, at least in its upper layers. Initially the particles are in surface waters with a range of salinities that average approximately to the nominal $\rho_f = 1025\ kg/m^3$. But as they sink in time they reach layers with higher densities (and more homogeneous across the Mediterranean). When the release is done in winter (right panel of Fig. 2.3) the water column is more mixed, so that the range of water densities experienced by the particles released at different points is always narrow. But the mean water density turns out to be always larger than the conventional surface density of $\rho_f = 1025\ kg/m^3$, so that a slightly slower sinking is expected to occur.

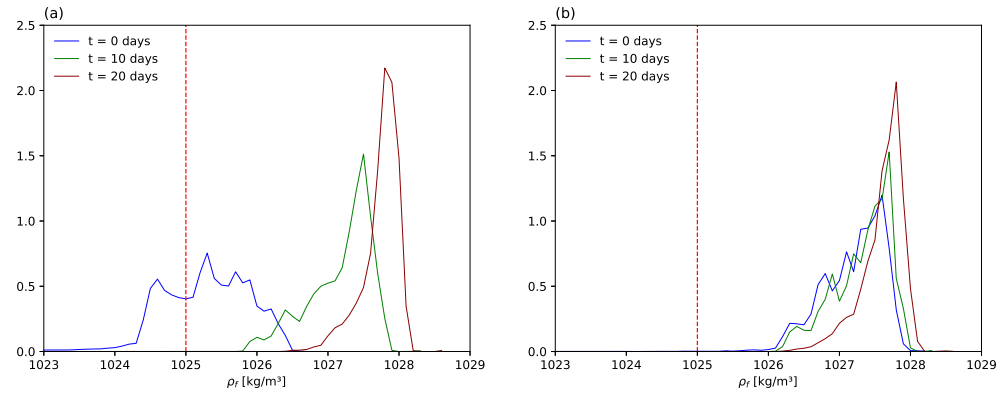

Fig. 2.3 Normalized histogram of the seawater density ρ_f at the positions of $N = 78803$ particles after $t = 0$, 10, and 20 days of being released over the whole Mediterranean. (a): summer release (release date 8 July 2000). (b): winter release (release date 8 January 2000). The particles' density is fixed at $\rho_p = 1041.5 kg/m^3$, and fluid density is obtained from the TEOS-10 equations. The vertical line indicates a conventional seawater density of $1025 kg/m^3$.

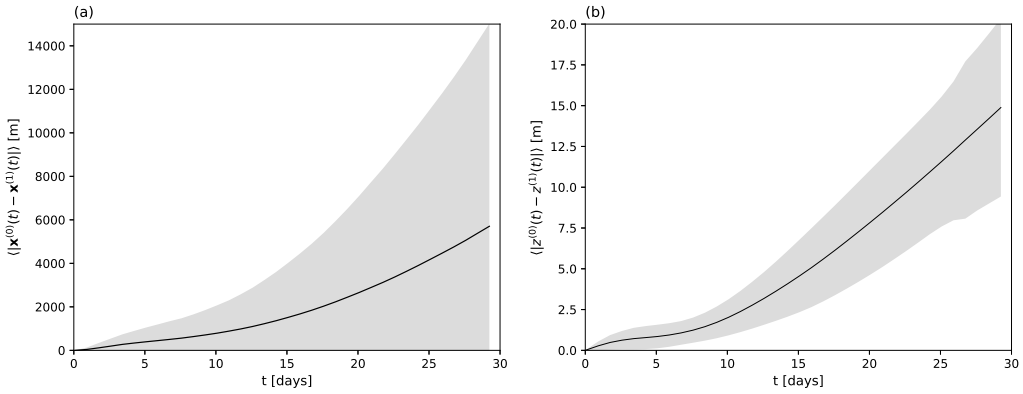

Fig. 2.4 The distance, as a function of time, between trajectories obtained with constant nominal fluid density of $\rho_f = 1025 kg/m^3$ and the actual variable fluid density, both starting at the same initial location. The range of the values among all particles released in different points of the Mediterranean is indicated by the shaded area, while the solid line indicates the average over the particles. Particles have $\rho_p = 1041.5 kg/m^3$, and all parameters are the same as for the summer release in Fig. 2.3.(a): horizontal distances; (b): vertical distances.

We illustrate the impact of this variable density on particle trajectories for the summer release in Fig 2.4. Here we compute, as a function of time, the range of horizontal $|\mathbf{x}^{(0)} - \mathbf{x}^{(1)}|$ and vertical $|z^{(0)} - z^{(1)}|$ distances and its average among particles. Trajectories $\mathbf{x}^{(0)}(t)$ and $\mathbf{x}^{(1)}(t)$ are obtained with constant nominal fluid density ($1025\ kg/m^3$) and position-dependent fluid density, respectively, using the same release location and date 8 July 2000 in both cases.

		10 days	20 days
Summer release	Horizontal:	1.12 %	2.75 %
	Vertical:	3.19 %	6.25 %
Winter release	Horizontal:	1.88 %	5.62 %
	Vertical:	8.14 %	9.32 %

Table 2.1 Relative effect on horizontal and vertical particle positions after 10 and 20 days of integration, averaged over 78803 particles released over the whole Mediterranean at 1 m depth, of replacing the actual seawater density by a nominal value $\rho_f = 1025\ kg/m^3$.

Particle density is fixed at $\rho_p = 1041.5\ kg/m^3$. The difference between the two calculations (and thus the error of considering that constant value for the density) should be compared to average horizontal and vertical displacements of 95 km and 124 m, respectively, at $t = 20$ days. At that time, we thus find that the influence of variable fluid density on the dynamics is about 3% for the horizontal movement and 6% for the vertical displacement on average.

A summary of the average relative differences on horizontal and vertical particle positions between using the location-dependent seawater density and a nominal constant value $\rho_f = 1025 kg/m^3$, both in winter and summer periods, is displayed in Table 2.1. The relative error produced by assuming a constant density is larger in the vertical direction. It is also larger for the release in winter, but this is a consequence of taking a value for the reference density that is not representative of winter waters but is strongly biased (see Fig. 2.3, right). If using a reference value more appropriate for winter waters (say $\rho_f \approx 1027\ kg/m^3$) the relative error remains quite small, due to the weaker stratification of the sea during this season. In fact, the reference value is also biased in the summer unless the investigation is restricted to the surface.

In brief, we see that the effect of location-dependent density may be a relevant effect to evaluate microplastic transport. At least, the traditional value of seawater density may be biased, which may be reflected in the particle trajectories. We recall, however, that we used parameters for the particle properties for which they are slowly falling. The impact of variable density on particles that sink faster will be smaller. Also, the effects reported in Table 2.1 remain of the order of the estimations of the effects of unresolved small scales of the flow (Sect. 2.4.1). As a consequence, in the following we will not consider variable seawater density, but restrict our modeling to Eq. (2.1) with a constant nominal value of the sinking velocity v_s.

2.4.3 Total mass and vertical distribution of microplastics

We will first estimate the total mass of negatively buoyant rigid microplastics in the water column of the open Mediterranean Sea by assuming a uniform vertical distribution, then we will justify this assumption by running numerical simulations according to the conclusion of Section 2.4.1 about the equation of motion.

For estimating the total mass, we take the quantities of Section 2.3.2 (4000 $tonnes/year$ of plastic release, with 37% being negatively buoyant of which 6% originates from maritime activities) to compute the rate r at which microplastic particles of our interest enter the water column in the open sea: $r = 4000\ tonnes/year \times 0.37 \times 0.06 = 88.8\ tonnes/year$, or $r = 0.24\ tonnes/day$.

The next step is to estimate the time during which these microplastic particles remain in the water column before reaching the sea bottom. We take the mean depth for the Mediterranean to be $h = 1480\ m$ (Eakins and Sharman, 2010, GEBCO Compilation Group, 2020) and estimate a residence time τ as the time of sinking to that mean depth. The residence time depends on the sinking velocity, $\tau = h/v_s$, and thus on the physical properties of the microplastic particles. Assuming a seawater density $\rho_f = 1025\ kg/m^3$, and the range of plastic densities and their proportions described in Sect. 2.3.1, we see from Eq. (2.2) that for microplastic particles of radius $a \approx 0.05\ mm$ the range of sinking velocities is $6.20 - 509.23\ m/day$, giving a residence time in the range $3.1 - 255\ days$. Averaging these times weighted by the proportion of each type of plastic we get $\overline{\tau} \approx 14\ days$. Combining the input rate r with this mean residence time we get an estimate for the total amount present in the water column at any given time as $Q = r\overline{\tau}$: the result is $Q \approx 3.36$ tonnes of dense rigid microplastics if all of them would be in the form of particles of size $a = 0.05\ mm$. This is below but close to 1% of the estimated upper bound of 470 tonnes of floating plastic in the Mediterranean (according to the corresponding estimation of Kaandorp et al. (2020)).

We emphasize the many uncertainties affecting this result (Sections 2.3.1 and 2.3.2), and we highlight the one related to particle size: because of the quadratic dependence of the sinking velocity on the particle radius a, Eq. (2.2), choosing the particle size to be half of the one used here will lead to a four times larger estimate for the mass if the same release rate is assumed. This enhanced retention of smaller particles in the water column may imply, depending on the actual size distribution, a dominance of very small particles on the plastic mass content of the water column. However, our estimates of plastic input into the ocean (we use mainly Kaandorp et al. (2020)) rely on observations that do not catch extremely small particles. These considerations further justify our choice of a radius $a = 0.05\ mm$, small but still easily detectable, as convenient to provide reasonable estimations of negatively buoyant rigid microplastic mass in the water column within commonly quoted size ranges.

We can not exclude larger plastic content at smaller sizes. Another source of bias may be not considering in this study the impact of small-scale turbulence and convective mixing events. While small-scale turbulence might cause an increase of lifetimes of particles in the water column, dense water formation and rapid convection, a process reported in areas such as the Gulf of Lions, might likely reduce particle retention time. These events take place in winter and were shown to transfer particles from the ocean surface to mid-waters (1000 meters) and deep ocean (>2000 meters) in a very short time (1-2 days) and lead to the formation of bottom nepheloid layers (de Madron et al., 1999, Vidal et al., 2009, Heussner et al., 2006, Stabholz et al., 2013).

The result for the total mass is independent of the horizontal distribution of particle release, which is quite inhomogeneous (Fig. 1 of Liubartseva et al., 2018). However, for a rough estimate of the density of these microplastics in the water column, we assume a uniform particle distribution over the whole Mediterranean both in horizontal and in vertical. Since the volume of the Mediterranean is about $4.39 \times 10^6\ km^3$ (Eakins and Sharman, 2010) the estimated density would be $\rho_V \approx 7.7 \times 10^{-11}\ kg/m^3$ (with the above-discussed scaling issues with a). We remind the reader that this is a value for the open sea, and our study does not address coastal areas, where the density would likely be higher.

The above estimates are rather rough as a result of the mentioned uncertainties. The assumption of a uniform distribution in the vertical direction has not yet been justified either, but we will show it to be appropriate by means of our simulations of particle release starting at 1 m depth over the whole Mediterranean. Instead of performing a continuous release of new particles at each time step, and computing statistics over this growing number of sinking particles, we approximate this by the statistics of all positions at all time steps of a set of particles deployed in a single release event. This assumes a time-independent fluid flow, but this approximation is appropriate, since the dispersion of an ensemble of particles released in a single event follows rather well-defined statistical laws, see Section 2.4.4, and is thus independent of the time-varying details of the flow. Particles are removed when touching the bottom. For our estimate, we use $\beta = 0.8$, i.e., assuming the fastest sinking velocity of typical plastic particles, for which particles reach vertical depths deeper if compared with the slower sinking velocities used in our study.

Figure 2.5 shows $\rho(z)$, the density of plastic particles per unit of depth z in the whole Mediterranean, and also $A(z)$, the amount of area that the Mediterranean has at each depth z. Both functions have been normalized such that the value of their integrals with respect to z is one; in this way the functions can be displayed in the same plot. We see that both curves are nearly identical (in fact, just proportional, because of the normalization), indicating that the variation of the number of particles with depth is essentially due to the decrease of sea area

with depth. A clearer way to see that is to plot $\rho(z)/A(z)$, which is proportional to the mean plastic concentration per unit volume at each depth z, $\rho_V(z)$. We see that this quantity is nearly constant, at least in the first 3000 m. At larger depths a weak increase seems to occur, but made unclear by the poor statistics arising from the small area and number of particles present at these depths. Thus, the hypothesis of a uniform distribution of plastic in the water column seems to be a reasonable description of the simulation of the fastest-sinking particles.

A uniform distribution of plastics in z is what is expected if the vertical velocity of the particles is exactly a constant (since each particle will spend exactly the same time at each depth interval). The equation of motion used, Eq. (2.1) corrects this constant sinking velocity $\boldsymbol{v_s}$ with a contribution $\boldsymbol{u}$ from the ambient flow. Thus, the close-to-constant character of the plastic concentration may imply that the flow correction $\boldsymbol{u}$ is negligible, at least when considering its effect over the whole Mediterranean. Another possibility is that the fluctuating flow component $\boldsymbol{u}$ in Eq. (2.1) results in a vertical dispersion compatible with a constant concentration. Although the former explanation predicts an alteration from a constant if the settling velocity is sufficiently small to allow $\boldsymbol{u}$ to induce a stronger vertical dispersion, we will see in the next section that a nearly constant concentration may be assumed for the majority of our parameter range.

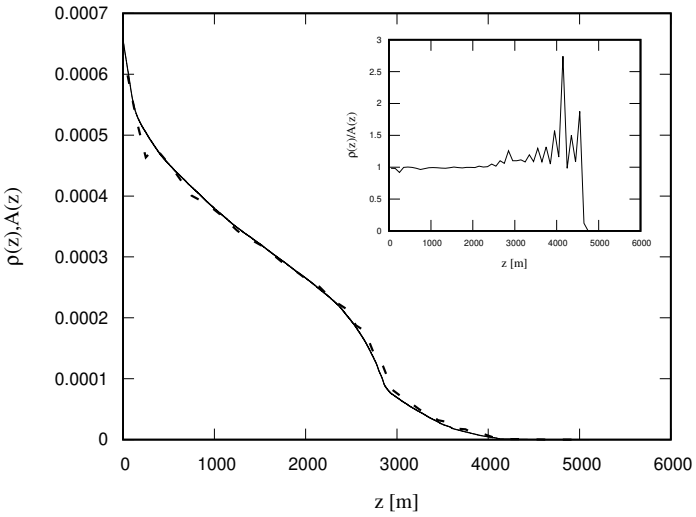

Fig. 2.5 The continuous line is the area that the Mediterranean has at each depth z. The dashed line is microplastic density per unit of depth $\rho(z)$ under continuous release of particles with $\beta = 0.8$ at 1 m depth. Both curves have been normalized to have unit area, so that they can be compared on the same scale. The binning size is 100 m. The inset shows the ratio $\rho(z)/A(z)$, proportional to the mass density of microplastic per unit of volume $\rho_V(z)$.

2.4.4 Transient evolution

We now analyze in detail the transient evolution of particle clouds initialized by flash releases at a fixed depth. Numerically we proceed by releasing $N = 78803$ particles uniformly distributed over the entire Mediterranean surface at 1 m depth in the winter season, as already described. They evolve according to Eq. (2.1) using a constant water density. We take three examples for the particle density, which correspond to $\beta = 0.8$, 0.9, 0.99, or $v_s = 153.48$, 68.21, 6.20 m/day for our particles of radius $a = 0.05$ mm, respectively; in what follows, these setups shall be denominated as v153, v68 and v6. The horizontal displacements during the particle sinking times are much larger (of the order of 60 km) than the sea depth, so that in fact the particles are sinking *sideways* (Siegel and Deuser, 1997). However, the horizontal displacements still remain very small compared to the basin size, and we concentrate on the vertical motion. Even though the vertical steady distribution has been found to be close to uniform in Section 2.4.3, the reason for this is not evident, and we will give support here for the pertinence of this finding to most of the relevant parameter range.

Figure 2.6 shows the vertical particle distribution at different times (upper plot is for v153, middle for v68 and bottom for v6). The plot is given in terms of a rescaled variable $\tilde{z} = \frac{z - t v_s}{\sigma_z}$ where $\sigma_z^2 \equiv \langle (z_i - \langle z_i \rangle)^2 \rangle$ is the variance of the particles' z coordinate. Here the subindex i refers to the particle and $\langle \ldots \rangle$ denotes averaging over different particles. Thus, we plot in the figure the rescaled distribution of the particles around the average depth of the particles at any given time. For comparison, the normal distribution is plotted with dashed lines. This figure shows deviations from Gaussianity for early times. The deviation from normal distribution decreases for later instants but remains considerable, especially for the tails, which may also be indicative of anomalous diffusive behavior. For reference, particles reach the mean Mediterranean depth, $h = 1480$ m at times $\tau = 9.64$, 21.8 and 246.7 days for v153, v68 and v6, respectively.

Since a non-Gaussian distribution is usually linked to anomalous dispersion (Neufeld and Hernández-García, 2009), we now analyze this aspect in detail by considering how the variance of the vertical particle distribution, $\sigma_z^2(t)$, evolves. Although there is a continual loss of particles because of reaching the seafloor with a varied topography, we illustrate in App. C that our conclusions are likely unaffected by this effect.

According to Fig. 2.7, dispersion appears to be governed by different laws in different regimes, which we shall distinguish by the approximate effective exponents ν, defined through approximate behaviors $\sigma_z^2 \sim t^\nu$ in different time intervals.

We start our analysis with the fastest-sinking particles (v153, Fig. 2.7a). At the very beginning, superdiffusion takes place with $\nu > 2$, which may be related to autocorrelation in the flow, but we will iterate on this question when comparing different settling velocities.

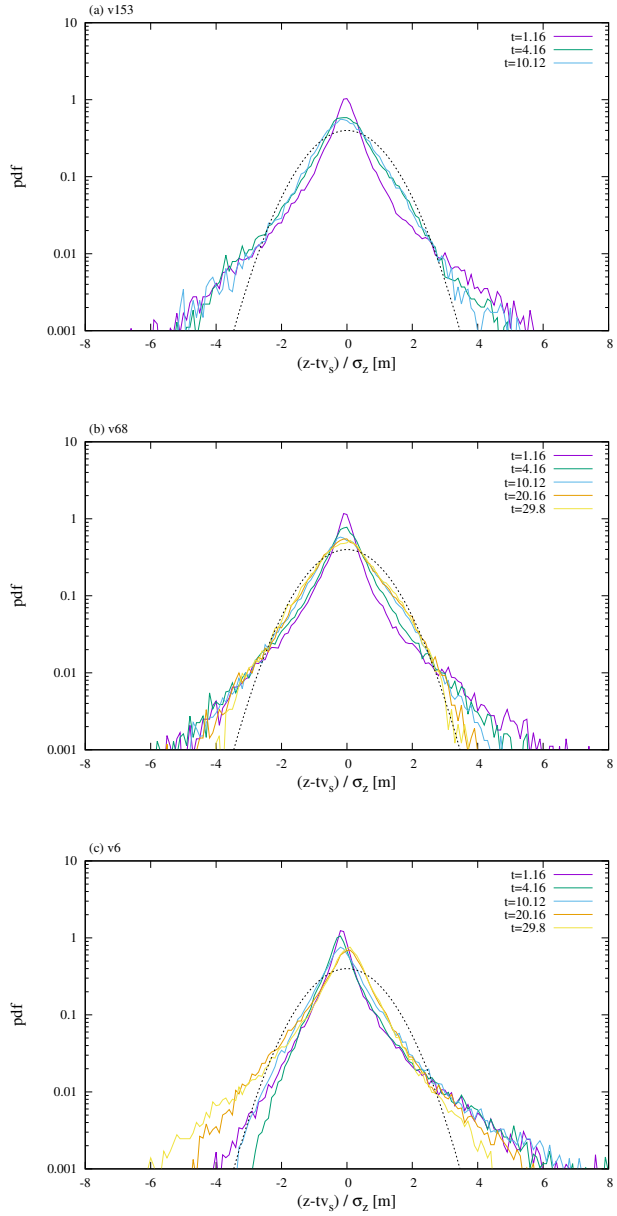

Fig. 2.6 The probability density function, estimated from a histogram of bin size 0.1, of all particles released in the Mediterranean in the rescaled variable $\tilde{z} = \frac{z - t v_s}{\sigma_z}$ for the different setups (v153, v68 and v6) and times (in days) as indicated. For comparison, normal distributions of zero mean and unit variance are shown with a dashed line.

Around $t = 1$ day, the evolution seems to become consistent with normal diffusion ($\nu = 1$), usual after initial transients in oceanic turbulence (Berloff and McWilliams, 2002, Reynolds, 2002). However, around $t = 4.5$ days, we can observe a crossover to ballistic dispersion ($\nu = 2$).

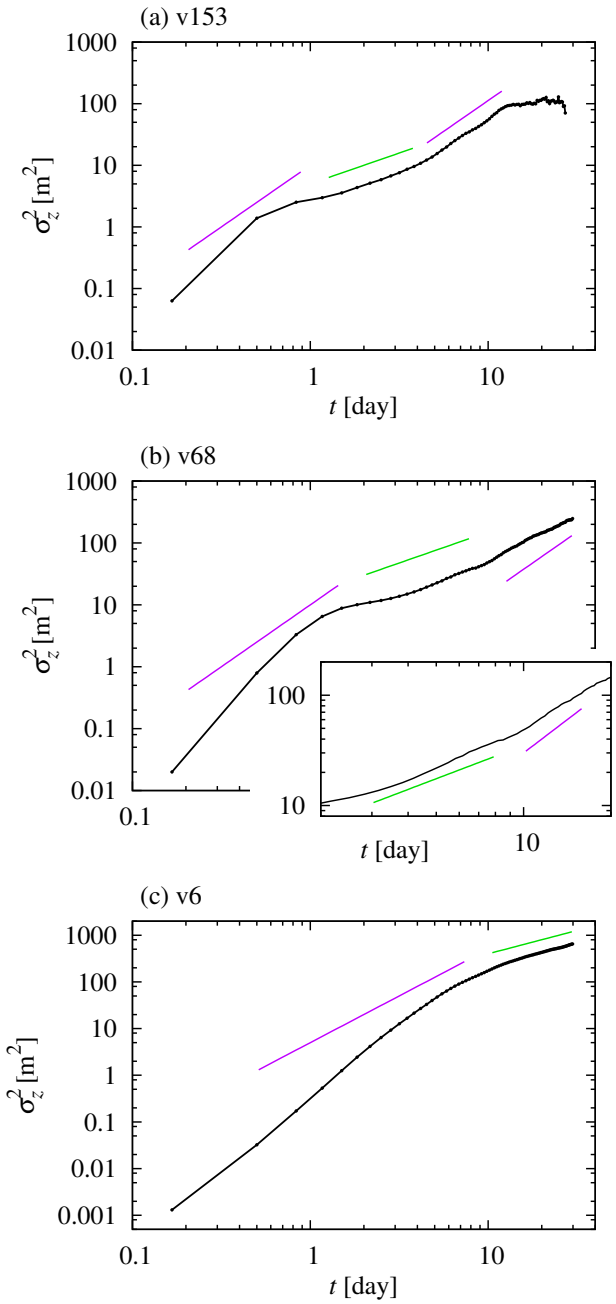

Fig. 2.7 Variance of depth reached by the particles as a function of time. Straight lines represent power laws for reference, with exponents 1 (in green, corresponding to standard diffusion) and 2 (in purple, corresponding to ballistic dispersion).

We explain this last crossover as resulting from a different mean sinking velocity in diverse regions of the Mediterranean, associated with up- and down-welling. This can be

modeled in an effective way by writing the vertical position of particle i as

$$z_i = \langle z_i \rangle + \bar{\omega}_i t + W_i, \tag{2.5}$$

where $\langle \ldots \rangle$ denotes, as before, an averaging over different particles. Here we are assuming that $z_i - \langle z_i \rangle$ evolves according to the sum of a constant average *velocity* contribution $\bar{\omega}_i$ for sufficiently long times (a characteristic of the flow region traversed by particle i), and of W_i, a Wiener process representing fluctuations with zero mean and defining a diffusion coefficient D_i for each trajectory by $\overline{W_i^2} = D_i t$. The overbar refers to temporal averaging for asymptotically long times along the trajectory of a given particle (but assuming that the particle remains in a region with a well-defined $\bar{\omega}_i \neq 0$), and D_i characterizes the strength of the fluctuations. Assuming $\langle \bar{\omega}_i W_i \rangle = 0$,

$$\sigma_z^2 \equiv \langle (z_i - \langle z_i \rangle)^2 \rangle = \langle \bar{\omega}_i^2 \rangle t^2 + \langle D_i \rangle t, \tag{2.6}$$

that is, the variance is a sum of a ballistic and a normal diffusive term, associated with regional differences in the mean velocity and with fluctuations, and dominating for long and short times, respectively. Writing $D = \langle D_i \rangle$, the crossover between the two regimes is obtained by equating the two terms as

$$t^* = \frac{D}{\langle \bar{\omega}_i^2 \rangle}. \tag{2.7}$$

To evaluate Eq. (2.7), we first estimate $\bar{\omega}_i$ for each particle from the "asymptotically" long time of $t = 10.83$ days, which is the latest time after the crossover still in the ballistic regime in Fig. 2.7a, when the contribution of fluctuations should already have become negligible. The horizontal pattern of the estimated $\bar{\omega}_i$ is presented in Fig. 2.8, which confirms its patchiness throughout the Mediterranean, associated with mesoscale features. Computing $\langle \bar{\omega}_i^2 \rangle$ and fitting a line to $\sigma_z^2(t)$ between $t = 1.4$ and 4 days to estimate D, we obtain $t^* \approx 4.5$ days from Eq. (2.7), which remarkably agrees with Fig. 2.7a. After approximately $t = 12$ days there is hardly any dispersion, since most of the particles are close to the sea bottom (cf. Fig. 2.9) where the vertical fluid velocity is nearly zero. Note also a small drop in $\sigma_z^2($ at the very end of the time series, where the results may actually be subject to artifacts, see App. C. However, this is of minor importance, since the distribution of particles so close to the bottom should anyway be strongly influenced by resuspension and remixing by bottom currents (Kane et al., 2020).

The different regimes are not as clear in the v68 case as for v153, see Fig. 2.7b. One evident novel feature is a subdiffusive regime during the transient from the initial superdif-

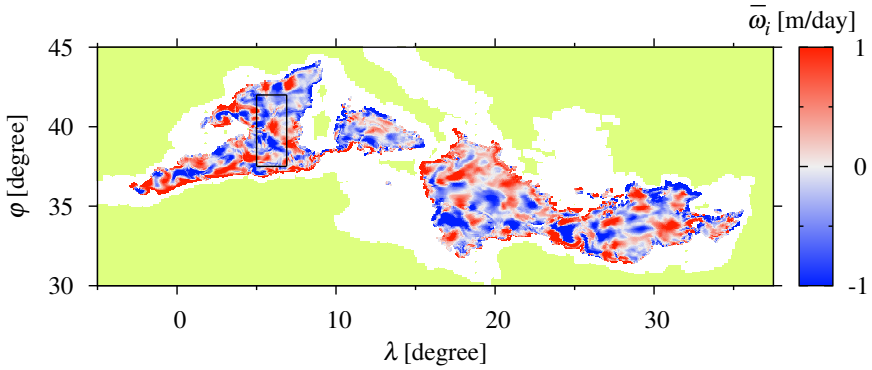

Fig. 2.8 $\bar{\omega}_i$ as estimated from $t = 10.83$ days plotted at the initial position of each particle i in the v153 simulation. The black rectangle in the Western Mediterranean is the area of large depth considered in App. C.

fusion (as in the case of horizontal tracer dispersion in the ocean studied by Berloff and McWilliams (2002), Reynolds (2002)). Approximate normal diffusion is then observed until $t = 10$ days, when a crossover to a faster dispersion does seem to take place, see the inset. A fit of normal diffusion from $t = 4$ to 8 days and the velocity variance at $t = 12.5$ days give an estimate $t^* \approx 11.7$. However, the long-time ballistic regime is not clear. In fact, a long-term return from such a ballistic regime to normal diffusion is expected as a result of increasing horizontal mixing, which renders $\bar{\omega}_i$ time dependent and makes it approach zero. According to a careful visual inspection of the inset in Fig. 2.7b, this may take place already around $t = 14$ days.

For v6 (Fig. 2.7c), the transition from the initial superdiffusive regime to that of normal diffusion appears to not involve subdiffusion. This is already informative: the fluid velocity field is the same for the three simulations with different settling velocity, so the differences must originate from the different rate of sampling of the different fluid layers by particles while they sink. In particular, the decay of autocorrelation is obviously faster for faster-sinking particles, since it is determined by the spatial structure of the velocity field.

While this is one possible explanation for the earlier timing of the initial transition from anomalous to normal diffusion for higher settling velocity, one cannot exclude that a depth-dependent organization of the flow is more in play; note that $\nu > 2$ at the beginning, which might not be explained by simple autocorrelation but might be characteristic of properties of the velocity field at those depths. The governing role of the spatial structure is supported by Fig. 2.9: the transition in question takes place at the same depth ($\approx$ 100m) in the different simulations, which seems to point to mixed-layer processes. Depth-dependence might also govern the suppression of ballistic dispersion for long times, but it is very unclear.

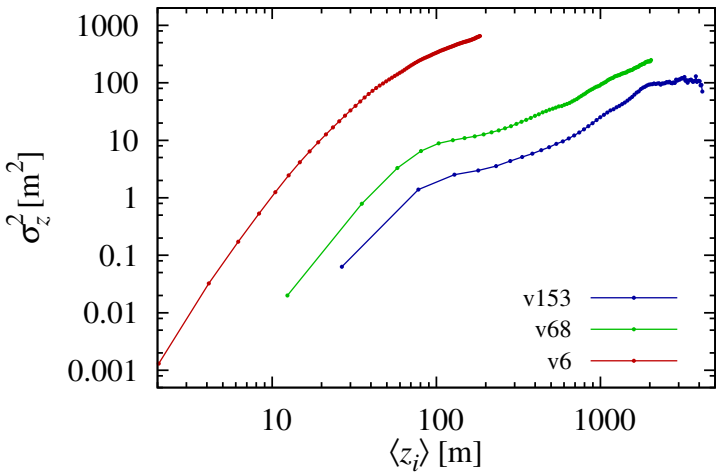

Fig. 2.9 Variance of depth reached by the particles as a function of their mean depth.

Note in Fig. 2.9 that the vertical variance is not expected to grow much larger for v68 than for v153 even if the simulation were longer. Therefore, even if the constancy of the steady vertical distribution relies on the weak vertical dispersion for v153 (see Section 2.4.3), constancy is expected to hold in most of our parameter range. A considerably stronger dispersion and a possible corresponding deviation from constancy may arise only for extremely low settling velocities, like for v6 in Fig. 2.9.

2.5 Conclusions

We have discussed the different types of plastics occurring in the water column, pointing out gaps in our knowledge about the sources, transport pathways and properties of such particles. It would be highly beneficial to have distributions of size, polymer type and quantifiers of shape recorded separately for the dynamically different classes of microplastics.

We have focused our attention on rigid microplastic particles with negative buoyancy. We have argued that the simplified MRG equation approximates the dynamics of such particles sufficiently well for qualitative estimations.

We have then analyzed the importance of different effects in this equation, and concluded that the Coriolis and the inertial terms are negligible. When a velocity field of large-scale nature is input to the equation (such that small-scale turbulence is not resolved), or when the variability in seawater density is neglected, moderate but possibly non-negligible errors emerge (Nooteboom et al., 2020). However, our conclusions about the vertical distribution and dispersion of microplastics rely on robust features of the large-scale flow and must

remain unaffected by moderate errors. We also note that the traditional value of seawater density, $\rho_f = 1025\ kg/m^3$, is representative only for near-surface layers in the summer, and correcting for the bias could reduce the error of simulations with a constant seawater density. A suitable equation of motion for the particles considered is constructed by adding to the the external velocity field a constant settling term, as also found by Monroy et al. (2017) for marine biogenic particles.

When the velocity field of the Mediterranean sea is approximated by realistic simulation, this equation of motion results in a nearly uniform steady distribution along the water column, perhaps except at extremely low settling velocities. The corresponding total amount of plastic present in the water column is relatively small, close to 1% of the floating plastic mass, but it may be an important contribution to the microplastic pollution in deep layers of the ocean, and is subject to several uncertainties.

Note that only those microplastic particles are considered here that have not yet sedimented on the bottom, and the plastic amount sedimented on the seafloor is large (Fischer et al., 2015, Liubartseva et al., 2018, Peng et al., 2018, Mountford and Morales Maqueda, 2019, Soto-Navarro et al., 2020). The suitability of our equation of motion to describe the sinking of a class of microplastic particles implies that advection by the flow may contribute to large-scale horizontal inhomogeneity of deep-sea plastic sediments by means of recently described noninertial mechanisms (Drótos et al., 2019, Monroy et al., 2019, Sozza et al., 2020). This may especially be so in regions where redistribution by bottom flows is restricted to small distances, like abyssal plains (Kane and Clare, 2019). Resuspension and redistribution may be dominant in forming sedimented patterns (Kane et al., 2020), and a future investigation should take all processes into account to identify zones of high plastic concentration on the sea bottom.

As for the vertical distribution profile, its approximate uniformity may be linked to the weak vertical dispersion of particles that is found in our simulations started with a flash release over the whole surface of the Mediterranean sea. The shape of the emerging transient vertical distribution exhibits deviations from a Gaussian, which are related to anomalous diffusive laws that dominate the vertical dispersion process in some phases.

The different diffusive laws are related to the properties of the decay in the Lagrangian velocity autocorrelation defined along the trajectories of the sinking particles. An important example is the transition from initial superdiffusion to a longer phase of normal diffusion, occurring around 100 m depth, which indicates that the particles enter into a different flow regime. Another characteristic of the velocity field is a horizontal patchiness, which results in a long-term ballistic dispersion as long as the particles' horizontal displacements remain small. The vertical diffusion returns to the normal type when horizontal mixing becomes

more developed. These results suggest regional differences in the sinking process, so that regional modeling might be more appropriate than a whole-basin approach. Future studies will include different areas of the oceans, and analyze the role of Lagrangian coherent structures on the different vertical dispersion regimes.

Chapter 3

Network and geometric characterization of three-dimensional fluid transport between two layers

3.1 Introduction

The study of transport phenomena is at the core of fluid mechanics. The Lagrangian approach to fluid transport has received powerful insights from its relationship to chaos and dynamical systems (Ottino and Ottino, 1989, Wiggins, 2005, Shadden et al., 2005), and more recently from set-oriented methodologies than can be recast into the language of graph or network theory (Bollt and Santitissadeekorn, 2013, Ser-Giacomi et al., 2015a, Froyland et al., 2014, 2007).

In most of the previous applications of these developments to geophysical contexts, consideration has been restricted to horizontal transport, as this is the dominant mode of motion at large scales in oceans and in the atmosphere. Some works, however, have addressed the full three-dimensional dynamics (Froyland et al., 2015, Bettencourt et al., 2015, 2017). Less attention has been given to the application or adaptation of the approaches mentioned above to the peculiarities of transport in the vertical direction, which is singled out by the gravitational force.

As the main motivation for the present work, many relevant biogeochemical phenomena involve the vertical transport of particles in the ocean. Two paradigmatic examples are the sinking of biogenic particles (Siegel and Deuser, 1997, Monroy et al., 2017), like

The contents of this Chapter are based on de la Fuente et al. (2021a).

phytoplankton cells and marine snow, which play a fundamental role in the biological carbon pump (Sabine et al., 2004, De La Rocha and Passow, 2007), and the sedimentation dynamics of microplastics, which are becoming a key environmental problem (Choy et al., 2019, Kaandorp et al., 2020, de la Fuente et al., 2021b). Despite the numerous studies with different experimental and theoretical methodologies many questions remain open, in particular those concerning the final fate of the particles from a known release surface area (i.e. the connection paths between surface and deep ocean), the amount and time they are suspended in the water column, and the spatial distribution both over the water column and the seafloor. Beyond the ocean context, vertical transport is also relevant in many other situations such as engineering processes (Michaelides, 2003) or rain precipitation (Falkovich et al., 2002). The objective of this chapter is to extend and adapt the powerful previously commented Lagrangian methodologies to situations in which there is a strong anisotropy in the flow leading to a clear transport direction, as is the case when considering sinking particles in fluid flows. We will concentrate on characterizing transport between two layers: in the case of particles sedimenting under gravity, particles released from an upper layer are driven by the flow and reach and accumulate in a lower layer. We expect our formalism would be useful also under transport anisotropies produced by forces other than gravity. The main object we will define is a two-layer map that connects the initial conditions of particles released from one of the layers to their final positions in the other one, after being transported by the flow. We extract information from this map with the two complementary approaches mentioned above: on the one hand we use dynamical systems tools to describe the geometry of the evolution of sheets of particles released from the initial layer. In this way we formalize previous results obtained in this context (Monroy et al., 2019, Drótos et al., 2019, Sozza et al., 2020) and extend them by the introduction of a new quantifier related to Lyapunov exponents: the Finite Depth Lyapunov Exponent. On the other hand, connectivity properties between the layers are studied with network theory or probabilistic techniques. Relationships between both approaches are obtained, and the whole formalism is illustrated with a model flow: a modification of the ABC flow which is frequently used as a simple example of three-dimensional chaotic advection, to which we add an additional velocity, modeling sinking, in the vertical direction.

The outline of the chapter is as follows. In Section 3.2 we introduce the basic Lagrangian description for transport of particles between two layers. In 3.3 we study the geometry and dynamics of a falling layer of particles, introducing the new type of Lyapunov exponent. In Section 3.4 we introduce the network methods to characterize connectivity, and in Section 3.5 we show the connection between the previous two descriptions. In Section 3.7 we present

the numerical results obtained for the modified ABC flow model. Section 3.8 presents our conclusions. Appendix D contains additional technical details.

3.2 Characterization of transport between two layers

Given a fluid flow characterized by a velocity field $\boldsymbol{u}(\mathbf{r},t)$, the Lagrangian description of transport considers the equations of motion for the position of fluid elements, which evolve according to

$$\frac{\mathrm{d}\mathbf{r}(t)}{\mathrm{d}t} = \boldsymbol{u}(\mathbf{r}(t),t)\ . \tag{3.1}$$

This equation defines the flow map $\phi_{t_0}^{\tau}(\mathbf{r}_0)$, such that integrating Eq. (3.1) for a given initial condition $\mathbf{r}_0$ at t_0 gives the final position of the fluid particle at time $t_0+\tau$:

$$\phi_{t_0}^{\tau}(\mathbf{r}_0) = \mathbf{r}(t_0+\tau). \tag{3.2}$$

In this thesis we will restrict to the situation in which $\boldsymbol{u}(\mathbf{r}(t),t)$ is a three-dimensional velocity field, and trajectories $\mathbf{r}(t)$ move in regions of $\mathbb{R}^3$.

Description (3.1) is not only pertinent for the motion of fluid elements. Particles of other substances immersed in a fluid also satisfy a first-order equation like (3.1), provided they are sufficiently small for their inertia to be neglected. For example, in a variety of realistic situations in the ocean, the equation of motion for the position of many types of particles of biological origin or of microplastics is ruled by Eq. (3.1), in which the velocity field to be used is the velocity of the fluid flow with the addition of a constant vertical component related to the sinking of the particle under gravity because of its weight (Siegel and Deuser, 1997, Monroy et al., 2017, de la Fuente et al., 2021b). In this chapter we will talk about the motion of 'particles' without specifying if they are particles of fluid or particles submerged in a fluid, provided an equation of the type (3.1), and thus (3.2), applies.

An object that plays an important role in the analysis of the map in (3.2) is its Jacobian matrix (a 3×3 matrix), defined by

$$\boldsymbol{J} = \nabla\phi_{t_0}^{\tau}(\mathbf{r}_0). \tag{3.3}$$

Given an infinitesimal separation between two initial conditions $\mathrm{d}\mathbf{r}_0$, $\boldsymbol{J}$ gives the evolution in time of this separation: $\mathrm{d}\mathbf{r}(t_0+\tau) = \boldsymbol{J}\cdot\mathrm{d}\mathbf{r}_0$. The singular values $\{S_\alpha\}_{\alpha=1,2,3}$ of $\boldsymbol{J}$ (i.e. the square roots of the eigenvalues of the Cauchy-Green tensor $C = \boldsymbol{J}^T\boldsymbol{J}$) give the stretching factors experienced by infinitesimal material line elements oriented along the eigendirections and started around $\mathbf{r}_0$ while integrated from t_0 to $t_0+\tau$. The standard finite-time Lyapunov

exponents (FTLE, $\{\lambda_\alpha\}_{\alpha=1,2,3}$) are obtained from these singular values as $\lambda_\alpha = |\tau|^{-1} \ln S_\alpha$ (Shadden et al., 2005).

In this chapter we are interested in anisotropic situations in which a direction of flow is distinguished from the others. Specifically, instead of the fully three-dimensional motion described by $\phi_{t_0}^{\tau}$, we are interested in the dynamics of fluid particles traveling between a pair of two-dimensional layers. The main example is the case of particles released from an upper horizontal layer, falling by gravity across a moving flow, and being collected on a second lower horizontal layer. Other sources of anisotropy can play the role of gravity, but in this chapter we use the terminology appropriate to the sedimentation by gravity example, so that both layers will be considered to be horizontal, and the first one will be called the *upper* or *release* layer, whereas the second one will be called the *lower* or the *collecting* layer. We distinguish the *vertical* coordinate z from the *horizontal* ones that form the horizontal vector $\mathbf{x}$, so that $\mathbf{r} = (x, y, x) \equiv (\mathbf{x}, z)$. Particles are initially released (at t_0) from the horizontal layer $\mathscr{M}$ characterized by 'height' z_0: $\mathscr{M} \equiv \{\mathbf{r} = (\mathbf{x}_0, z_0), z_0 \text{ fixed}\}$, and we want to track the horizontal position $\mathbf{x}$ at which the particle started at $\mathbf{r}_0$ first reaches the second horizontal layer characterized by 'depth' z. As we stop the dynamics after this first arrival, we can say that particles 'accumulate' at the second layer. This procedure defines a new flow map which we call the *two-layer map*: $\mathbf{x} = \phi_{z_0}^{z}(\mathbf{x}_0)$. We do not explicitly specify the initial time t_0 but for time-dependent velocity fields there will be a dependence on it.

Given a region $D \in \mathscr{M}$ of the upper layer, we call its image $\phi_{z_0}^{z}(D)$ onto the lower one its *footprint*. It is the region of the collecting layer where particles from D will become accumulated.

Particles released at the same time do not necessarily arrive at the same time at the final layer. Let $\omega(\mathbf{x}_0)$ be the time that a particle started at t_0 from $(\mathbf{x}_0, z_0)$ takes to reach the second layer at z for the first time. Thus the time of arrival is $t_z = t_0 + \omega$. Although not explicitly written, ω and t_z depend on t_0, z_0 and z, in addition to $\mathbf{x}_0$. In terms of ω, the relationship between the coordinates of the two flow maps introduced so far is:

$$\begin{aligned} \phi_{z_0}^{z}(\mathbf{x}_0) = \mathbf{x}(t_0 + \omega(\mathbf{x}_0)) &= \phi_{t_0}^{\omega(\mathbf{x}_0)}(\mathbf{r} = (\mathbf{x}_0, z_0))\,|_{\mathrm{h}}\,, \\ z &= \phi_{t_0}^{\omega(\mathbf{x}_0)}(\mathbf{r} = (\mathbf{x}_0, z_0))\,|_{z}\,, \end{aligned} \tag{3.4}$$

where the subindices h and z indicate that the horizontal and vertical coordinates of $\phi_{t_0}^{\omega}$, respectively, should be taken.

In general $\phi_{z_0}^{z}$ can always be computed by solving Eq. (3.1) from initial conditions on $\mathscr{M}$, and checking when the trajectory crosses the second layer at z, as Eq. (3.4) indicates. In the following we will use this last method.

The Jacobian associated with the two-layer map is

$$\bar{\boldsymbol{J}}_{\mathscr{M}} = \nabla \phi^z_{z_0}(\mathbf{x}_0) \, . \tag{3.5}$$

Note that the gradient acts on the two-dimensional initial position $\mathbf{x}_0$, so that $\bar{\boldsymbol{J}}_{\mathscr{M}}$ is a 2×2 matrix. The subindex $\mathscr{M}$ is a reminder of the fact that $\bar{\boldsymbol{J}}_{\mathscr{M}}$ is defined on each point $\mathbf{x}_0$ of the upper layer $\mathscr{M}$.

The singular values of this new Jacobian matrix are the square roots of the eigenvalues of the associated 2×2 Cauchy-Green tensor:

$$\bar{C}_{\mathscr{M}} = (\nabla \phi^z_{z_0}(\mathbf{x}_0))^T \cdot \nabla \phi^z_{z_0}(\mathbf{x}_0), \tag{3.6}$$

which will be used later on.

We next develop the two complementary approaches we propose to study transport between two layers: the geometric and the network approaches.

3.3 Geometric characterization of a falling layer

First we introduce a geometric characterization of the deformation of the falling layer of released particles with tools from dynamical systems. This approach can be called both *geometric* or *dynamical*.

In the same way that the three-dimensional Jacobian matrix $\boldsymbol{J}$ maps infinitesimal vector particle separations from time t_0 to time t ($\mathrm{d}\mathbf{r}(t) = \boldsymbol{J} \cdot \mathrm{d}\mathbf{r}_0$), $\bar{\boldsymbol{J}}_{\mathscr{M}}$ takes initial infinitesimal separations $\mathrm{d}\mathbf{x}_0$ on the horizontal release layer and gives its footprint $\mathrm{d}\mathbf{x}_z$ on the collecting layer: $\mathrm{d}\mathbf{x}_z = \bar{\boldsymbol{J}}_{\mathscr{M}} \cdot \mathrm{d}\mathbf{x}_0$. The singular values $\bar{\Lambda}_1$ and $\bar{\Lambda}_2$ of $\bar{\boldsymbol{J}}_{\mathscr{M}}$ give the stretching factors experienced by the footprint of line elements initially oriented along the eigendirections of $\bar{C}_{\mathscr{M}}$. In analogy with the definition of FTLEs, we can define *Finite-Depth Lyapunov Exponents* (FDLEs, $\bar{\lambda}_\alpha(\mathbf{x}_0)$) as the logarithmic rate of stretching along the eigendirections:

$$\bar{\lambda}_\alpha(\mathbf{x}_0) = \frac{1}{|z - z_0|} \log \bar{\Lambda}_\alpha \, , \alpha = 1, 2. \tag{3.7}$$

$\bar{\lambda}_\alpha$ is naturally expressed as a function of $\mathbf{x}_0$. But in fact it is a property of the trajectory joining $\mathbf{x}_0$ and $\mathbf{x} = \phi^z_{z_0}(\mathbf{x}_0)$, so that it (and also $\bar{\Lambda}_\alpha$) can be thought and displayed as a function of the coordinates on the collecting layer, $\mathbf{x}$. Although not explicitly indicated, $\bar{\lambda}_\alpha$ (and $\bar{\Lambda}_\alpha$) is a function of t_0, z_0 and z. Values $\bar{\lambda}_\alpha > 0$ ($\bar{\Lambda}_\alpha > 1$) indicate that lengths grow when initially in the corresponding eigendirection, whereas $\bar{\lambda}_\alpha < 0$ ($\bar{\Lambda}_\alpha < 1$) indicate length contraction. If $\bar{\lambda}_1 > \bar{\lambda}_2$, for sufficiently large differences of depth $|z - z_0|$ we would have

$|\mathrm{d}\mathbf{x}_z| \approx e^{|z-z_0|\bar{\lambda}_1}|\mathrm{d}\mathbf{x}_0^{(1)}|$, where $\mathrm{d}\mathbf{x}_0^{(1)}$ is the projection of the initial particle separation $\mathrm{d}\mathbf{x}_0$ onto the singular vector of singular value $\bar{\Lambda}_1$.

At difference with the FTLE, the FDLE has dimensions of inverse of length, not of time. But this is not the most important difference between the two quantities (in fact an alternative definition could be to replace $|z-z_0|$ by ω in (3.7)). The main difference is that the FTLE quantifies the stretching of initial vectors as they are transported by the flow in three-dimensional space, whereas the FDLE also includes the projection effect experienced by these vectors when arriving at the collecting layer: the footprint of such a vector is the projection onto the horizontal layer of that vector arriving there, taken along its direction of motion. Further details of this projection process are given in App. D, and are also illustrated in Fig. 3.1. Note also that the FDLE is not a form of a finite-size Lyapunov exponent (Aurell et al., 1997, Bettencourt et al., 2013, Cencini and Vulpiani, 2013), since for this last quantity initial separations are integrated until reaching a specified separation value, whereas in the FDLE integration proceeds until reaching a particular depth level z.

Next, we consider the effect of the flow on surface elements initially in the release layer. This was already considered in (Monroy et al., 2017, 2019, Drótos et al., 2019, Sozza et al., 2020) in the context of sedimenting particles in fluid flows.

Let us consider an infinitesimal material surface of area $\mathrm{d}A_0$ started at the release layer at z_0, which at any time is transformed into a surface of area $\mathrm{d}A_t$, and which finally reaches the collecting layer at z leaving a footprint area $\mathrm{d}A_{\mathrm{acc}}$ (see Fig. 3.1). If we take the initial surface element to be a rectangle of sides given by the vectors $\hat{\boldsymbol{x}}\mathrm{d}x_0$ and $\hat{\boldsymbol{y}}\mathrm{d}y_0$ ($\hat{\mathbf{x}}$ and $\hat{\boldsymbol{y}}$ are unit vectors in the x and y directions; the area of the rectangle is $\mathrm{d}A_0 = \mathrm{d}x_0\mathrm{d}y_0$), and noting that the cross product of vectors gives the area of the parallelogram subtended by them, we obtain

$$\mathrm{d}A_{\mathrm{acc}} = |\bar{\boldsymbol{\tau}}_{\boldsymbol{x}} \times \bar{\boldsymbol{\tau}}_{\boldsymbol{y}}|\mathrm{d}A_0, \tag{3.8}$$

where $\bar{\boldsymbol{\tau}}_{\boldsymbol{x}} = \frac{\partial \phi^z_{z_0}(\mathbf{x}_0)}{\partial x_0}$ and $\bar{\boldsymbol{\tau}}_{\boldsymbol{y}} = \frac{\partial \phi^z_{z_0}(\mathbf{x}_0)}{\partial y_0}$ are two-dimensional vectors on the final layer such that $\bar{\boldsymbol{\tau}}_{\boldsymbol{x}}\mathrm{d}x_0$ and $\bar{\boldsymbol{\tau}}_{\boldsymbol{y}}\mathrm{d}y_0$ give the footprint of the initial vectors $\hat{\mathbf{x}}\mathrm{d}x_0$ and $\hat{\boldsymbol{y}}\mathrm{d}y_0$.

Simple algebra relates the cross product in (3.8) to the matrix $\bar{C}_{\mathscr{M}}$ and the singular values $\bar{\Lambda}_\alpha$:

$$|\bar{\boldsymbol{\tau}}_x \times \bar{\boldsymbol{\tau}}_y| = \sqrt{\det \bar{C}_{\mathscr{M}}} = \bar{\Lambda}_1\bar{\Lambda}_2 \equiv F^{-1}\ , \tag{3.9}$$

where we have defined the quantity F which we call the *density factor*. It is a function of the trajectory that starts at $\mathbf{x}_0$ and arrives at $\mathbf{x} = \phi^z_{z_0}(\mathbf{x}_0)$, so that, with some abuse of language, it can be considered either as a function of the initial or of the final location: $F = F(\mathbf{x}_0)$ or $F = F(\mathbf{x})$. The name density factor comes from the consideration of the ratio between the density of particles in a release surface element, $\sigma(\mathbf{x}_0)$, and in its image in the collecting

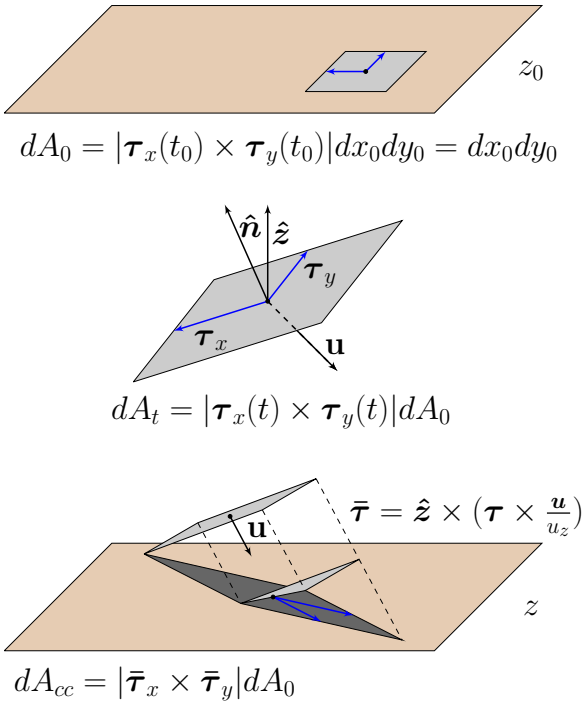

Fig. 3.1 Illustration of the dynamics of a rectangular surface element, lying on the upper layer at the release time t_0, and with area $\mathrm{d}A_0$, until leaving a footprint of area $\mathrm{d}A_{\mathrm{acc}}$ on the lower layer when arriving there. See main text and App. D for details.

layer $\sigma(\mathbf{x} = \phi^z_{z_0}(\mathbf{x}_0))$. In the situation in which both surface elements contain the same fluid particles, this ratio is the inverse of the ratio of areas, and thus equal to F:

$$\frac{\sigma(\mathbf{x})}{\sigma(\mathbf{x}_0)} = \frac{\mathrm{d}A_0}{\mathrm{d}A_{\mathrm{acc}}} = F. \tag{3.10}$$

The surface elements $\mathrm{d}A_0$ and $\mathrm{d}A_{\mathrm{acc}}$ will contain the same particles if a single surface element from the release layer reaches $\mathrm{d}A_{\mathrm{acc}}$. For time-dependent velocity fields, folding of the falling layer can occur, and in this case the complete density ratio should be computed as the sum of all contributions of the type (3.10) from the initial release areas $\mathrm{d}A_0$ that reach the same $\mathrm{d}A_{\mathrm{acc}}$ at different times (Drótos et al., 2019, Monroy et al., 2019, Sozza et al., 2020).

A convenient way to write $F = \mathrm{d}A_0/\mathrm{d}A_{\mathrm{acc}}$ is to split it into two contributions (Monroy et al., 2019, Drótos et al., 2019, Sozza et al., 2020) (see Fig. 3.1): the evolution of the surface element under the time map $\phi^{\omega}_{t_0}$ until when its area gets stretched to $\mathrm{d}A_{t_z}$ (recall that $t_z = t_0 + \omega$ is the time at which the infinitesimal surface touches the z layer), and the

projection of this surface element onto the horizontal collection layer along the direction of motion to leave a footprint of area $\mathrm{d}A_{\mathrm{acc}}$ there, completing with this the action of $\phi^z_{z_0}$:

$$F = \frac{\mathrm{d}A_0}{\mathrm{d}A_{t_z}} \frac{\mathrm{d}A_{t_z}}{\mathrm{d}A_{\mathrm{acc}}} = S\,P\,. \tag{3.11}$$

The stretching and projection factors, S and P, can be calculated as (Monroy et al., 2019, Drótos et al., 2019, Sozza et al., 2020):

$$S = \frac{\mathrm{d}A_0}{\mathrm{d}A_{t_z}} = \left|\boldsymbol{\tau}_x(t_z) \times \boldsymbol{\tau}_y(t_z)\right|^{-1}, \tag{3.12}$$

$$P = \frac{\mathrm{d}A_{t_z}}{\mathrm{d}A_{\mathrm{acc}}} = \left|\frac{u_z}{\hat{\mathbf{n}} \cdot \boldsymbol{u}}\right|, \tag{3.13}$$

where $\hat{\mathbf{n}}(t)$ is a unit vector normal to the falling surface element at time t, and the vectors $\boldsymbol{\tau}_x(t)$ and $\boldsymbol{\tau}_y(t)$ are tangent to the sinking surface $\mathrm{d}A_t$ at time t, given by $\boldsymbol{\tau}_x = \frac{\partial \phi^\tau_{t_0}(\mathbf{r}_0)}{\partial x_0}$ and $\boldsymbol{\tau}_y = \frac{\partial \phi^\tau_{t_0}(\mathbf{r}_0)}{\partial y_0}$. The expression for S is obtained simply by recognizing that $\boldsymbol{\tau}_x(t)\mathrm{d}x_0$ and $\boldsymbol{\tau}_y(t)\mathrm{d}y_0$ are the images under time evolution of the vectors $\hat{\boldsymbol{x}}\mathrm{d}x_0$ and $\hat{\boldsymbol{y}}\mathrm{d}y_0$, respectively, that make the initial surface, and thus the area at any time t is $\mathrm{d}A_t = |\boldsymbol{\tau}_x(t) \times \boldsymbol{\tau}_y(t)|\mathrm{d}x_0\mathrm{d}y_0$. A derivation of the expression for P is given in App. D, where further details on the projection process is given. As with λ_α, expression (3.12) is a property of the trajectory joining $\mathbf{x}_0$ and the corresponding $\mathbf{x}$ in the collecting layer, so that S can be considered as a function of any of these two locations. Eq. (3.13) involves velocities and the normal to the surface element at the collecting layer, so that it is more natural to consider $P = P(\mathbf{x})$, although for invertible $\phi^z_{z_0}$ the values of P can also be mapped back to the release layer and displayed there.

The density factor F can also be expressed in terms of singular values of a different Jacobian matrix. We begin with expressing the stretching factor S. First note that the Jacobian matrix in (3.3) has as columns the two vectors $\boldsymbol{\tau}_x(t)$, $\boldsymbol{\tau}_y(t)$, and the additional one $\boldsymbol{\tau}_z(t) = \frac{\partial \phi^\tau_{t_0}(\mathbf{r}_0)}{\partial z_0}$. Let $\boldsymbol{J}_{\mathscr{M}}$ be the 3×2 matrix having as columns just the three-dimensional vectors $\boldsymbol{\tau}_x(t)$, $\boldsymbol{\tau}_y(t)$. The subindex $\mathscr{M}$ indicates that it involves derivatives only along the horizontal release layer $\mathscr{M}$. The singular values of $\boldsymbol{J}_{\mathscr{M}}$, Λ_1 and Λ_2, are the square roots of the eigenvalues of the 2×2 matrix $C_{\mathscr{M}} = \boldsymbol{J}^T_{\mathscr{M}} \boldsymbol{J}_{\mathscr{M}}$. Simple algebra demonstrates that

$$S^{-1} = |\tau_x(t) \times \tau_y(t)| = \sqrt{\det C_{\mathscr{M}}} = \Lambda_1 \Lambda_2\,. \tag{3.14}$$

We stress that the quantities Λ_α are in general different from the singular values S_α of the 3×3 matrix $\boldsymbol{J}$ in Eq. (3.3), giving the Lyapunov exponents as $\lambda_\alpha = |\omega|^{-1} \log S_\alpha$. Λ_α characterizes stretching only of infinitesimal initial vectors lying on the horizontal initial

layer. But, in the limit of large t_z or $|z-z_0|$, vectors of arbitrary initial orientation are expected to approach the directions that stretch faster under the action of $\boldsymbol{J}$, so that we expect that in this limit Λ_α will approach S_α, for $\alpha = 1,2$. More in general, since $\boldsymbol{J}_{\mathscr{M}}$ is the matrix $\boldsymbol{J}$ with a column deleted, inequalities for singular values of submatrices (Horn and Johnson, 1991) lead to $S_{\alpha+1} \leq \Lambda_\alpha \leq S_\alpha$, with $\alpha = 1,2$.

Comparison of Eqs. (3.9), (3.11) and (3.14) gives the following relationship between the descriptions based on the singular values of $\bar{J}_{\mathscr{M}}$ and $J_{\mathscr{M}}$:

$$\bar{\Lambda}_1\bar{\Lambda}_2 = P^{-1}\Lambda_1\Lambda_2 = F^{-1}, \tag{3.15}$$

which also shows the two different ways to compute the density factor F.

3.4 The network approach

We now describe a characterization of fluid transport between layers by tools from network or graph theory. This type of approach can also be called *probabilistic*, or *set-oriented*. Our goal is to generalize studies such as (Froyland and Dellnitz, 2003, Ser-Giacomi et al., 2015a) by considering a bipartite network which is the natural framework to study two-layer transport. For this we construct the discrete version of the Perron-Frobenius operator describing the transport matrix between the two layers.

3.4.1 Coarse-graining of the flow and transport matrix

The upper layer is partitioned with a set of boxes $\{A_i\}_{i=1,\ldots,M_0}$, and the lower layer with boxes $\{B_j\}_{j=1,\ldots,M_z}$ (see Fig. 3.2). Each of these boxes is interpreted as a node in a bipartite network. Links between the upper and the lower layer are established by the action of the two-layer map. These links are directed and weighted, with weights between A_i in the upper layer and B_j in the lower one given by the proportion of area of A_i which is mapped onto B_j, which defines a transport matrix:

$$\mathbf{P}(z_0,z)_{ij} = \frac{\mu\left(A_i \bigcap \left(\phi_{z_0}^z\right)^{-1}(B_j)\right)}{\mu(A_i)}. \tag{3.16}$$

$\mu(S)$ is the measure of set S (a part of the release layer) here taken to be its area. The map $\left(\phi_{z_0}^z\right)^{-1}$ is the inverse of $\phi_{z_0}^z$, i.e. it takes points from the lower layer that at some moment were reached by the released particles and maps them back into the position they had at t_0 in the upper layer. Note that for time-dependent velocity fields this inverse map

can be multivalued, as several initial conditions $\mathbf{x}_0$ can reach the same point in the lower layer, provided they do so at different times. In this case, all preimages of box B_j should be considered in Eq. (3.16). From a practical point of view, one computes the matrix elements $\mathbf{P}(z_0,z)_{ij}$ by releasing a large number N_i of trajectories from box A_i at t_0, and counts how many of them, N_{ij}, reach the collecting layer for the first time at box B_j. The ratio N_{ij}/N_i estimates the value of $\mathbf{P}(z_0,z)_{ij}$ for N_i large enough.

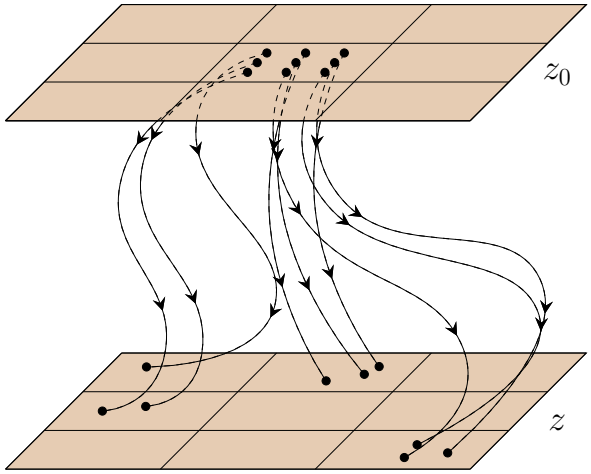

Fig. 3.2 Sketch of the bipartite network construction. Particles travel from the upper layer to the bottom one. Nodes are the boxes A_i, $i = 1,...,M_0$ on which the upper layer is partitioned, and B_j, $j = 1,...,M_z$, partitioning the lower one. Two nodes are linked if some trajectory joins them.

We note that the transport matrix $\mathbf{P}(z_0,z)$ is different from the one used in previous works in two aspects: first, it represents connections between two distinct regions: the release and the collecting layer, whereas the transport matrix used for example in (Froyland and Dellnitz, 2003, Ser-Giacomi et al., 2015a) quantifies the transport between boxes embedded in the same fluid region. This bipartite character of our transport matrix is shared by other operators in the literature, for example (Froyland et al., 2015), but then the second difference is that in those cases transport is computed during a fixed amount of time, whereas in our case what is fixed is the distance between the two layers, with possibly different times of transport between them for different fluid particles.

Eq. (3.16) immediately leads to a probabilistic interpretation: $\mathbf{P}(z_0,z)_{ij} \geq 0$ is the probability that a fluid particle started at t_0 in a uniformly random position in box A_i of the release layer reaches the collecting layer for the first time on box B_j. If all fluid particles

released from $\mathscr{M}$ reach the collecting layer, then $\mathbf{P}(z_0,z)_{ij}$ is row stochastic:

$$\sum_{j=1}^{M_z} \mathbf{P}(z_0,z)_{ij} = 1. \tag{3.17}$$

If some fluid particles never reach the collecting layer, then we can have $\sum_{j=1}^{M} \mathbf{P}(z_0,z)_{i,j} < 1$, being this the probability of reaching the lower layer if starting from a random position in the release one. As when dealing with open flows (Ser-Giacomi et al., 2017) one can consider the transport matrix that takes into account only the particles that do reach the second layer. The so-called *out-strength* of node i, defined as

$$S_{\mathrm{OUT}}(i) = \sum_{j=1}^{M_z} \mathbf{P}_{ij} \ , \tag{3.18}$$

can be used to formulate a general definition of the bilayer transport matrix, which is row-stochastic and valid for both closed and open flows (i.e. cases in which the collecting layer is always reached and cases in which it is not):

$$\mathbf{Q}_{ij} = \begin{cases} \frac{\mathbf{P}_{ij}}{S_{\mathrm{OUT}}(i)} & \text{if } S_{\mathrm{OUT}}(i) \neq 0 \\ 0 & \text{if } S_{\mathrm{OUT}}(i) = 0 \end{cases} . \tag{3.19}$$

In the following we indicate some relevant network measures that can be computed from this bipartite transport matrix.

3.4.2 Network measures

Many quantities have been introduced to characterize the topology and connectivity properties of networks (Newman, 2010). In this chapter we will not consider non-local quantifiers, such as optimal paths, betweenness or communities (Bollt and Santitissadeekorn, 2013, Ser-Giacomi et al., 2015a,b,c, 2021). We just introduce the simplest quantifiers involving single nodes, namely degrees and network entropy. The adjacency matrix is given by

$$A_{ij} = \begin{cases} 1 & \text{if } \mathbf{Q}_{ij} > 0 \\ 0 & \text{if } \mathbf{Q}_{ij} = 0 \end{cases} . \tag{3.20}$$

It is used to define the out-degree of a node i, $K_{\mathrm{OUT}}(i)$, i.e, the number of nodes in layer z receiving fluid from node i in layer z_0; and the in-degree for a node j, $K_{\mathrm{IN}}(j)$, which is the number of nodes of the release layer from which fluid content arrives at node j in the

collecting layer:

$$K_{\mathrm{OUT}}(i) = \sum_{j=1}^{M_z} A_{ij}, \tag{3.21}$$

$$K_{\mathrm{IN}}(j) = \sum_{i=1}^{M_0} A_{ij}. \tag{3.22}$$

Quantities related to degrees, but that take into account the actual proportion of particles arriving at each node (the *weights* of the links) are the out-strength defined in Eq. (3.18) and the *in-strength*:

$$S_{\mathrm{IN}}(j) = \sum_{i=1}^{M_0} \mathbf{P}_{ij} \, . \tag{3.23}$$

An alternative to S_{IN} can also be defined by using $\mathbf{Q}_{ij}$ instead of $\mathbf{P}_{ij}$. It coincides with (3.23) for closed flows, which is the case for the example presented later in this chapter.

Another quantity that takes into account the weights of the links is the network entropy, defined for each node i of the release layer as

$$H(i) = -\sum_{j=1}^{M_z} \mathbf{Q}_{ij} \log(\mathbf{Q}_{ij}). \tag{3.24}$$

Note that, at difference with previous references (Ser-Giacomi et al., 2015a), we have not introduced a prefactor corresponding to the inverse of the integration time in the definition (3.24).

3.5 Relationship between geometric and network characterization

For clarity, in the following we write expressions in terms of the matrix $\mathbf{P}_{ij}$, with the understanding that $\mathbf{Q}_{ij}$ should be used instead if the flow is open. We first obtain a relationship between the probabilistic or network approach and the geometric or dynamical one for the evolution of densities. Recall that $\mathbf{P}_{ij}$ is estimated as $\mathbf{P}_{ij} = N_{ij}/N_0$, where N_{ij} is the number of particles released from box A_i and landing on box B_j, provided N_0 particles are seeded from each release box (giving the same density σ_0 at each initial box if all of them have the same area). Then, $S_{\mathrm{IN}}(j)$, defined in (3.23), is estimated as $S_{\mathrm{IN}}(j) = N_j/N_0$, where N_j is the number of particles landing on box B_j irrespective of their origin. On the other hand, the average of the ratios of local densities $\sigma(\mathbf{x})/\sigma_0$ of the points inside a collecting box B_j,

$\langle\sigma(\mathbf{x})\rangle_{B_j} = \mu(B_j)^{-1}\int_{B_j} d\mathbf{x}\sigma(\mathbf{x})/\sigma_0$ is also estimated by N_j/N_0. These estimates become exact in the limit $N_0 \to \infty$. Using relationships (3.9) and (3.10) we find

$$S_{\mathrm{IN}}(j) = \lim_{N_0\to\infty} \frac{N_j}{N_0} = \langle F\rangle_{B_j} = \langle(\bar{\Lambda}_1\bar{\Lambda}_2)^{-1}\rangle_{B_j} \ , \tag{3.25}$$

where the left-hand side is computed from the network approach of Sect. 3.4, and the right-hand average is a coarse-graining of quantities from the geometrically based approach of Sect. 3.3. Note that Eq. (3.10) assumes the absence of folding processes producing multiple branches of arrival of the release layer onto the collecting one, so that this is also needed for the validity of (3.25).

We now suggest some network-geometric relationships similar to the ones developed in (Ser-Giacomi et al., 2015a) for single-layer Lagrangian flow networks. In particular, relationships between degree and network entropy on the one hand and the largest stretching factor and Lyapunov exponent on the other were found. These relationships were not exact ones, but approximate relationships that were checked to hold for the case of long times, sufficiently small network boxes, and a clear hyperbolic situation (i.e. Lyapunov exponents sufficiently larger or smaller than zero).

By repeating the heuristic arguments developed in (Ser-Giacomi et al., 2015a) we can find the following approximate relationships between the network and the geometrical description of our two-layer dynamics:

$$K_{\mathrm{OUT}}(i) \approx \left\langle\bar{\Lambda}\right\rangle_{A_i} = \left\langle e^{|z-z_0|\bar{\lambda}}\right\rangle_{A_i} \tag{3.26}$$

$$H(i) \approx \left\langle\log\bar{\Lambda}\right\rangle_{A_i} = |z-z_0|\left\langle\bar{\lambda}\right\rangle_{A_i} \ , \tag{3.27}$$

where $\bar{\Lambda}$ and $\bar{\lambda}$ are defined below. The averages perform a coarse-graining of the values of $\bar{\Lambda}(\mathbf{x}_0)$ or $\bar{\lambda}(\mathbf{x}_0)$ over all initial conditions inside the initial box A_i. At difference with the bidimensional situation considered in (Ser-Giacomi et al., 2015a), in which only one of the stretching factors was larger than one (a single expanding direction), in the present three-dimensional dynamics several directions can be expanding, and these directions are, in the arguments leading to Eqs. (3.26-3.27), the ones that contribute to the out degree K_{OUT} or to the network entropy H. In consequence, in Eqs. (3.26-3.27) we should use for every initial location $\bar{\Lambda} \equiv \prod_\alpha \bar{\Lambda}_\alpha$, where the product is over all factors Λ_α that satisfy $\Lambda_\alpha > 1$ at that point. Or, equivalently, $\bar{\lambda} \equiv \sum_\alpha \bar{\lambda}_\alpha$, where the sum is over all positive FDLEs, $\bar{\lambda}_\alpha > 0$, at that point.

We stress that relationships (3.26-3.27) are not exact, but we expect them to be satisfied for sufficiently small network boxes, large $|z-z_0|$, and dynamics sufficiently hyperbolic,

which roughly requires $\bar{\Lambda}_\alpha$ sufficiently different from unity. We will check this validity for a particular flow model in Sect. 3.7.5.

3.6 Bipartite network communities

As pointed out in Sec. 3.4, the network approach is defined by partitioning each layer into regular boxes. This coarse-graining allows a natural network description of the two-layer map given by the Perron-Frobenius operator, **P**, which defines flow connections between nodes of different layers. In this case, links are directed (from the upper to bottom layer) and the weight quantifies the proportion of fluid from boxes in the upper layer mapped to boxes in the collecting layer. The probabilistic interpretation of this transport matrix is derived in Sec. 3.4.

Set-oriented approaches identify a partition of the fluid domain into regions of different dynamical behaviour, the so-called coherent regions (Froyland et al., 2010, Santitissadeekorn et al., 2010). These regions are characterized by the large-scale properties of the flow. In terms of networks, they have high intraconnectivity between their nodes and low interconnectivity between them, resulting in almost isolated subnetworks. Similarly to other structures in time-dependent flows, these regions are not fixed in time, but rather they move with the flow. Coherent regions have been previously identified as communities in two-dimensional incompressible flows (Ser-Giacomi et al., 2015a). Altough different methods for community detection such as spectral partitioning may identify almost isolated regions (Danon et al., 2005, Lancichinetti and Fortunato, 2009), the additional condition of high internal mixing requires specific approaches. In this line, the *Infomap* algorithm assumes such condition and has a clear interpretion in flow networks, as pointed out in (Ser-Giacomi et al., 2015a).

The *Infomap* algorithm minimizes a cost function based on random walkers moving according to the transition probabilities between nodes. It searches for the best network partition given the inter and intraconnectivity between nodes (Rosvall and Bergstrom, 2008) (see Sec. 1.6.4). For two-dimensional incompressible flows, transition probabilities are associated to the transport matrix $\mathbf{P}(t_0, \tau)$ of Eq. 1.9, which has a direct probabilistic interpretation. For bipartite networks, one common approach consists in analyzing the community structure of each mode of the bipartite network (Zhou et al., 2007, Ramasco and Morris, 2006, Newman, 2004a). However, this method results in a loss of structural information if one is interested in finding common community structures between modes and an integration of communities in the whole bipartite system (Everett and Borgatti, 2013, Melamed, 2014). In such cases, a simultaneous search of communities of both networks is performed by using combina-

torial techniques that link communities of each individual network, as the dual-projection (Melamed, 2014, Newman and Girvan, 2004, Guimerà et al., 2007, Barber, 2007). Here we use the first approach, and analyze the community structure at each individual layer using the two one-mode projections. We argue that a loss of information in one-mode projections is not relevant for our propouse, since we are interested in the independent community structure at each layer, and it has a clear interpretation in terms of fluid networks. Further research in the exploration of other possible projections may be useful to characterize other connectivity properties.

The two one-mode networks are mathematically described as the projection of the transport matrix $\mathbf{P}_{ij}$ onto each layer:

$$\begin{aligned} \mathbf{M}^{Out} &= \mathbf{P}\mathbf{P}^T \\ \mathbf{M}^{In} &= \mathbf{P}^T\mathbf{P}. \end{aligned} \tag{3.28}$$

These matrices provide connections between nodes located in the same layer, with $\mathbf{M}^{Out}$ defining links between nodes in the upper layer and $\mathbf{M}^{In}$ between nodes in the bottom layer. At a difference from $\mathbf{P}$, the links are now undirected and the weights lose a probabilistic interpretation. Thus, both one-mode projections, $\mathbf{M}^{Out}$ and $\mathbf{M}^{In}$ are symmetric, and are neither row stochastic nor column stochastic. Furthermore, these matrices do not share identical information, mathematically illustrated from the fact that $\mathbf{P}\mathbf{P}^T \neq \mathbf{P}^T\mathbf{P}$. From one side, the one-mode matrix $\mathbf{M}^{Out}$ defines connectivity patterns between nodes in the upper layer, and links quantify the amount of fluid density shared by each pair of boxes when being collected at the second layer. In other words, an undirected link gives the probability that trajectories from two locations chosen randomly in the two nodes end up in the same location at the collecting layer. Analogously, the one-mode matrix $\mathbf{M}^{In}$ defines connections in the collecting layer, and quantifies the amount of fluid with common initial releasing source.

Coherent regions are identified at each layer finding the optimal community structure given the matrices $\mathbf{M}^{Out}$ and $\mathbf{M}^{In}$. We apply the *Infomap* algorithm using each one-mode projection as undirected transition rates between nodes belonging at a given layer. A direct consequence of the inequality between both one-mode projections is that communities of each layer are not necessarily connected to each other. Following the community characterization of (Ser-Giacomi et al., 2015a), we extend some concepts from network theory to define two quantifiers that test the quality of each network partition, the *outwards (inwards) coherence ratio* and the *outwards (inwards) mixing parameter*. In the following we use specific notation

to refer to sets of boxes. We first denote by Z_0 and Z_f the set boxes at the releasing and collecting layers, repectively. Then, the set of indices I correspond to all boxes making the upper layer, $Z_0 = \cup_{i\in I} A_i$. Analogously, the set of indices K correspond to boxes making the collecting layer, $Z_f = \cup_{k\in K} B_k$. We also denote by $M \subseteq I$ the subset of boxes making a set $A = \cup_{m\in M} A_m$. We define the *outwards transport matrix* as the normalized version of $\mathbf{M}_{ij}^{Out}$:

$$\bar{\mathbf{P}}_{ij} = \frac{\sum_{k\in K} \mathbf{P}_{ik}\mathbf{P}_{jk}}{\sum_{l\in I}\sum_{k\in K} \mathbf{P}_{ik}\mathbf{P}_{lk}} = \frac{\mathbf{M}_{ij}}{\sum_{l\in I}\mathbf{M}_{il}}, \tag{3.29}$$

for each pair of boxes $i, j \in I$. This matrix is not symmetric, defining directed and weighted links, with a probabilistic interpretation:

$$\begin{aligned} \bar{\mathbf{P}}_{ij} &\leq 1,\ \forall i, j \in I \\ \sum_{j\in I} \bar{\mathbf{P}}_{ij} &= 1,\ \forall i \in I. \end{aligned} \tag{3.30}$$

The outwards coherence ratio for a set A is defined as

$$\rho_{z_0}^{z}(A) = \frac{\sum_{i,j\in I} \mu(A_i)\bar{\mathbf{P}}_{ij}}{\sum_{i\in I}\mu(A_i)}. \tag{3.31}$$

For a given parition of the releasing layer into p communities, $P = \{A_1, ..., A_p\}$, the global outwards coherent ratio reads as

$$\rho_{z_0}^{z}(P) = \frac{\sum_{i=1}^{p} \mu(A_i)\rho_{z_0}^{z}(A_i)}{\sum_{i=1}^{p}\mu(A_i)}, \tag{3.32}$$

where we have weighted communities according to their size. A coherence value close to one indicates a good community partition. In terms of fluid networks, a good partition means that the application of the two-layer map over each community results in almost-isolated collecting areas in the bottom layer.

We also provide a measure for the internal mixing occurring inside communities, which quantifies how strongly the two-layer map mixes particles inside communities. We first define the transport matrix conditioned to a set A (we recall that M denotes the set of indices

making A):

$$\bar{\mathbf{R}}_{ij}(A) = \frac{\sum\limits_{k\in K} \mathbf{P}_{ik}\mathbf{P}_{jk}}{\sum\limits_{m\in M}\sum\limits_{k\in K} \mathbf{P}_{ik}\mathbf{P}_{mk}} = \frac{\mathbf{M}_{ij}}{\sum\limits_{m\in M} \mathbf{M}_{im}}, \tag{3.33}$$

for all $i, j \in M$. This matrix also defines directed links between nodes and has a probabilistic intepretation inside A. The entropy of the transition probabilities defined in $\bar{\mathbf{R}}$ provides a natural description of mixing, which we use to define the *outwards mixing rate* of a set A:

$$m^z_{z_0}(A) = \frac{-\sum\limits_{i,j\in M} \bar{\mathbf{R}}_{ij} log \bar{\mathbf{R}}_{ij}}{|A| log(|A|)}, \tag{3.34}$$

where $|A|$ denotes the size of A. A value close to one indicates a high internal mixing occurring inside A. The global mixing rate defined for a community partition P is given by

$$m^z_{z_0}(P) = \frac{\sum\limits_{i=1}^{p} \mu(A_i) m^z_{z_0}(A_i)}{\sum\limits_{i=1}^{p} \mu(A_i)}. \tag{3.35}$$

While these two quantifiers provide a good test fot the quality of a given community partition at the releasing layer, we define similarly the *inwards coherence rate* and *inwards mixing rate*, which are quantifiers for the quality of community partition in the collecting layer. The mathematical description of such quantifiers is analogous to the previous formalism, with a simple reversal of indices between boxes and sets of boxes of both layers. Similarly, values of coherence and mixing close to one would indicate a good community partition of the collecting layer, where each community would be mapped from an almost-isolated but well mixed fluid area source in the releasing layer.

3.7 Numerical results

In this section we illustrate the previous concepts with a slightly modified version of an idealized incompressible three-dimensional flow, the ABC flow. Application of the network communities formalism of the last section however will be delayed until application to the Canary island flow described in the next Chapter.

3.7.1 ABC flow model

The ABC flow is a 3d model flow which is widely used for analyzing chaotic transport (McMillen et al., 2016, Dombre et al., 1986). It provides a simple stationary solution of Euler's equation for incompressible, inviscid fluid flows.

To simulate the situation of particles going from one layer to another, we modify the ABC flow with a drift in a preferential direction, specifically in the vertical one (z-direction), without changing most of the properties of the flow. The motivation for this choice is to mimic in a very simple way the transport of particles falling under gravity in a chaotic fluid flow. The equations describing the model are

$$\dot{x} = u_x = A\sin z + C\cos y, \tag{3.36}$$

$$\dot{y} = u_y = B\sin x + A\cos z, \tag{3.37}$$

$$\dot{z} = u_z = C\sin y + B\cos x + D. \tag{3.38}$$

We take $A = 1, B = \sqrt{2}, C = \sqrt{3}$ for which chaotic motion is found (Dombre et al., 1986). The new constant $D = -3.15$ is the one giving a contribution to the velocity pointing downwards. Its value is just sufficient to keep the particles to travel downwards in the z direction (thus, $u_z < 0$ for any particle at any time). Among other consequences, this guarantees that all initially released trajectories will reach the collecting layer at some time, so that $S_{\mathrm{OUT}} = 1$ in Eq. (3.25). In the horizontal coordinates the fluid domain is $x, y \in [0, 2\pi]$ with periodic boundary conditions. In the vertical (z-coordinate) particles are released from the layer $z_0 = 10$ and are followed until they reach the layer at coordinate z where integration is stopped. Thus the model is defined in the vertical interval $[z, z_0]$.

Note that $\nabla \cdot \boldsymbol{u} = 0$. The facts that $u_z < 0$ and that the flow is time-independent guarantees that the map $\phi_{z_0}^z$ is one-to-one.

3.7.2 Transport properties between layers

We first study the map $\phi_{z_0}^z$ for the ABC flow by taking $z_0 = 10$ and $z = 0$ (particles fall from height z_0). In Fig. 3.3 we show a histogram of arrival times, $p(\omega)$. It shows a two-peaked shape with peaks around the values 2 and 6. We can differentiate two main dynamical behaviors: more laminar for the first peak and more chaotic for the second one. This suggests the existence of two zones of trajectory behavior in the fluid flow, which is confirmed in Figure 3.4.

We show in Figure 3.4 the spatial distribution of ω, the time needed by every particle to go from layer z_0 to layer z. This time is shown as a color map for every particle at the release

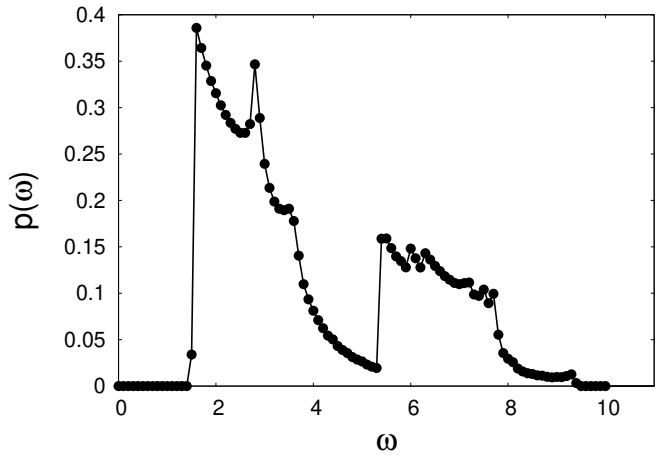

Fig. 3.3 Histogram of the times to reach the second layer at $z = 0$, starting from $z_0 = 10$.

layer z_0 and on its corresponding final position at layer z. The color map in the bottom layer is conveniently computed by running the flow backwards in time from a regular grid of initial conditions located at z. The equivalence between the backwards- and the forward-in-time calculation of t_z is guaranteed by the fact that for this time-independent flow the map $\phi_{z_0}^z$ is one-to-one. Since $u_z < 0$ for any particle and time, all particles released in the upper layer reach the collecting layer in a finite time, and all locations in the collecting layer receive a trajectory.

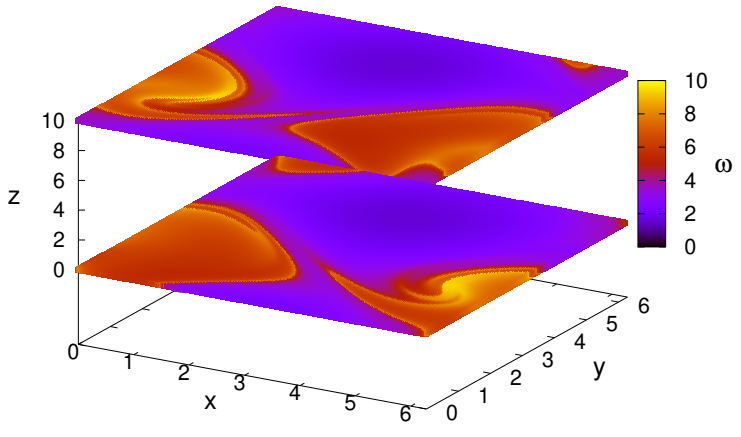

Fig. 3.4 The travel time, ω, from release layer ($z_0 = 10$) to collecting layer ($z = 0$) displayed at the initial and final position of each particle.

We observe the two regions in Fig. 3.4: the first peak in Figure 3.3 corresponds the dark regions, with more laminar trajectories, i.e., the particles go straightforwardly from one layer to the other; and the red regions correspond to the second peak and to more convoluted (chaotic) trajectories. The frontiers between initial conditions of large and small t_z are quite sharp, and will be identified with lines of large finite-depth Lyapunov exponent in Section 3.7.3.

3.7.3 Geometric characterization

The Jacobian $\bar{\boldsymbol{J}}_{\mathscr{M}}$ is computed by releasing particles on a regular grid on layer z_0, integrating their trajectories under the modified ABC flow until reaching the final layer at z, and approximating the derivatives in $\bar{\boldsymbol{J}}_{\mathscr{M}} = \nabla\phi_{z_0}^{z}(\mathbf{x}_0)$ by finite differences between final positions of initially neighboring particles. Then, its singular values $\bar{\Lambda}_1$ and $\bar{\Lambda}_2$ are computed after construction of the Cauchy-Green tensor $\bar{C}_{\mathscr{M}} = \bar{\boldsymbol{J}}^T_{\mathscr{M}}\bar{\boldsymbol{J}}_{\mathscr{M}}$.

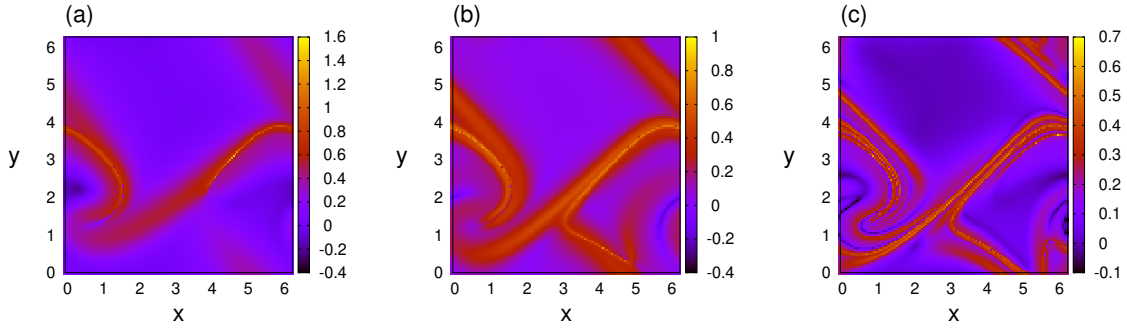

Fig. 3.5 Maximal FDLE $\bar{\lambda}_1$ for dynamics under the modified ABC flow, displayed at the initial particle locations in the release layer $z_0 = 10$, and for collecting layer at (a) $z = 2\pi$, (b) $z = 4$ and (c) $z = 0$.

Figure 3.5 shows the maximal FDLE $\lambda_1(\mathbf{x}_0)$ from Eq. (3.7), displayed on the release layer $z_0 = 10$, for collecting layers at three different depths z. We see that increasingly finer filamentary structures appear for increasing travel depth. This is similar to the behavior of the FTLE for increasing integration time. We note that the highest FDLE values roughly divide the release domain into two regions (remember the periodic boundary conditions in the horizontal directions) that closely correspond to the long and short travel time regions in Fig. 3.4: as for the FTLE, ridges of FDLE are associated with separatrices that divide the release layer into regions of different dynamic behavior.

In Figure 3.6a we plot the factor F on the collecting layer, which is the factor that multiplies the initial density at the release layer (and thus it is proportional to the accumulated

density of particles if the release density is constant). We also display in the other panels of Fig. 3.6 the two geometric factors, stretching S and projection P, that shape F (i.e. $F = S\,P$, Eq. (3.11)). We see clearly from the plot of F that filamentary structures will appear in the density collected in the lower layer. The effect of surface-element stretching (S) is less determinant for F than the projection of surface elements onto the collecting layer, P, although this can be different for other types of flows. In more complex flows (Drótos et al., 2019, Monroy et al., 2019, Sozza et al., 2020) the projection factor can even diverge at *caustics*, locations where the denominator of Eq. (3.13) vanishes. As in (Drótos et al., 2019), there is some degree of anticorrelation between S and P, so that the fluctuations in F are smaller than those in S and P.

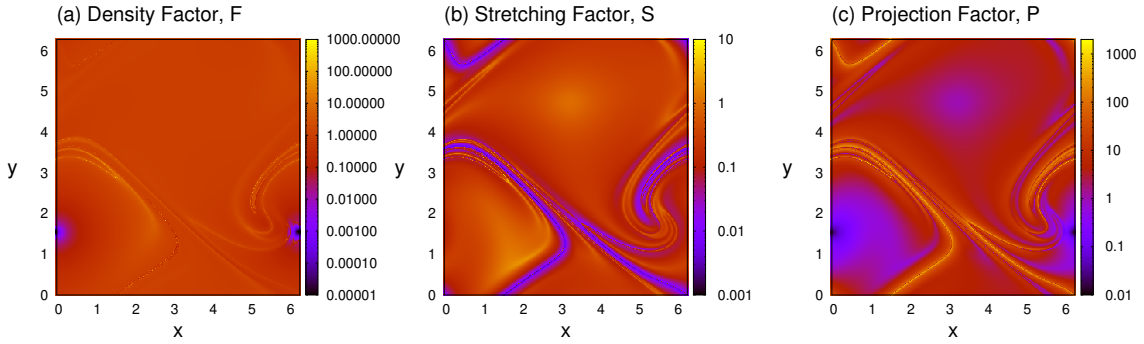

Fig. 3.6 (a) The density factor, F, computed as $F = (\bar{\Lambda}_1\bar{\Lambda}_2)^{-1}$ at the collecting layer $z = 0$, giving the relative density of collected particles if the density in the release layer $z_0 = 10$ is uniform. Panel (b) shows the stretching factor S, computed as $S = (\Lambda_1\Lambda_2)^{-1}$. Panel (c) shows the projection factor P from Eq. (3.13). We have checked that $F = S\,P$ to good accuracy. Note the logarithmic scale in the color maps.

3.7.4 Network characterization

We study connectivity properties between layers $z_0 = 10$ and $z = 0$. For doing this, we divide the upper layer into 100×100 square boxes $A_i,\ i = 1, ..., 10000$, and the lower one into 100×100 square boxes $B_j,\ j = 1, ..., 10000$. Then we release from each box in z_0 900 particles uniformly distributed. We integrate each of these particles with the map $\phi_{z_0}^{z}$ (equivalent to integrating Eq. (3.1) until reaching the collecting layer at z).

In Figure 3.7 we show the out-degree in the starting layer and the in-degree in the final one. The out-degree for a given box in the starting layer indicates the number of boxes reached in the final layer. It is a measure of dispersion, and large values at a box indicate that a part of a repelling or dispersing structure is present there. On the other side, large values of

in-degree in the final layer indicate mixing from a large number of different initial conditions, so that boxes with in-degree maxima trace the location of attracting regions. These ideas are confirmed when comparing degrees to the FDLEs of Fig. 3.5c.

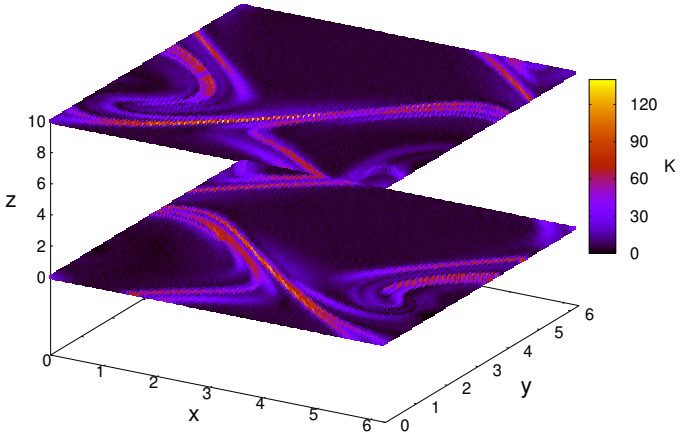

Fig. 3.7 Out-degree and in-degree in the release ($z_0 = 10$) and the arrival ($z = 0$) layers, respectively.

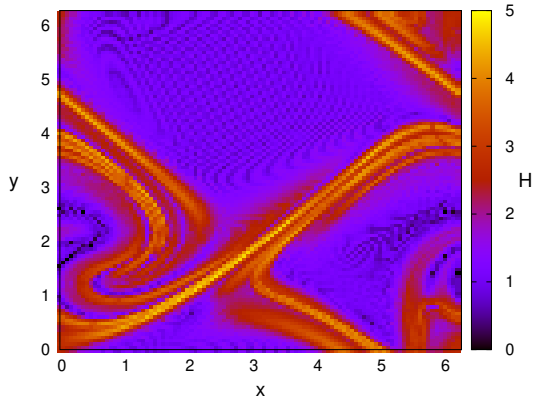

Fig. 3.8 Entropy $H(i)$ for transport from the release layer at $z_0 = 10$ to the collecting layer at $z = 0$, displayed on the release layer.

Another quantity computed in the network approach, the entropy $H(i)$ defined in Eq. (3.24) is displayed in Fig. 3.8. There is a clear relationship with $K_{\mathrm{OUT}}(i)$ (Fig. 3.7), and also with the FDLEs of Fig. 3.5c. These relationships will be checked more systematically in the next section.

3.7.5 Relationship between geometric and network characterization

In this section we first check Eq. (3.25). It relates the network quantity $S_{\mathrm{IN}}(j)$, giving also the density accumulated at box B_j in the lower layer relative to the uniform release density in the upper layer, to a coarse graining on collecting boxes of a quantity developed in the geometric approach, the density factor $F = (\bar{\Lambda}_1\bar{\Lambda}_2)^{-1}$. In Fig. 3.9 we see that, as predicted, both quantities are nearly equal, although there are some differences in the narrowest filamental regions, arising from numerical inaccuracies. According to the outlying values in Fig. 3.9b, it is presumably S_{IN} that can be computed more reliably than $(\bar{\Lambda}_1\bar{\Lambda}_2)^{-1}$.

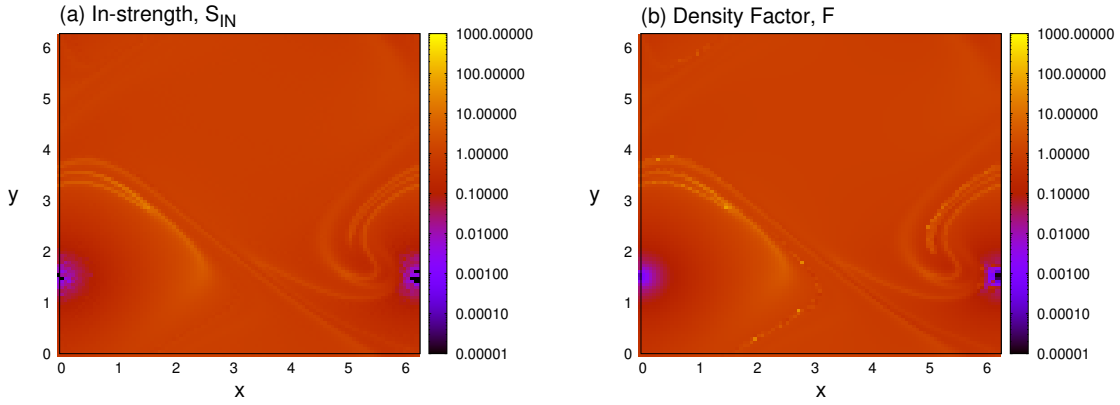

Fig. 3.9 (a) The in-strength $S_{\mathrm{IN}}(j)$ in the lower layer $z = 0$, which gives the accumulated density in that layer starting from a unit-density uniform release at $z_0 = 10$. (b) Density factor averaged on each box of the accumulation layer, i.e. $\langle F\rangle_{B_j} = \langle(\bar{\Lambda}_1\bar{\Lambda}_2)^{-1}\rangle_{B_j}$.

We now address the validity of expressions (3.26) and (3.27). At difference with Eq. (3.25), these formulae were derived only heuristically, following the arguments of Ref. (Ser-Giacomi et al., 2015a). Their validity is subjected to restrictions such as smallness of boxes, large values of $|z - z_0|$, and sufficiently hyperbolic dynamics (roughly, singular values sufficiently different from unity), which we will now check if are satisfied for our modified ABC flow.

Regarding Eq. (3.26), comparison of K_{OUT} from the upper layer in Fig. 3.7, and $\bar{\lambda}_1$ in Fig. 3.5c, which is the logarithm of $\bar{\Lambda}_1$, already indicates a strong relationship. A more quantitative comparison is made in panel (a) of Fig. 3.10 between $K_{\mathrm{OUT}}(i)$ and $\langle\bar{\Lambda}\rangle_{A_i}$, where $\Lambda = \prod_\alpha \bar{\Lambda}_\alpha$ and the product multiplies the singular values larger than unity. We see that, although there is a positive correlation, there is no identity between the two quantities. We attribute this failure of Eq. (3.26) to the fact that the second singular value $\bar{\Lambda}_2$ takes values close to unity for most of the trajectories. This is confirmed by the distribution of $\bar{\Lambda}_2$ in the upper layer displayed in Fig. 3.11. We note that, since the modified ABC flow is time

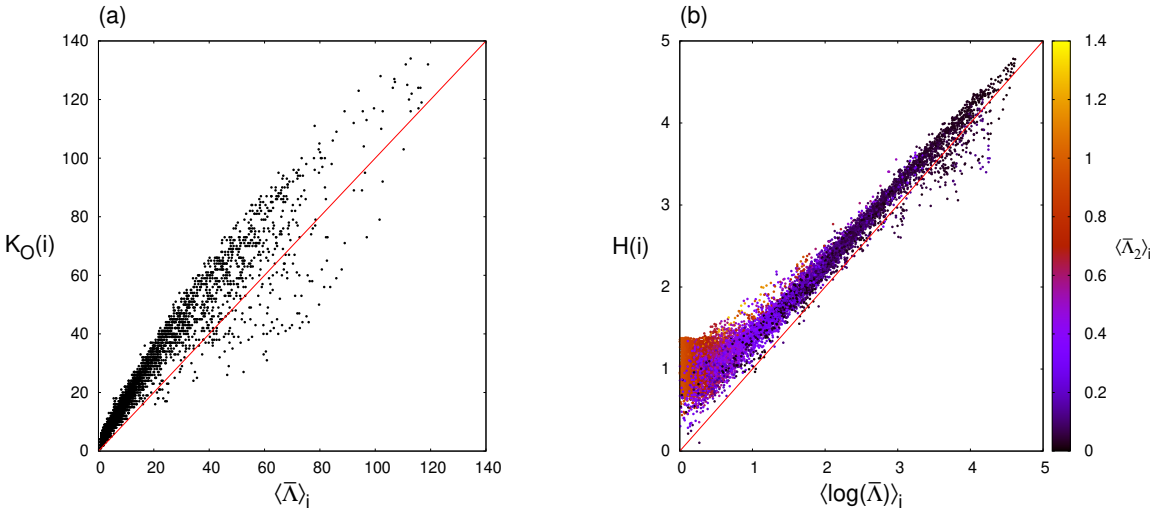

Fig. 3.10 (a) Scatter plot of values of $K_{\rm OUT}(i)$ vs $\langle\bar{\Lambda}\rangle_{A_i}$. The red diagonal indicates the fulfillment of Eq. (3.26). (b) Scatter plot of values of $H(i)$ vs $\langle\log\bar{\Lambda}\rangle_{A_i}$. The red diagonal indicates the fulfillment of Eq. (3.27). Dots are colored according to the value of $\langle\bar{\Lambda}_2\rangle_{A_i}$.

independent, we have always that the second Lyapunov exponent is zero, or $S_2 = 1$. The three-dimensional singular value S_2 is not exactly Λ_2 nor $\bar{\Lambda}_2$, but it is related to them at long times, which justifies the prevalence of values $\bar{\Lambda}_2 \approx 1$ in Fig. 3.11, and then a lack of hyperbolicity. $\bar{\Lambda}_2 \approx 1$ implies that boxes in the upper layer are not converted by the dynamics into thin filaments, but into broad strips. When reaching the collecting layer, they will leave a footprint larger than the thin filament needed to derive Eq. (3.26), and consequently $K_{\rm OUT}$ will be generally larger than predicted, as seen in Fig. 3.10a.

Relationships that imply a weighting with the number of particles reaching a particular box in the collecting layer are expected to be more robust than relations such as Eq. (3.26) that involve the degree, a quantity counting all boxes to which particles arrive, independently on how many of them do so. Thus, Eq. (3.27), although derived under heuristic arguments similar to those leading to Eq. (3.26), is expected to be satisfied under a broader range of conditions. This in indeed the case, as seen by comparing plots of entropy (Fig. 3.8) with corresponding plots of FDLE (Fig. 3.5c). A more quantitative check is performed in panel (b) of Fig. 3.10. We see that the equality in Eq. (3.27) is satisfied much better than Eq. (3.26). Nevertheless, there are still deviations, especially for small values of $\langle\log\bar{\Lambda}\rangle_{A_i}$. These small values arise from locations where $\bar{\Lambda} \approx 1$, confirming situations of lack of hyperbolicity. We have also colored the points in the scatter plot with the values of $\langle\bar{\Lambda}_2\rangle_{A_i}$. Again, the stronger deviations occur when both $\langle\bar{\Lambda}_2\rangle_{A_i}$ and $\langle\bar{\Lambda}\rangle$ are close to unity.

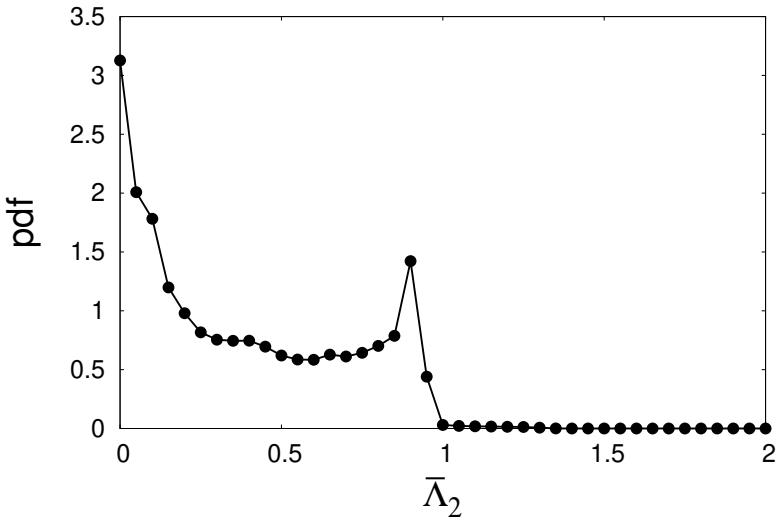

Fig. 3.11 Probability density function of the values of $\bar{\Lambda}_2$ on the release layer.

3.8 Conclusions

In this chapter we have developed a formalism to characterize transport of particles between two layers in a fluid. The motivation was to obtain a theoretical framework to analyze problems related to the sinking of particles in fluid flows, sedimenting towards a bottom layer. Two complementary sets of tools have been addressed: geometrical or dynamical, by studying the dynamics and deformation of a layer of particles, and probabilistic, using concepts from network theory. Most importantly, we have addressed the relationship between these two approaches, and illustrated the whole formalism with a modified ABC model.

The crucial step is the definition of a two-layer map, which drives particles from one initial layer to the final one. Within the geometric approach we have analyzed the deformation of surfaces and lines of particles released from the upper layer. A quantity related to the Lyapunov exponent, the FDLE, has been defined and related to the quantities above. Within the probabilistic methodology the natural description of the system is via bipartite networks, in which quantities such as the out-degree in the initial layer and the in-degree in the final one acquire a clear physical meaning. Both descriptions have been connected, for example, by expressing the accumulated density of particles in terms of the in-degree and of averages of singular values defined in the geometric approach. Other geometric-network relationships that were successfully tested for transport on a single layer (Ser-Giacomi et al., 2015a) are satisfied here with poor accuracy. This stresses the need for sufficiently hyperbolic dynamics to justify some of the heuristic steps used in the derivations. Finally, a formalism is developed

to identify network communities associated to the two-layer map, which is applied to the Canary Island basin in the next Chapter.

There are recent works studying, on the one side, microplankton sedimentation in the ocean with network tools (Nooteboom et al., 2019) and, on the other, the geometry of sedimentation dynamics and distribution of biogenic particles (Monroy et al., 2017, 2019) and microplastics (de la Fuente et al., 2021b). The steps presented here to connect both approaches will provide new insights into problems of sinking particles in the ocean. This will be also relevant for studies of sedimentation in atmospheric flows, as for example in the context of deposition of volcanic ashes or aerosol particles (Haszpra and Tél, 2011, Haszpra, 2019). More generally, we expect our formalism to be of use in other flow problems in which a clear direction of transport occurs.

Chapter 4

Vertical structure of transport of sinking particles: A case study in the Canary Islands

4.1 Introduction

In this Chapter we proceed to the application of the vertical transport characterization described in Chapter 3 to idealized sinking particles released in the Canary islands basin. We first introduce previous results related to the oceanography in this region. Then, we apply our model based on the two-layer map and analyze dynamical properties of particles and connectivity patterns taking place in the Canary basin. In particular, we use concepts from dynamical systems to analyze the horizontal dispersion of particles when reaching a given deeper layer, by applying the FDLE. We also check within this realistic flow the identities derived in Chapter 3 that relate the geometrical and network approaches. As a novelty, we use bipartite networks to identify communities at each layer depth as almost isolated regions.

4.2 Oceanography of the Canary Islands basin

The Canary islands basin is of specific interest because it shows crucial instabilities as a result of strong interactions between fronts, the upwelling system and the topography structure. As a result, it is a region characterized by strong mesoscale variability. The main large-scale circulation patterns influencing the flow transport are illustrated skematically in Fig. 4.1. The Canary basin is a complex region dominated by the anticyclonic eastern subtropical gyre. It follows the eastward-flowing Azores current, which crosses the Madeira Island, within a

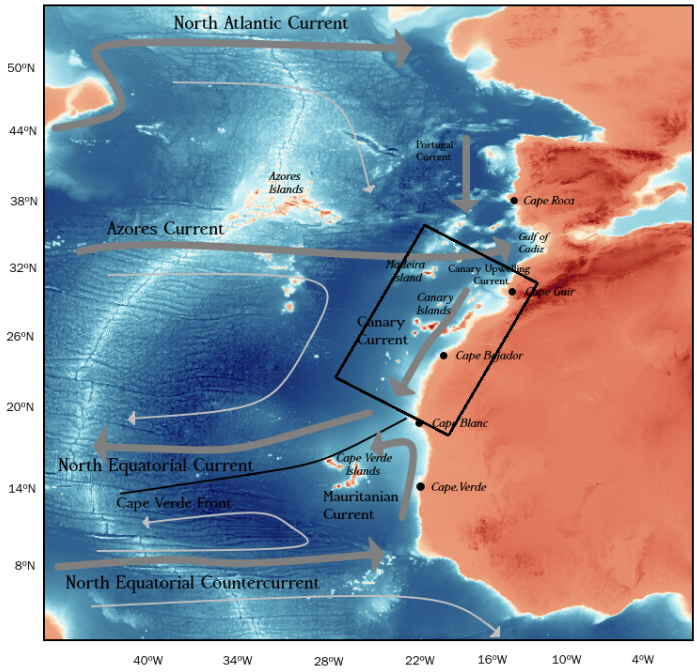

Fig. 4.1 Large-scale circulation in the Canary islands basin

recirculation through the Canary current until going further away from the coast following the North Equatorial current in westward direction. The pathways to the islands are not well-defined, but a dominant northwest entrance of waters in summer is reported Mason (2009). Islands act as a barrier to the influx of the Canary current, with the appearance of island-generated mesoscale eddies and extended filaments (Arístegui et al., 2009, Mason, 2009). This activity is associated to a strong vorticity around the islands countour, which generates high vertical velocities (Arístegui et al., 1994, Álvaro Peliz et al., 2002). Eddies are estimated to be about 50 km and up to 270 m deep (Arístegui et al., 1994). The well-known Canary Eddy Corridor was identified from altimetry data as a corridor of persistent eddies being transported offshore from the Canary islands (Sangrà et al., 2009). It shows long-lived eddies with a seasonal dependence. Specifically, eddies are generated at the African coast during all year and are intensified in autumn and winter, while island-generated eddies appear to be dominant in summer.

On the other hand, the Canary upwelling system is present almost all year, with strongest activity in summer (Wooster et al., 1976), and is one of the most important regions of biological production (Hailegeorgis et al., 2020, Arístegui et al., 2001). It has been reported the formation of filamentary structures of hundred of kilometers carrying cold waters rich

in nutrients up to the photic zone at latitudes of Cape Guir and Cape Bojador (Sangrà et al., 2009, Arístegui et al., 2001), mainly associated to oceanic instabilities of the upwelling system (Pelegrí et al., 2005). This system is conected to the Canary Eddy Corridor, which spans zonally in the west direction carrying potent mass of biological primary production and carbon from the Canary Upwelling region to the open ocean. Specifically, this corridor has been estimated to transport more than 0.25% of the southward path of the Canary Current.

High vertical transport is reported to exist at the eddy boundaries and fronts, enhancing the exchange of nutrients from cold and deep waters to the photic zone. In particular, there are fronts and eddies that dissipate in short temporal scales, but whose vertical velocities are larger than typical ones associated to mesoscale structures (Bakun and Nelson, 1991). There are three main vertical waters in the Canary basin (Mason, 2009). The central waters expand from the surface to the main thermocline, which is located between 200 and 1000 meters depth, generally above 600 m. This water mass is mainly wind-driven, where instabilities generated by the subtropical gyre result in strong vertical mixing that homogenizes the superficial waters, specially in winter. The intermediate waters are under the central waters, at a maximum depth of 1500 m. Finally, the deep waters extend up to 4000 m.

We are specifically interested in the transport structure of particles present in the Canary basin. There is high horizontal variability in particle distribution (Neuer et al., 2002), which is commonly associated to changes in biogenic particle concentration in superficial waters (Fischer et al., 2020). However, the vertical profile shows a most robust distribution, with an increase of particle concentrations for deeper waters (Neuer et al., 1997). A first hypothesis for this vertical distribution was that fast sinking particles drag smaller particles and contribute to an increasing particle concentration with depth, but some studies pointed out that there is no evidence for a predominance of this effect and remark other processes that are involved, such as aggregate formation and remineralization for slower particles (Omand et al., 2020, Riley et al., 2012, Collins et al., 2015). Instabilities in the coastal upwelling system are predominant in autumn, which develop into filamentary structures of cold water that flow offshore until reaching deeper waters in the open ocean (Fischer et al., 2020, Pelegrí et al., 2005, Álvarez Salgado et al., 2008), exporting large amounts of organic material (Pelegrí et al., 2005, Sangrà et al., 2009). Recent studies point out that the Canary current is characterized by higher lateral export than previous estimates, being more susceptible for slower particles. This lateral transport, for which 90% of exported fresh material is in dissolved form, is intensified by the filaments of cold water. Particle flux has high seasonality,

with maximum flux rates of lateral transport taking place in late winter and early spring (Neuer et al., 1997). Some modelling studies can be seen in Sandulescu et al. (2006, 2007).

4.3 Numerical procedure

We focus on theoretical particles for which the dynamics is well approximated by the equation:

$$\mathbf{v}(\mathbf{r}(t),t) = \mathbf{u}(\mathbf{r}(t),t) + \mathbf{v}_s, \tag{4.1}$$

where the parameters correspond to the settling velocity, $\mathbf{v}_s = (1-\beta)\mathbf{g}\tau_p$, the particle's buoyancy, $\beta = \frac{3\rho_f}{2\rho_p+\rho_f}$, and the Stokes time, $\tau_p = \frac{a^2}{3\beta\nu}$. It is an approximation of the simplified Maxey-Riley-Gatignol (MRG) equation (Maxey and Riley, 1983, Gatignol, 1983) for spherical particles with sufficiently small size and negligible inertial effects (Monroy et al., 2017, de la Fuente et al., 2021b). Further details in the derivation of Eq. (4.1) is given in Monroy et al. (2017) and is also explored in Chapter 2 for sinking microplastic particles.

We focus on the subdomain remarked by a black box in Fig. 4.1, which is considered as one of the subregions with a particular large-scale circulation (Arístegui et al., 2009). The three-dimensional velocity field of the fluid $\mathbf{u}$ is computed from ROMS (Regional Ocean Modeling System), a primitive equation, free-surface model described on an orthogonal curvilinear coordinate system in the horizontal, (ξ,η), and a generalized terrain-following coordinate in the vertical. We use data provided from Mason (2009), where ROMS is applied over the Canary Islands basin with climatological forcing of 1/2 monthly means. The horizontal domain has 332×534 grid points, covering a total of $996\times1602 km^2$, with an horizontal resolution of Δ =3km and 75 vertical s-levels. The domain is rotated clockwise 28.5° to become parallel to the coast line. The different ocean variables can be rotated from (ξ,η) curvilinear grid directions to geographic east and north, (λ,θ), following a rotation (Evans, 2001):

$$\begin{aligned} u_\lambda &= u_\xi cos(\Theta) - u_\eta sin(\Theta) \\ u_\theta &= u_\eta cos(\Theta) + u_\xi sin(\Theta), \end{aligned} \tag{4.2}$$

where (u_ξ,u_η) represent the horizontal components of the velocity field pointing in the direction of the curvilinear grid (ξ,η), and (u_λ,u_θ) the velocity field pointing in the direction of longitude and latitude. Θ is the counterclockwise angle between the ξ-axis and true east at grid points. Notice that grid coordinates are extracted from Easy-Grid (Equal-Area Scalable Earth Grid), whose method generates an horizontal grid lattice superimposing an

equal-area map. We apply the formalism by using the curvilinear coordinate (ξ, η) given by the model and vertical locations are represented always in meters depth by performing a bilinear interpolation from model data. Bilinear interpolation is performed according to the formulation in Delandmeter and van Sebille (2019), which provides an interpolation scheme suitable for curvilinear C-grids, and trajectories are integrated using a fourth order Runge-Kutta method with integration time of 20 seconds. We uniformly distribute particles at the releasing layer with distances between them of $\delta = 0.5\Delta$, which equals to 1.5km. This initial setup results in a total of N=176423 released particles. The releasing layer is fixed at depth $z_0 = 100$m and we analyze transport by varying the depth of the collecting layer, $z = 300, 600, 1200$m.

Finally, we establish a range to be studied for the settling velocity taking into account the properties of the external flow, and assuming a strictly negative particle velocity, and its restriction to values within the theoretical validity of Eq. (4.1). The application of the two-layer map is restricted to particles with a preferential motion, in this case pointing in the vertical direction. We analyze transport of particles that sink downwards from the ocean surface due to their physical properties and gravity, ultimately reflected in the settling velocity. The upper limit of settling velocities is established looking at the distribution of the vertical fluid velocity, which allows the identification of a significant range of sinking particle's velocities when comparing the settling velocity to that of the fluid. In Fig. 4.2 we show the probability density function of the vertical fluid velocity values, w, along the full three-dimensional domain. Assuming that the velocity field distributes according to a normal distribution, the percentil P_{95} value is located around w=20m/day, which corresponds to the upper positive limit (i.e, upwards) below which the 95% of vertical fluid velocities are located. Furthermore, an empirical estimation of the percentage of values falling below $w = 20$m/day agrees with this Gaussian approximation percentage. The condition of $v_s \leq$ 20m/day guarantees a significant proportion of particles to travel downwards, i.e., that at least 95% of the released particles will cross the bottom layer. With this analysis, and taking into account the theoretical range in Monroy et al. (2017) for which the equation of motion is valid, we conclude that we should restrict to settling velocities limited to the interval of 20m/day - 1000m/day in the downwards direction. We explore the dynamics of oceanic sinking particles for three different setups: $v_s = 20, 60, 100$m/day.

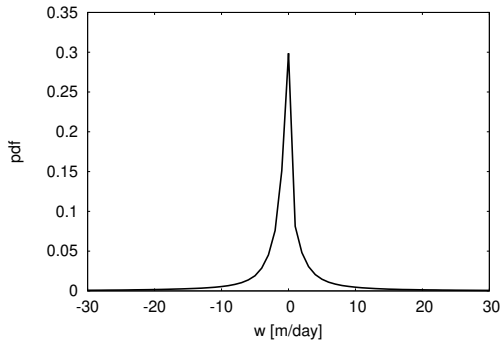

Fig. 4.2 Probability density function of the vertical fluid velocity, w, along the three-dimensional fluid domain.

4.4 Results

4.4.1 Seasonality of FDLE

We first analyze the seasonality of the FDLE for $v_s = 20$m/day, which is expected to show more seasonality if compared to faster sinking particles. The releasing layer is fixed at $z_0 = 100$m and the bottom layer at $z = 600$m depth. Monthly and spatial averages for 4 years of the FDLE are computed starting from January in Fig. 4.3. The temporal evolution of the mean FDLE in the Canary Islands basin shows one-year seasonal cycle with maximum values in February. This result is in agreement with the seasonal predictability of large-scale flow patterns (Chen et al., 2006, Vannitsem, 2017), with lower predictability of oceanic patterns in late winter. Seasonal instabilities in surface waters are mainly driven by trade-winds that are ultimately reflected on the spreading of particles. Consequently, the FDLE appears to be inversely correlated to sea surface temperature (see Fig. 4.3 (b)). As expected, higher values of horizontal dispersion occur at minimum water temperatures, coupled to the desestabilization of the water column. Conversely, lower values of the FDLE in early autumn are in concordance with the vertical stabilization of the column in warm conditions. Seasonality of FDLE fields is reflected in the full range of sinking particles. However, while FDLE values show lower values for faster particles, a qualitative comparison of the FDLE when varying the settling velocity of particles suggests a more flattened seasonality for increasing sinking velocities. This is consistent with the fact that faster particles are less affected by lateral transport, and fall almost vertically along the water column.

In Figure 4.4 we show the FDLE field at initial particle trajectories in the releasing layer starting at each of the four seasons. Although mean values of the FDLE show seasonality, the range of values remains constant in all time periods. Indeed, maximum values are of the

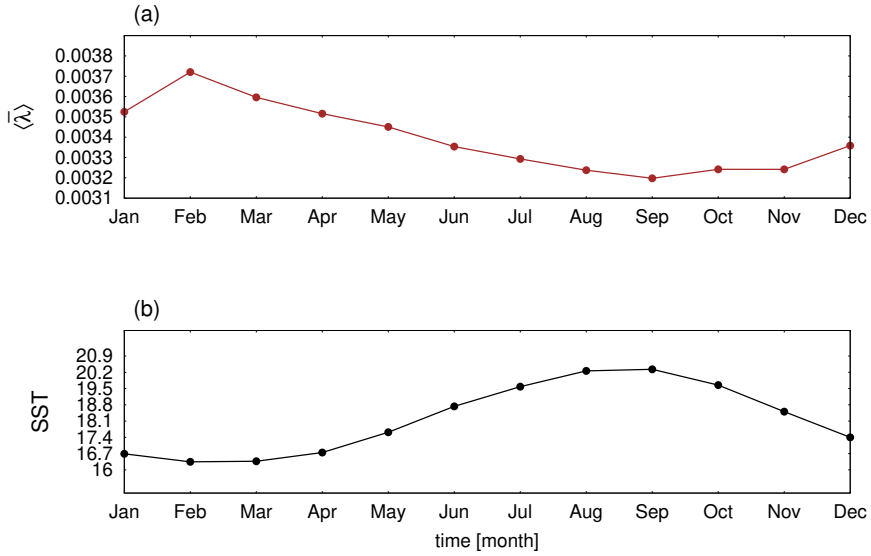

Fig. 4.3 (a) Monthly and spatial average of FDLE values over 4 years starting from January. The settling velocity is fixed at v_s=20m/day and the releasing and bottom layer are located at $z_0 = 100$m and $z = 600$m depth, respectively. (b) Mean Sea Surface Temperature.

order of 0.012 meters^{-1} in all seasons.

In relation with previous observations, we observe eddies appearing in all seasons, with higher values of the seasonal FDLEs in concordance with the highest mesoscale activity taking place in late winter and early spring (Valdés and Déniz-González, 2015, Arístegui et al., 2001). In particular, eddies appear as filamentary structures with maximum values of the FDLE in the boundaries and very low values in the core of eddies, suggesting that particles tend to concentrate inside eddies while boundaries act as a barrier that prevents particles to cross it. In summer and autumn we observe the predominance of big vortices around the Canary islands, which agrees with a predominance of island-generated eddies and stabilization of the water column in summer. On the other hand, in winter there is an increase of mesoscale structures and the big vortices predominate along the coast line, in accordance with a dominant generation of eddies at the coast in this season and the destabilization of water column. In the following, we focus on structures in spring, when the transport of cold and rich upwelled waters into the open ocean takes place through long filamentary structures and eddies.

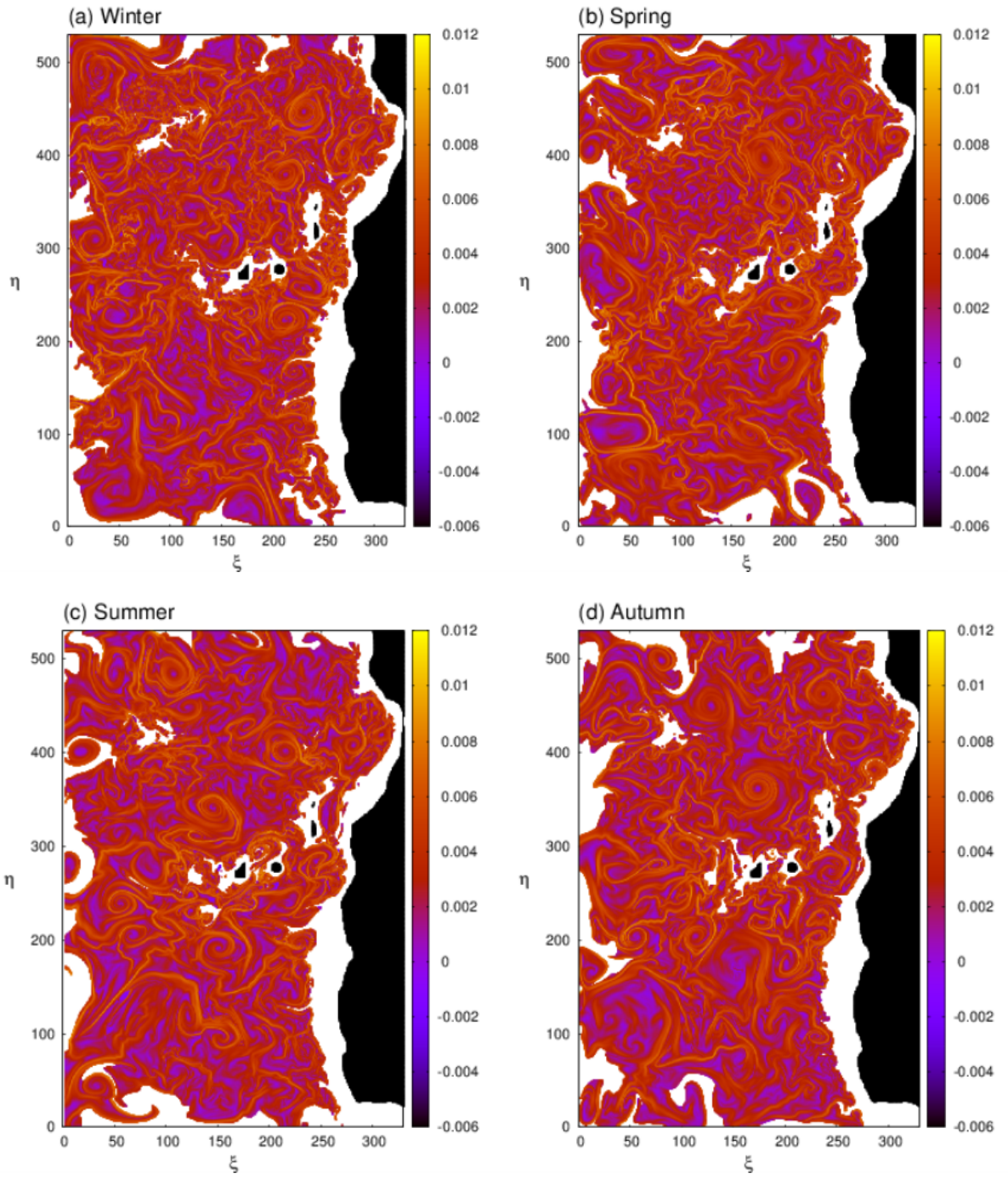

Fig. 4.4 FDLE fields displayed at the initial releasing layer $z_0 = 100$, with $z = 600$ the bottom layer, the settling velocity fixed at $v_s = 20$m/day, and starting at seasons (a) winter (December), (b) spring (March), (c) summer (Juny) and (d) autumn (September).

4.4.2 FDLE Fields

FDLE fields do not inform about the instantaneous location of structures, but rather about the horizontal transport structures at the initial or final locations of particles that sink from the ocean surface and reach a given depth. Maximum values of the FDLE field organize into filamentary structures, where particles experience maximal stretching and do not cross them while sinking. In this section we analyze FDLE fields and how they vary for different collecting layers and increasing settling velocities. In figures 4.5, 4.6 and 4.7 we show the FDLE fields for settling velocities $v_s = 20, 60, 100$, and collecting layers $z = 300, 600, 1200$ for each case study. Simulations are performed in spring, starting in March, and initial location of particles is set to $z_0 = 100$.

The typical length scale for vortices is approximately 50Δ=150km. Negative values of the FDLE predominate at the eddy cores, whereas eddy boundaries have positive and maximal values. As observed in figures, although there are a few big vortices along the Canary eddy corridor, there is not a predominance of island-generated eddies, and mesoscale structures are abundant in all the domain. One interesting observation is the filamentary structure that spans in west direction along the islands line, which may be associated to the transport of cold and rich waters to the deep ocean taking place in late winter and early spring.

Typical values of the FDLE decrease for increasing distances between layers in all setups. This result suggests a convergence of the FDLE values for increasing vertical distances, similarly to the evolution of the FTLE when increasing integration times. However, the projection effect may cancel any global property of the dynamical evolution of the falling surfaces. This is the case, for example, in the modified version of the ABC flow in Chapter 3, for which the projection P is more determinant to F if compared to the effect of stretching factors S. We hypothesize, however, that there are global trends associated to the changes of FDLE fields when increasing vertical distances between layers that are inherent to incompressible and hyperbolic flows with a preferential direction of motion. This hypothesis is supported from the fact that, in such flows, while stretching factors of falling surfaces increase for increasing vertical distances (or integration times), the projection factor has similar global effects without dependency on the collecting layer depth where it applies. This argument is also in concordance with the appearance of more filamentary structures for increasing the bottom depth. Finally, a qualitative comparison between Figures 4.5-4.7 indicates that FDLE values also decrease for faster particles. It agrees with the fact that faster particles are less influenced by the external flow, resulting in a more flattened field and broader structures. These results show that the global structure of transport governed by the dynamics is robust

to changes in both parameters, the settling velocity and the vertical distance between layers.

In Fig. 4.8 we analyze quantitatively the evolution of stretching rates, $\bar{\Lambda}$, and FDLEs, $\bar{\lambda}$, averaged over all particle trajectories as a function of distance between both layers, $z - z_0$. As discussed previously, stretching rates increase for increasing vertical distances, but with a decrease in FDLE values. While FTLEs usually converge asymptotically to a given value for increasing integration times, the evolution of the FDLE for increasing sinking distances may have fluctuations due to the effect of local projections onto the collecting layer. In particular, we observe in Fig. 4.8(b) that the FDLE seems to approach some positive value, but the log-log picture illustrated in the inset shows that such convergence does not take place in the parameter space of study. Although a deeper analysis may be required, the results suggest that a steady state would be reached for deeper collecting layers and slower particles to those limited in our study. On one side, infinitesimal lines advected by a three-dimensional incompressible flow are expected to grow at a rate given by Lyapunov exponents. On the other hand, because the vertical component of the external velocity flow follows a normal distribution with zero mean, the vertical particle velocity fulfills $\langle v_z \rangle = v_s$ and arrival times of particle trajectories follow a linear relationship with vertical spatial distances, which is approximately $\langle t_z \rangle = |z - z_0|/v_s$. Consequently, mean stretching rates of the three-dimensional falling surfaces, Λ_{max}, computed at t_z when they reach the collecting layer, are also expected to show an increase for increasing vertical distances, $z - z_0$. A first conclusion is that both dependencies, in t_z and z, of field properties (averages over all particle trajectories) show similar dispersion laws. Furthermore, we have verified that this is indeed the case for the evolution of the three-dimensional stretching rates of falling surfaces. A second conclusion is that, as previously suggested, because the projected stretching rates, $\bar{\Lambda}$, also show increasing values with depth, the projection effect does not significantly affect the vertical (or time) evolutionary trends reflected on the large-scale properties of particle dispersion taking place between layers, and only may add small fluctuations.

FDLE identifies separatrices of maximum horizontal dispersion of particles when reaching the bottom layer. To visualize the location of such structures at the bottom layer, FDLE values can be displayed at final particle's position given by the two-layer map. In Figure 4.9 we show FDLE values at each initial and final particle locations of the two-layer map. Since the particle dynamics is time-dependent, arrival times are specific to each particle trajectory. Consequently, the FDLE map displayed both at the releasing and collecting layers has not to be interpreted as the existence of instantaneous structures, but rather about the properties of transport on the horizontal layers.

4.4.3 Transport structure from Bipartite Networks

In this section we first check the relationship between the geometric and network characterizations, as pointed out in Chapter 3. We perform the simulations starting in March. The layer domain is partitioned into boxes of size $6\Delta = 18km$, giving a total number of 4895 regular boxes in each layer. A number of $N = 144$ particles are released homogeneously from each box in the upper layer. Furthermore, we assure a statistical significance in the network measures by excluding in the simulations such releasing boxes for which more than 5% of releasing particles scape before reaching the collecting layer.

Connection between Bipartite Networks and Lyapunov Exponents

The out degree is displayed in Fig. 4.10 at releasing boxes for $z_0 = 100$ and collecting layers $z = 300, 600, 1200$. The simulation is performed for the slowest settling velocity, $v_s = 20m/day$, as it better captures the filamentary structure of transport if compared to faster particles. As expected, typical values increase for increasing depth, indicating larger horizontal dispersion of fluid boxes when reaching the second layer. Furthermore, a qualitative comparison with Fig. 4.5 suggests a close relationship between the out degree and stretching factors of the two-layer map. However, the filamentary structure loses some degree of resolution when performing the coarse-graining. This result is aligned from the fact that mesoscale structures are not well captured by the most robust large-scale sructures of transport. In Fig. 4.11 we check the validity of Eqs. (3.26, 3.27) described in Chapter 3. As expected, the relation of out-degree and network entropy correlate well with the geometric interpretation of the bipartite mapping. On the other hand, we also observe some deviations from equality with a predominance of higher values of network measures when compared to stretching factors (logarithm of stretching factors for network entropies). As previously discussed, this inequality is mostly due to the fact that values of the second singular value $\bar{\Lambda}_2$ close to one break the analogy between footprints and thin filaments, and the projection results into broad strips.

Horizontal communities

In this section we identify coherent regions associated to each layer by applying the *Infomap* algorithm and using the two one-mode matrices given in Eq. (3.28) as transition probabilities of transport. This community detection method shows a partition of each layer into regions with low interconnectivity and high intraconnectivity given the two one-mode projection matrices. This means that there is a rather different set of final positions for particles released

from different communities.

We first identify communities for layers located at $z_0 = 100$ and $z = 600$. The result of this partition is illustrated in Fig. 4.12 for increasing settling velocities v_s, and communities are differentiated with different colors. In general, coherence ratios are high, with values close to unity, which indicates a good community partition into almost isolated regions. On the other hand, mixing values are rather moderate, which is expected from the fact that values close to one correspond to an accumulation of all particles in highly dense regions, a situation which is unrealistic for oceanic flows. The Canary basin is partitioned into two main communities along the offshore line crossing the Canary islands for both layers and setups. This result shows that the presence of the Canary islands has a strong influence on dynamics and generate a zonal barrier, although the absence of more partitions may be also strongly biased by the presence of the islands. We observe increasing coherence and a decreasing of mixing ratios for faster particles, reflected from the fact that faster particles sink more vertically and experience lower lateral advection.

A two-level *Infomap* partition of communities is performed in Fig. 4.13, i.e, the community structure occurring inside first-level communities of Fig. 4.12. In this case, coherence values are lower and mixing increases for all communities, but both values remain high enough to guarantee a good community partition. As for the first-level community description, coherence values increase for faster particles while mixing decreases. On the other hand, a qualitative comparison between the different setups (given by panels (a)-(c)) shows a lack of community robustness when varying the settling velocity and a slightly increasing number of communities for faster particles. Finally, all communities have an elongated shape in offshore direction. We argue that horizontal dispersion of particles may predominate in offshore direction, causing the lateral advection of particles and the transport of coastline particles to deep waters away from the coast, as previously observed in some studies (Pelegrí et al., 2005, Sangrà et al., 2009, Fischer et al., 2020).

The community structure is also modulated by the depth of the collecting layer. We show in Fig. 4.14 some quality parameters of the two-level community structure for varying collecting depths. Releasing layer is fixed at $z_0 = 100$, and $v_s = 20m/day$ for all setups. We conclude from Fig. 4.14(a) that the mean area of communities increases for larger distances between layers, $|z - z_0|$, according to a decrease in the number of communities. Note that we lose statistical significance for highest vertical distances, for which we observe a deviation from the trend. Finally, Figs. 4.14(b),(c) show a lose of coherence but a gain in mixing for increasing depths.

4.5 Conclusions

We have analyzed transport properties of sinking particles travelling between horizontal layers in the Canary islands basin. In particular, we have applied the two-layer map and transport measures defined in Chapter 3 to idealized sinking particles, whose dynamics are governed by the external fluid flow and a settling velocity. Typical vertical velocities in the external flow have limited the range for the possible settling velocities, from $v_s = 20m/day$ to $v_s = 200m/day$.

The first approach uses a geometric interpretation of transport, for which the Finite-Depth Laypunov Exponent is applied. FDLE fields show one-year seasonality with higher dispersion rates taking place in winter, in accordance with seasonal instabilities of the flow along the water column and observational results related to the spreading and lateral export of particles around the Canary basin. FDLE fields organize the layer domains into regions of different dynamical behavior. Maximum values define thin filaments, approximating the most horizontal repelling lines of sinking particles travelling between layers, and show vortices and horizontal fronts taking place along the Canary basin.

Focusing on March season, we observe a decreasing FDLE values for increasing final depths. The FDLE results fom the combination of two well different processes: The deformation of fluid patches as they are advected by the three-dimensional flow and their projection onto the bottom layer. The results indicate that the projection effect does not cancel the dispersion laws of large-scale properties when varying the collecting depth or settling velocities. In particular, there is an increase of stretching factos $\bar{\Lambda}$ and the appearance of more filamental structures for increasing the collecting depth and slower particles.

The network approach analyzes transport properties from a statistical point of view using a coarse-graining of the domain and applying concepts of network theory. The heuristic relationship between FDLEs and network measures is checked in this realistic flow. The relations show a good correlation with a slight deviation due to stretching factors associated to the second eigendirection close to one.

Finally, coherent regions are characterized independently at each layer. The community detection algorithm *Infomap* is applied over the two one-mode projection matrices to obtain a domain partition into almost isolated regions with high internal mixing. The global structure of transport gives a partition of the domain into two main communities along the offshore line parallel to the Canary islands. However, a two-level partition of communities shows that the community structure is modulated by settling velocities and bottom depths. Interestingly, all

communities present an elongated shape in offshore direction, which suggests a predominance of lateral transport of particles in offshore direction, from the surface close to the coast to deep waters in the interior of the ocean.

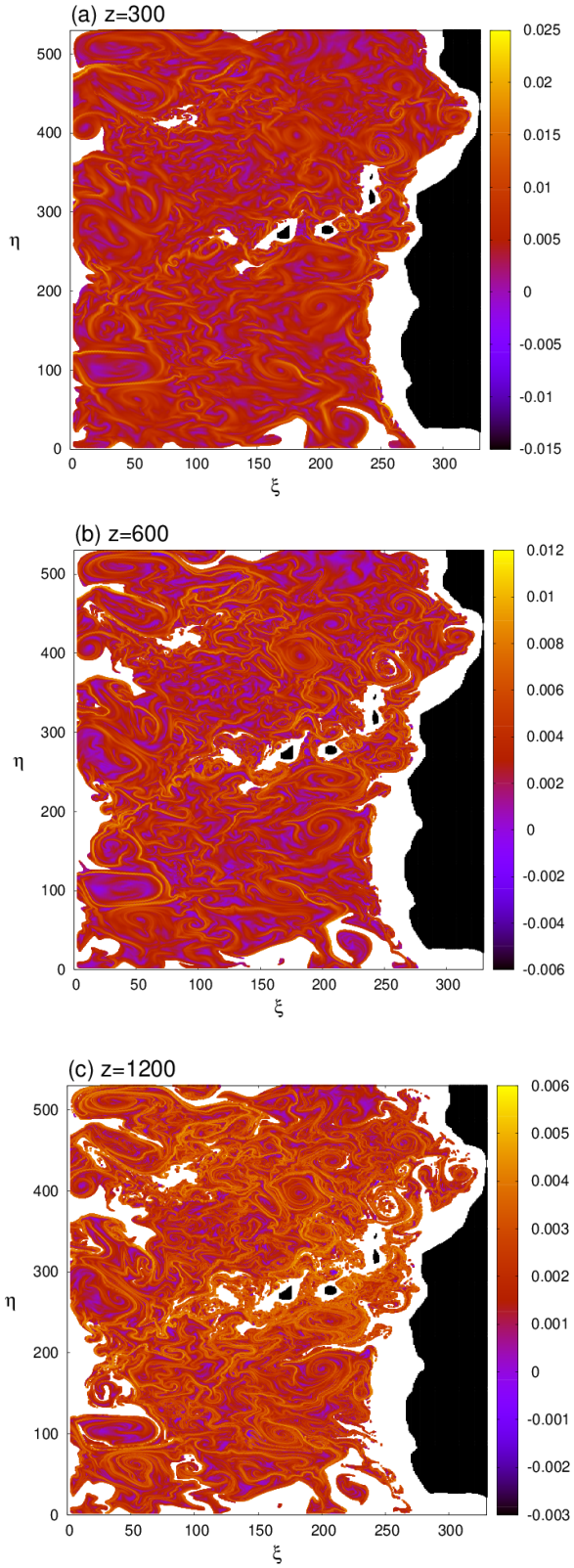

Fig. 4.5 FDLE field for 20m/day from $z_0 = 100m$ and final layer at (a) $z = 300$, (b) $z = 600$, and (c) $z = 1200$, starting in March.

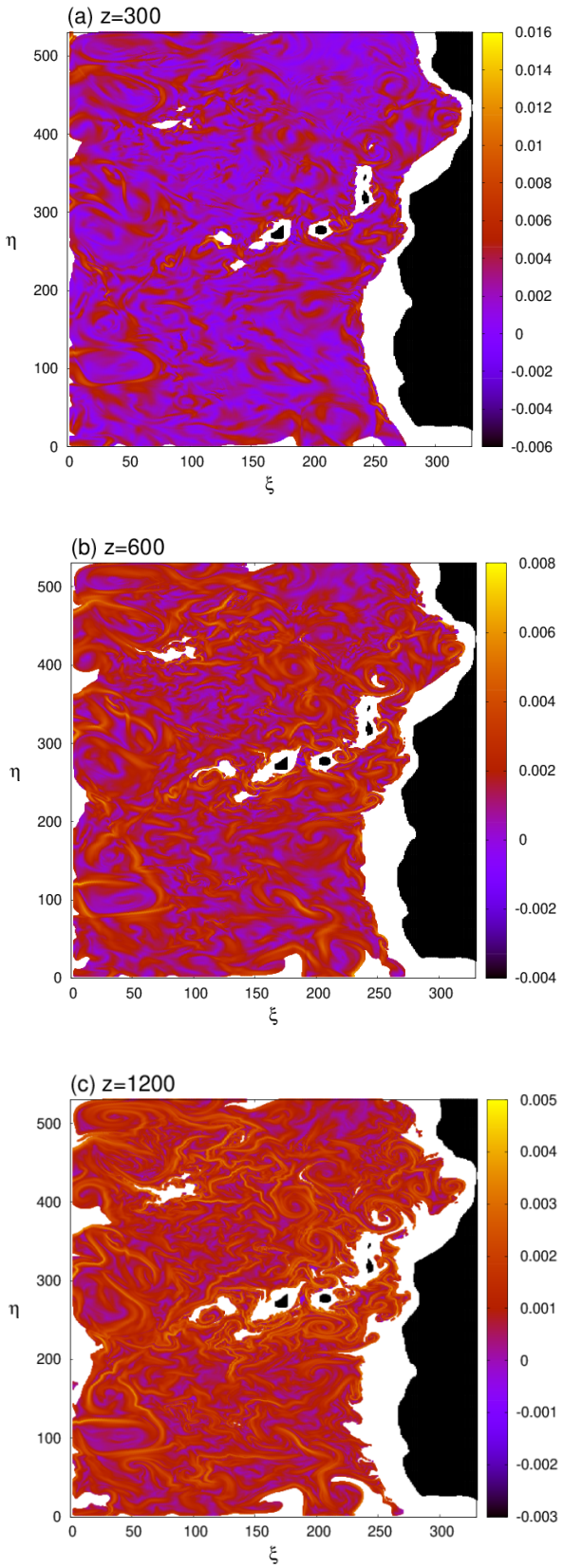

Fig. 4.6 FDLE field for 60m/day from $z_0 = 100m$ and final layer at (a) $z = 300$, (b) $z = 600$, and (c) $z = 1200$, starting in March.

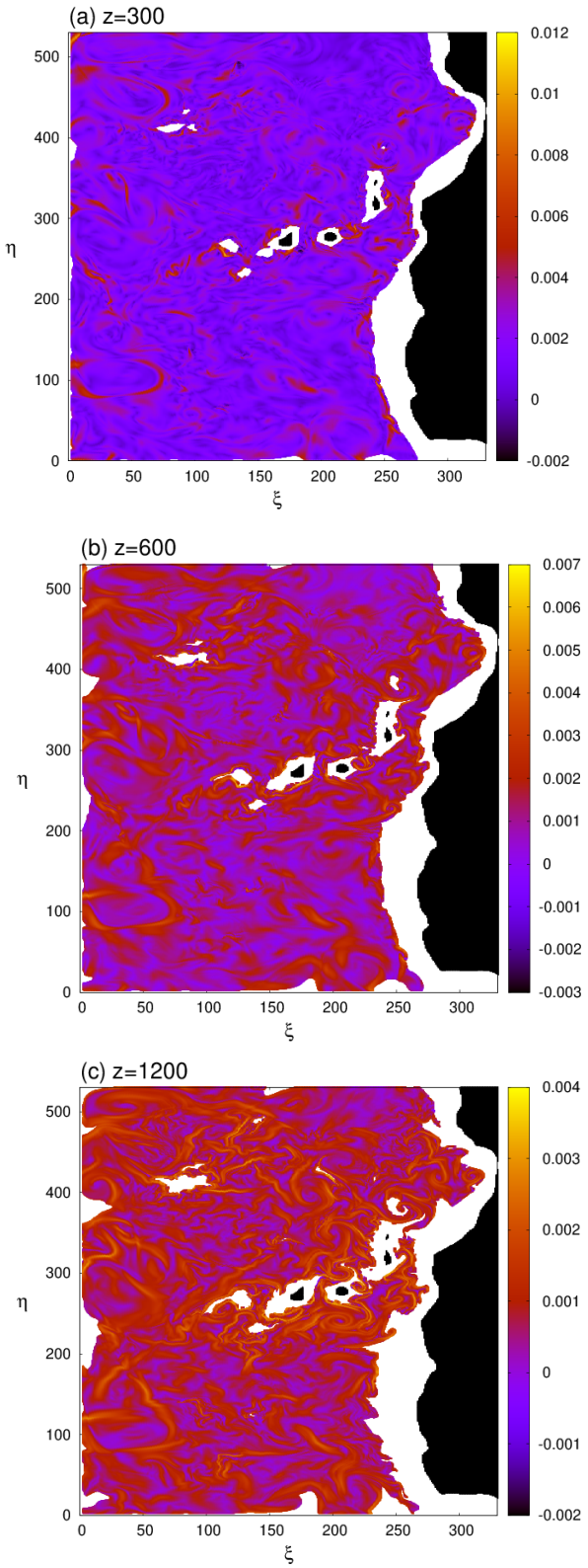

Fig. 4.7 FDLE field for 100m/day from $z_0 = 100m$ and final layer at (a) $z = 300$, (b) $z = 600$, and (c) $z = 1200$, starting in March.

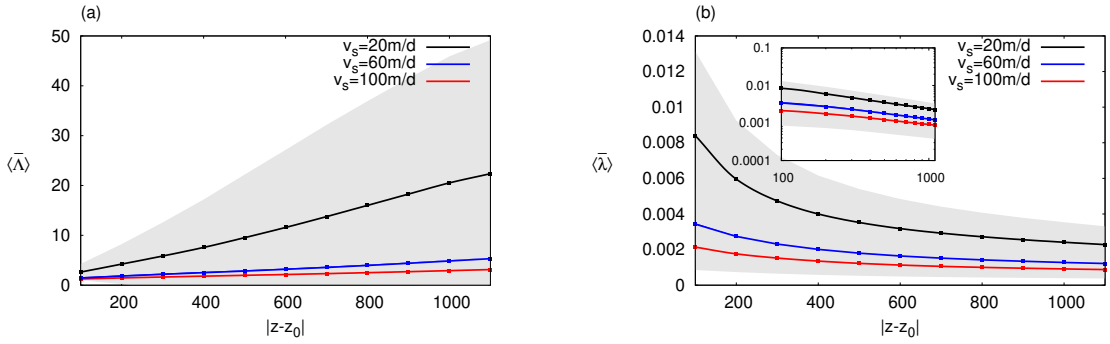

Fig. 4.8 average values of (a) stretching factor and (b) FDLE for increasing vertical distance between layers, for $v_s = 20, 60, 100$, $z_0 = 100$ and $z = 600$. Inset of (b) shows the log-log scale of mean FDLE values.

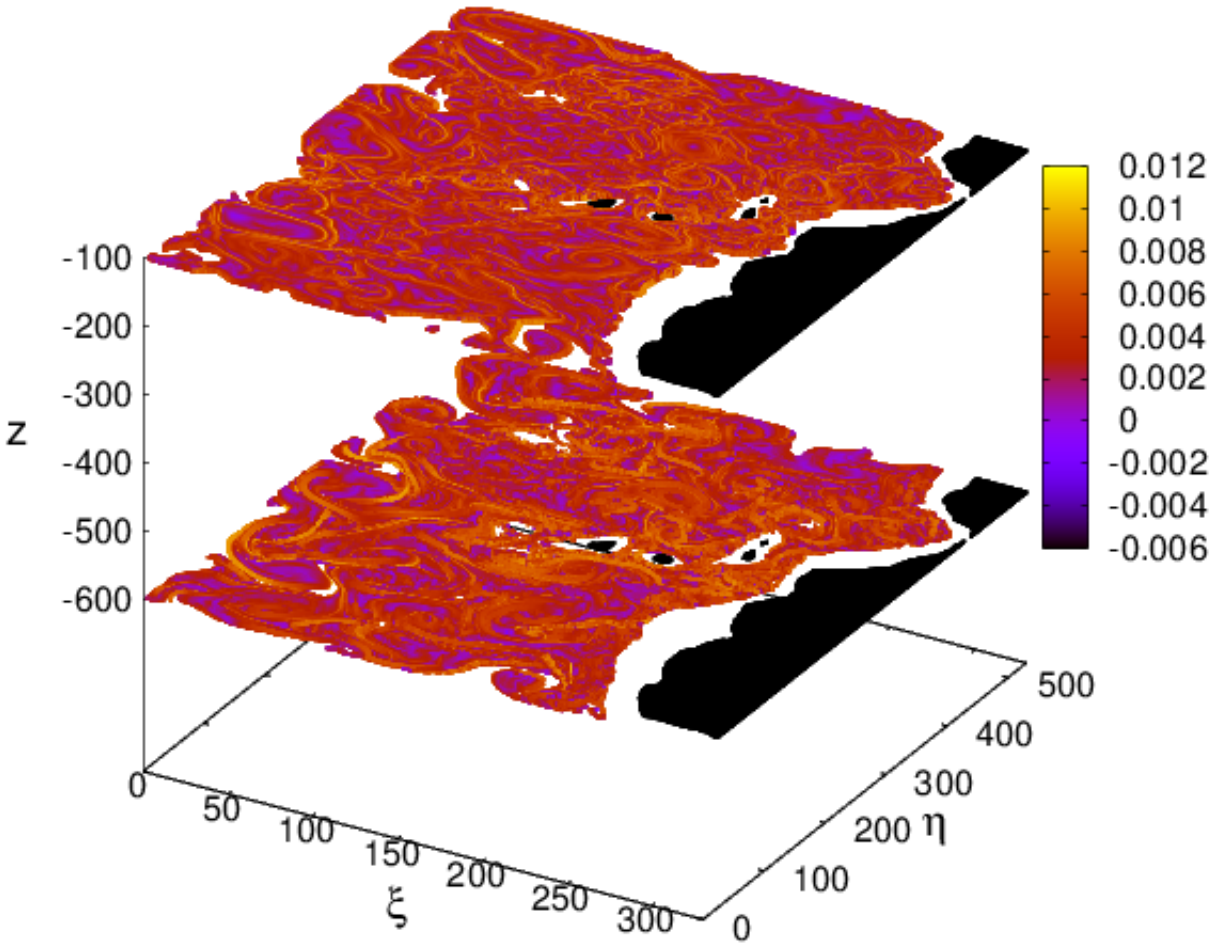

Fig. 4.9 FDLE field showed at initial and final particle locations of the two-layer map. Parameters are fixed at $v_s = 20$m/day, $z_0 = 100$, $z = 600$.

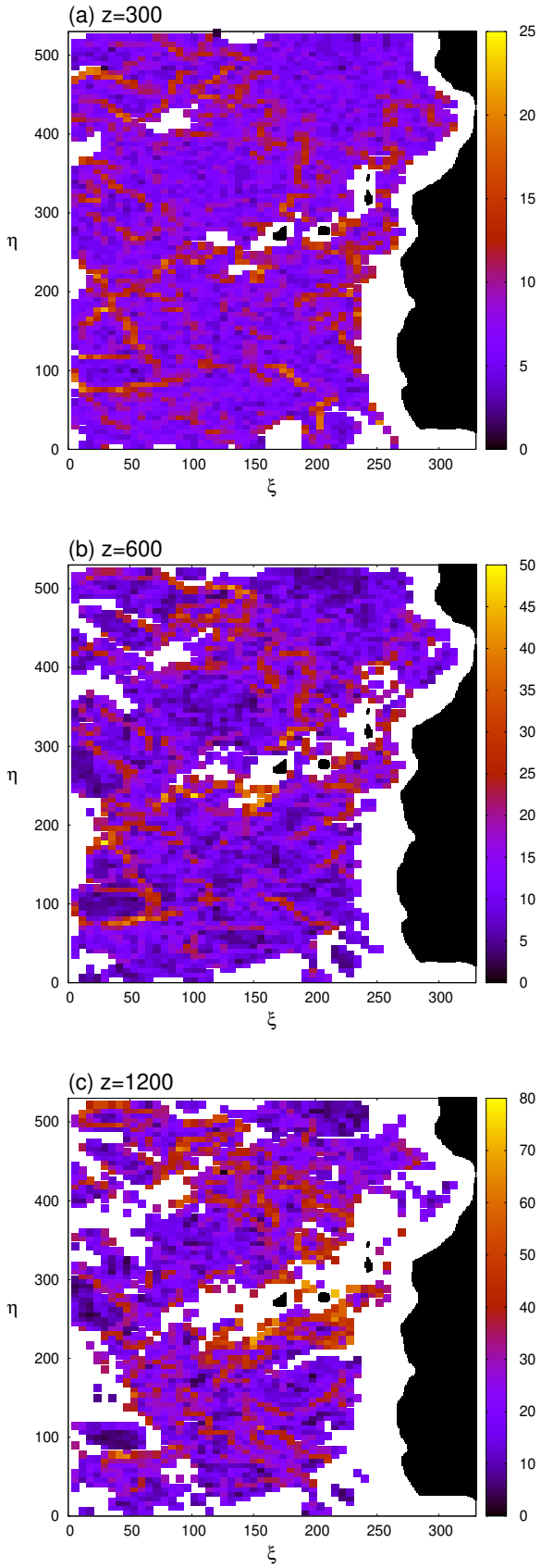

Fig. 4.10 Out-degree in the releasing layer ($z_0 = 100$) for $v_s = 20m/day$. Collecting layers are (a) $z = 300$, (b) $z = 600$ and (c) $z = 1200$.

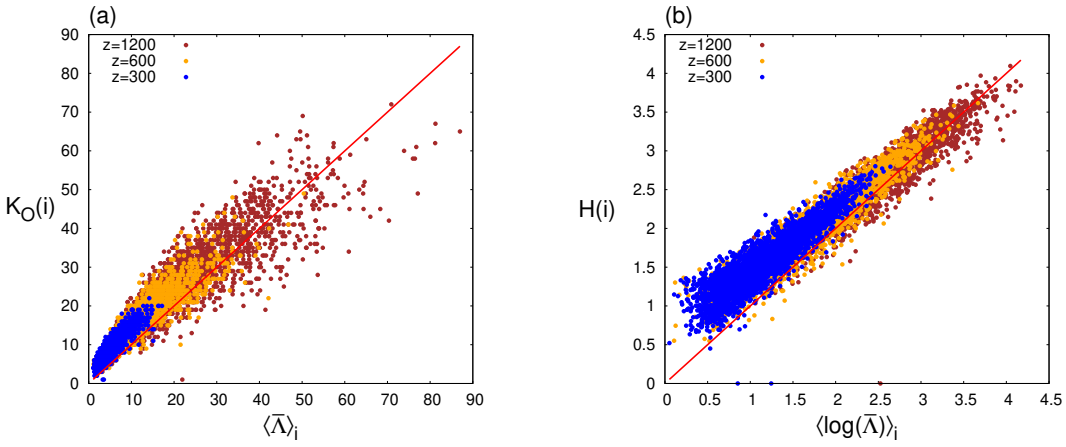

Fig. 4.11 Scatter plots of (a) $K_O(i)$ vs $\langle\bar{\Lambda}\rangle_i$ and (b) $H(i)$ vs $\langle log(\bar{\Lambda})\rangle_i$. The diagonal red line corresponds to equality and dots are colored according to collecting depth layers $z = 300$ (blue), $z = 600$ (yellow) and $z = 1200$ (red). Simulations are performed with $v_s = 20m/day$ and $z_0 = 100$.

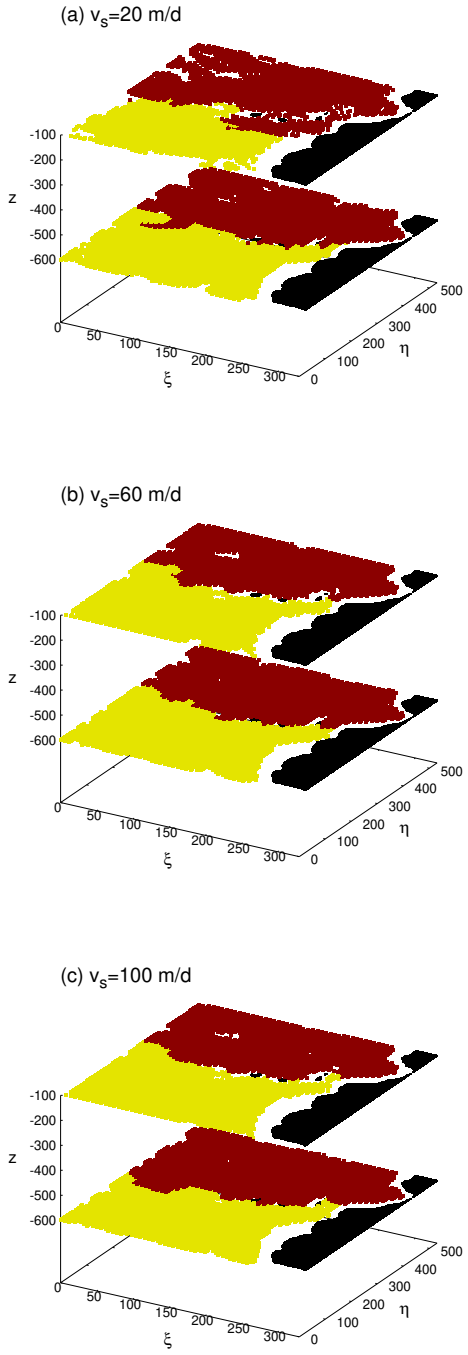

Fig. 4.12 Partition of domain layers into two communities given by *Infomap* algorithm from the two-one mode projections $\mathbf{M}^{Out}$ and $\mathbf{M}^{In}$. Particle dynamics are integrated forwards in time with releasing and collecting layers set at $z_0 = 100$ and $z = 600$, respectively. Settling parameter is fixed at (a) $v_s = 20m/day$, (b) $v_s = 60m/day$ and (c) $v_s = 100m/day$. Colors are assigned randomly to each community. Global coherence and mixing ratios are (a) $\rho^z_{z_0} = 0.987$, $m^z_{z_0} = 0.379$, (b) $\rho^z_{z_0} = 0.994$, $m^z_{z_0} = 0.264$, and (c) $\rho^z_{z_0} = 0.993$, $m^z_{z_0} = 0.236$ for community partition in the releasing layer, and (a) $\rho^z_{z_0} = 0.986$, $m^z_{z_0} = 0.381$, (b) $\rho^z_{z_0} = 0.995$, $m^z_{z_0} = 0.264$, and (c) $\rho^z_{z_0} = 0.995$, $m^z_{z_0} = 0.236$ for community partition in the collecting layer.

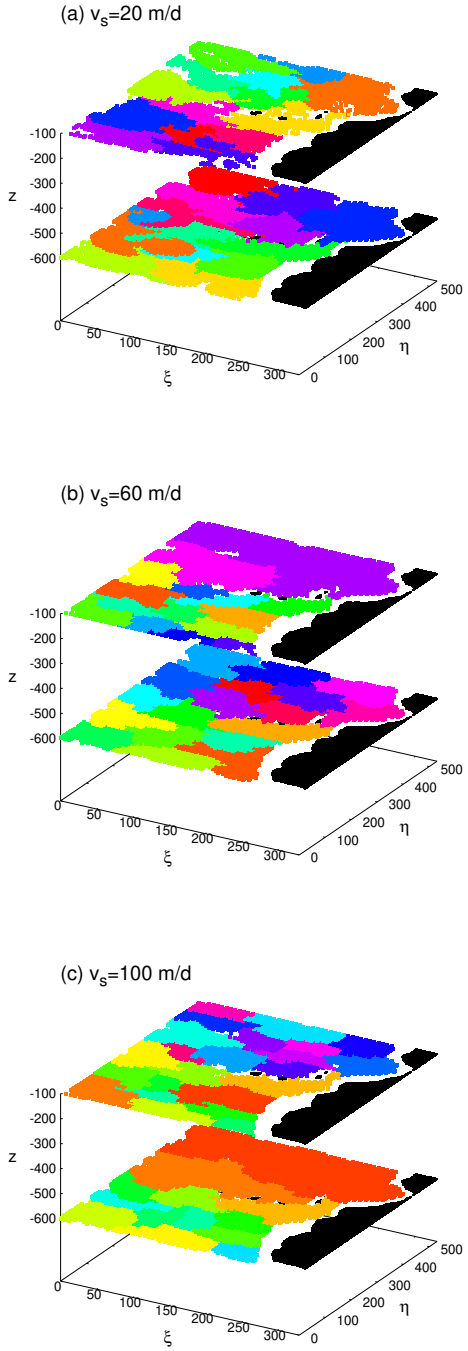

Fig. 4.13 Two-level *Infomap* partition of Fig. 4.12. Global coherence and mixing ratios are (a) $\rho^z_{z_0} = 0.883$, $m^z_{z_0} = 0.494$, (b) $\rho^z_{z_0} = 0.921$, $m^z_{z_0} = 0.334$, and (c) $\rho^z_{z_0} = 0.924$, $m^z_{z_0} = 0.332$ for community partition in the releasing layer, and (a) $\rho^z_{z_0} = 0.881$, $m^z_{z_0} = 0.487$, (b) $\rho^z_{z_0} = 0.928$, $m^z_{z_0} = 0.358$, and (c) $\rho^z_{z_0} = 0.937$, $m^z_{z_0} = 0.291$ for community partition in the collecting layer.

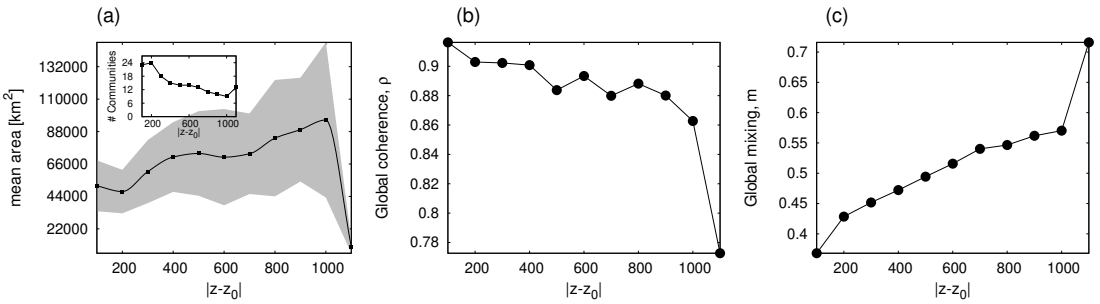

Fig. 4.14 Quality parameters of community partition evaluated at the releasing layer $z_0 = 100$ for increasing distances between layers, $|z - z_0|$. Settling velocity is fixed at $v_s = 20m/day$ and dynamics are integrated forwards in time. Quality parameters: (a) mean area of communities and number of communities (inset), (b) global coherence and (c) global mixing. The shadow in panel (a) corresponds to standard deviation.

Conclusions and Perspectives

We have analyzed the vertical distribution and dispersion properties of micropastics in the Mediterranean sea. We have focused on negatively buoyant rigid microplastics, for which the simplified MRG equation has been tested to be valid. For typical microplastics, the dynamics has been simplified by adding a constant settling term to the external velocity field, as previously used in Monroy et al. (2017) for marine biogenic particles. We have observed a uniform distribution of particles along the water column, except at extremely low settling velocities. The total amount of plastic present in the water column has been estimated to be close to 1% of the floating plastic mass. We have also observed a weak vertical dispersion of particles and the emergence of transient vertical distributions with deviations from Gaussianity, related to anomalous diffusive behaviours dominating the vertical dispersion of particles in some phases. We have argued that regional differences in the sinking process may be the source of these diffusive behaviours.

On the other side, we have developed a formalism to describe transport structures of particles travelling between two layers within a three-dimensional flow. This theoretical framework aims to characterize the transport of particles that travel in a preferential direction, which is of crucial interest for analyzing the motion of sinking particles in the ocean. A two-layer map has been applied to map particle positions initially released at a given layer onto a second one. Two different approaches have been adressed: the geometrical and the probabilistic ones. Within the geometrical, we have characterized the deformation of particle patches. Specifically, the formalism characterizes the transport between layers as the combination of two different processes: the deformation of particle patches as they are advected by the three-dimensional flow and its projection onto the bottom layer. A novel measure, the Finite Depth Lyapunov Exponent, has been defined to quantify the dispersion properties specific to the two-layer map, so it is a new and useful quantity for the study of transport structures of sinking particles. On the other hand, the probabilistic point of view uses tools from network theory and transport properties have been described in terms of network degrees and entropies. Both descriptions of transport have been previously related for two-dimensional flows (Ser-Giacomi et al. (2015a)). In this work, we have tested the

heuristic relation for the two-layer characterization of transport in three-dimensional flows. Also, we have used bipartite networks as a natural description for transport properties between the two layers, for which the out-degree (defined at the releasing layer) and the in-degree (defined at the collecting layer) have a clear physical meaning. The main numerical results have been illustrated in a modified version of the analytical ABC flow model, in which we have added a constant velocity pointing downwards.

Finally, we have applied the characterization to study sinking particles in the Canary Island basin. Horizontal dispersion of sinking particles show one-year seasonality with higher dispersion rates in winter. While final footprints of particles are the result of two combined processes, it has been observed that the projection effect does not dominate the large-scale properties of the flow. We have also compared FDLE values when varying settling velocity of particles and the depth of collecting layers. As a main result, there is a trend of increasing stretching values and the appearance of more filamentary structures for slowest particles and for increasing distances between layers. Within the network approach, we have developed a formalism to identify communities specific to each layer. As a first step, the transport matrix defining connections between both layers has been projected onto each layer, providing a description of similarity between fluid regions located at the same layer in terms of their fate or origin. Next, *Infomap* algorithm has been applied to each one-mode transport matrix and layers have been partitioned into almost isolated regions with high internal mixing. The main result is the partition of the two-layer domain into two main communities along the offshore line parallel to the Canary islands. Furthermore, all communities have an elongated shape offshore, indicating a predominance of lateral export of particles from the coastline.

The developed formalism provides new insights into problems of sinking particles in the ocean by the identification of the vertical skeleton of motion of particles traveling between waters located at different depths. The result is a theoretical characterization that may be useful in all future applications that focus on transport properties of sinking particles, such as the study of sedimentation patterns, barriers to transport, or regions with high mixing properties between regions located at different depths. The formalism may be useful to analyze global patterns of connectivity between superficial and deep waters for sinking particles present in the ocean, compare particle distributions of sinking particles between different regions of the ocean and better understand the global cycles that mantain the sustainability of life. Furthermore, as a novel application, community detection can be practically useful, which is inaccessible without the network characterization. This approach may characterize connectivity patterns between regions located at different depths, and find

almost-isolated regions along its vertical dynamics. This will be relevant for studies of sedimentation, and for the identification of regions of interest, such as highly polluted regions or with high primary activity, with sinking particles remaining in isolated regions along their trajectories in the vertical direction.

Appendix A

Effect of deviations from spherical particle shape on its settling

We complete the analysis of Chapter 2 by quantitatively assessing the impact of deviations from a spherical shape of a falling particle through a correction to the settling velocity v_s. The simplified MRG equation, Eq. (2.3), or its first-order approximations in the Stokes number, Eqs. (2.4) and (B.1), are affected by particle geometry through the drag force and the added mass term; however, accelerations are irrelevant for v_s, so that the added mass term does not appear in its formulation or in the simple approximation of Eq. (2.1). We will compare values of the settling velocity describing nonspherical and spherical particles with the same density, then finally comment on the results' relevance for Eqs. (2.3), (2.4) and (B.1).

Most generally, the settling velocity vector $\mathbf{v}_\mathrm{s}$ can be obtained by balancing the drag force $\mathbf{F}_\mathrm{drag}(\mathbf{v}-\mathbf{u})$ (a function of the difference of the particle and the fluid velocities, $\mathbf{v}$ and $\mathbf{u}$, respectively) with the resultant of gravitational and buoyancy forces:

$$0 = \mathbf{F}_\mathrm{drag}(\mathbf{v}-\mathbf{u}) + V\left(\rho_\mathrm{p}-\rho_\mathrm{f}\right)\mathbf{g} \tag{A.1}$$

with $\mathbf{v}-\mathbf{u}=\mathbf{v}_\mathrm{s}$, where V is the particle's volume, ρ_p and ρ_f are the densities of the particle and the fluid, respectively, and $\mathbf{g}$ is the gravitational acceleration vector. For a spherical particle with radius a, the Stokes drag force reads as

$$\mathbf{F}^{(\mathrm{sph})}_\mathrm{drag}(\mathbf{v}-\mathbf{u}) = -6\pi\mu(\mathbf{v}-\mathbf{u})a, \tag{A.2}$$

where μ is the dynamical viscosity of the fluid. According to Leith (1987), Ganser (1993), an appropriate approximation for small nonspherical particles is

$$\mathbf{F}_{\text{drag}}^{(\text{non})}(\mathbf{v}-\mathbf{u}) = -6\pi\mu(\mathbf{v}-\mathbf{u})\left(\frac{1}{3}a_{\text{n}}+\frac{2}{3}a_{\text{s}}\right), \tag{A.3}$$

where a_{n} is the radius of the sphere with equivalent area projected on the plane perpendicular to the relative velocity $\mathbf{v}-\mathbf{u}$, and a_{s} is the radius of the sphere with equivalent total surface. From either of the last two equations, the settling velocity is obtained by substituting $\mathbf{v}-\mathbf{u}=\mathbf{v}_{\text{s}}$, and solving Eq. (A.1) for $\mathbf{v}_{\text{s}}$. We denote the magnitudes of the settling velocities obtained from Eq. (A.2) and Eq. (A.3) by $v_{\text{s}}^{(\text{sph})}$ and $v_{\text{s}}^{(\text{non})}$, respectively.

To characterize the correction in the settling velocity for a given nonspherical particle (with a given density ρ_{p}) with respect to assuming a spherical shape with a radius a, we will consider

$$q \equiv \frac{v_{\text{s}}^{(\text{non})}}{v_{\text{s}}^{(\text{sph})}} = \frac{3}{4\pi}\frac{V^{(\text{non})}}{a^2\left(\frac{1}{3}a_{\text{n}}+\frac{2}{3}a_{\text{s}}\right)}, \tag{A.4}$$

where $V^{(\text{non})}$ is the real volume of the given particle. In order to evaluate Eq. (A.4), one has to specify the shape and the size of the particle, its orientation with respect to its relative velocity, and also how a is derived from its real size.

Note that it is always possible to define an a for which $q=1$, i.e., for which there is no correction arising from the deviation from a spherical shape. In this sense, any choice of a representing a spherical shape, including ours in the manuscript, describes the settling velocity of certain nonspherical particles, the question is just their shape and size, which will mutually depend on each other for a given a. We will nevertheless proceed by choosing a shape class and defining a along independent considerations, because we intend to link a given a to a single particle size as identified during the processing of field observations.

The shape of rigid microplastic particles is not usually described in the literature, but we can see photographs of some examples in, e.g., Song et al. (2014), Fischer et al. (2015), Bagaev et al. (2017). For an explorative computation, a reasonable choice seems to be a rectangular cuboid with edges A, $B=\hat{B}A<A$ and $C=\hat{C}A<B<A$, where one or both of $\hat{B}$ and $\hat{C}$ are less than 1 but greater than, say, 0.1.

Under this assumption, the particle size will correspond to the longest edge, A, of the cuboid if the size is identified through microscopy as the largest extension ("length"; e.g., Cózar et al., 2015); and it may be related more to the middle edge, B, if one thinks of a sieving technique (e.g., Suaria et al., 2016). The naive choice will be $a=A/2$ and $a=B/2$ in these two cases.

We can substitute either of these choices of a in Eq. (A.4), as well as the appropriate formulae describing the actual cuboid. $V = ABC$ is unique, and so is a_s,

$$a_\mathrm{s} = \left(\frac{AB + AC + BC}{2\pi}\right)^{\frac{1}{2}}. \tag{A.5}$$

However, a_n depends on the particle's orientation with respect to the relative velocity. Implications will be discussed when interpreting the results, and we take here all three directions parallel to edges A, B and C to represent different possibilities. The corresponding expressions for a_n read as

$$a_{\mathrm{n},X} = \left(\frac{ABC}{\pi X}\right)^{\frac{1}{2}} \tag{A.6}$$

for $X = A$, B and C.

After substituting all these expressions in Eq. (A.4), we obtain

$$q_X^{(A/2)} = 9\pi^{-\frac{1}{2}}\hat{B}\hat{C}\left[\left(\frac{\hat{B}\hat{C}}{\hat{X}}\right)^{\frac{1}{2}} + 2^{\frac{1}{2}}\left(\hat{B} + \hat{C} + \hat{B}\hat{C}\right)^{\frac{1}{2}}\right]^{-1}, \tag{A.7}$$

$$q_X^{(B/2)} = \hat{B}^{-2} q_X^{(A/2)}, \tag{A.8}$$

where $X = \hat{X}A$ has been introduced.

We plot $q_A^{(A/2)}$ in Fig. A.1 as a function of $\hat{B}$ and $\hat{C}$ for $\hat{B}, \hat{C} \in [0.1, 1]$ with $\hat{B} > \hat{C}$. Its range extends from 0.07 to 1.5 on this domain, but it drops below 0.1 only for $\hat{C}$ very close to 0.1 and $\hat{B}$ below 0.2; i.e., for extremely thin rod-like particles, which do not appear to be common based on photographs. The range of $q_A^{(B/2)}$ (not shown) on the same domain is between 0.2 and 7, and values above 4 are again restricted to very small $\hat{C}$ and to $\hat{B} < 0.3$. The results are very similar for other choices of X, deviations beyond 20% with respect to $X = A$ are only found for small $\hat{C}$ and do not reach beyond 40% even there.

We have left the question which orientation is relevant open so far. In small-scale isotropic turbulence, which is certainly present in the ocean, nonspherical particles have a preferential alignment with certain characteristics of the flow but undergo rotation (Voth and Soldati, 2017). This is why we have chosen to simply cover three perpendicular orientations in our analysis, and have found that differences that may arise from changes in the orientation are minor in most of the domain describing shapes. The only relevant exception is small $\hat{C}$ with $\hat{B} \approx 1$. This regime may characterize paint flakes (Song et al., 2014, Bagaev et al., 2017), but the relative difference remains below 40% even there.

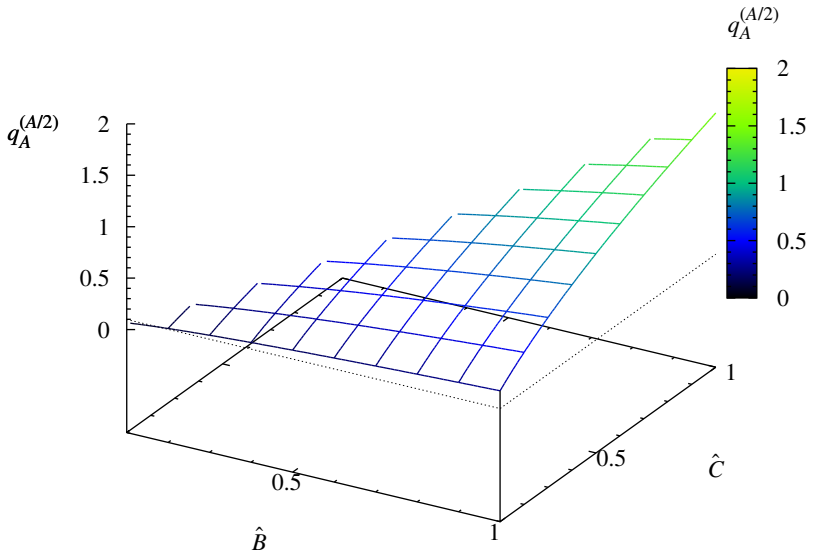

Fig. A.1 $q_A^{(A/2)}$ as a function of $\hat{B}$ and $\hat{C}$ for $\hat{B},\hat{C} \in [0.1,1]$ with $\hat{B} > \hat{C}$. Dotted lines represent $q_A^{(A/2)} = 0.1$.

Even though the real advection of the particles will become more complicated as a result of the ever-changing orientation and may thus be beyond the scope of the MRG equation (cf. the discussion in the main text about the settling velocity of irregular particles), we have found that changing orientation introduces minor variations in the value of the settling velocity. Together with the absence of order-of-magnitude corrections that may arise from a nonspherical shape (but comparing shapes under the assumption of the same particle density), this gives quantitative support for the applicability of a spherical shape in Eq. (2.1) of the main text.

Finally, we briefly comment on the more general Eqs. (2.4) and (B.1), in which effects from nonsphericity arise in the inertial term through added mass. Since corrections in added mass with respect to a sphere are of order 1 for all common shapes (see Kaneko et al., 2014, for an overview), we believe that the finding of App. B about the negligible importance of inertial effects in these equations is not affected by a deviation from sphericity. The Stokes number, which is proportional to the settling velocity and also depends on the coefficient of added mass ($St \sim \tau_p$ with τ_p given by Eq. (2.2)), is estimated to be $10^{-3} - 10^{-2}$ for spherical particles in Sect. 2.4.1, so that it will not increase to 1 due to a nonspherical shape either, hence leaving the approximation (2.4) of Eq. (2.3) valid.

Appendix B

Importance of different physical effects in the dynamics of sinking particles

To complete the analysis of Chapter 2, we present here the detailed numerical analysis of the relevance of a finite time of response (Stokes time, τ_p) of the particle to the fluid forces, the Coriolis force, and scales unresolved by the NEMO velocity field.

We incorporate the first two effects to a single equation,

$$\mathbf{v} = \mathbf{u} + \mathbf{v}_s + \tau_p(\beta - 1)\left(\frac{D\mathbf{u}}{Dt} + 2\boldsymbol{\Omega} \times \mathbf{u}\right) , \tag{B.1}$$

which is identical to Eq. (2.4) except for the addition of the Coriolis force, $2\boldsymbol{\Omega} \times \mathbf{u}$. $\boldsymbol{\Omega}$ is Earth's angular velocity vector. We include the Coriolis force because it can be more important than the other inertial term, given by the fluid acceleration $D\mathbf{u}/Dt$, in large-scale ocean flows $\mathbf{u}$ (Haller and Sapsis, 2008, Monroy et al., 2017).

The effect of unresolved scales will also be estimated by keeping the original NEMO velocity field $\mathbf{u}$ but modifying the equation of motion, Eq. (2.1), by adding a stochastic noise term:

$$\mathbf{v} = \mathbf{u} + \mathbf{v}_s + \mathbf{W} . \tag{B.2}$$

$\mathbf{W}(t) = (\sqrt{2D_h}\xi_x(t), \sqrt{2D_h}\xi_y(t), \sqrt{2D_v}\xi_z(t))$, where $\boldsymbol{\xi}(t)$ is a vector Gaussian white noise process (independent for each particle) of zero mean and with correlations given by $\langle \xi_i(t_1)\xi_j(t_2)\rangle = \delta_{ij}\delta(t_1 - t_2)$, $i, j = x, y, z$. Thus, the horizontal and vertical intensities of this term are given by D_h by D_v, respectively.

The statistical properties are chosen to be similar to the ones expected for oceanic motions below the scales resolved by the numerical model (Monroy et al., 2017, Kaandorp et al., 2020). To do so, we use for D_h Okubo's empirical formulation (Okubo, 1971) that parameterizes the

effective horizontal eddy-diffusion below a spatial scale ℓ as $D_h(\ell) = 2.055 \times 10^{-4} \ell^{1.55} m^2/s$. Taking for ℓ the horizontal resolution of our numerical model (1/12 degrees) we obtain $D_h = 7.25\ m^2/s$. Since the Okubo formula is an empirical fit to surface motions, and effective horizontal diffusivity should be weaker below the thermocline, our results provide an upper bound for the error associated with unresolved scales of fluid motion. For the vertical diffusivity we take $D_v = 10^{-5} m^2/s$.

In order to compare the different equations of motion, we release a large number $N = 78803$ of particles on the whole Mediterranean at 1 m depth on 8 January 2000. We associate a β parameter to each particle by selecting it from a random uniform distribution in the range $\beta \in [0.8, 1)$, and once it is selected it remains fixed at all times for the corresponding particle. High values of β (close to one) correspond to more buoyant plastic particles whereas low values of β correspond to high settling velocities. The corresponding range of velocities is $v_s \in [1.776 \times 10^{-3}, 0)\ m/s$. We integrate the particle trajectories using Eq. (2.1) and also, from the same initial conditions, using the corrected dynamics in Eq. (B.1) or (B.2), all with the same NEMO velocity field $\mathbf{u}$. The horizontal and vertical distances between particles released from the same point but evolved with different equations are compared by calculating the following averages over particles:

$$d_h^I(t) = \frac{1}{N} \sum_{k=1}^{N} |\mathbf{r}_k^0(t) - \mathbf{r}_k^I(t)| \ , \ d_v^I(t) = \frac{1}{N} \sum_{k=1}^{N} |z_k^0(t) - z_k^I(t)| \ . \tag{B.3}$$

$\mathbf{r}_k = (x_k, y_k)$ is the horizontal position of particle k, z_k is its vertical position, and the superindices 0 and I indicate that the particle trajectory has been integrated by using the reference equation, Eq. (2.1) or the one containing inertial corrections, Eq. (B.1). The quantities $d_h^W(t)$ and $d_v^W(t)$, comparing Eq. (2.1) with the dynamics (B.2) modeling small-scale flow effects, are defined analogously.

In Fig. B.1, we display the average distances $d_h^I(t)$ and $d_v^I(t)$ as a function of time, characterizing the corrections by inertial terms to the simple dynamics of Eq. (2.1). Analogously, Fig. B.2 displays the average distances $d_h^W(t)$ and $d_v^W(t)$ as a function of time, characterizing the estimated corrections arising from small scales unresolved by the NEMO velocity field. The effect induced by the inertial terms is very small and clearly negligible. The impact of $\mathbf{W}$, and thus of small unresolved scales is larger.

To evaluate the different effects more quantitatively, we summarize in Table B.1, considering particles separately in different density ranges (given by the ranges in β and associated v_s), the average horizontal and vertical pairwise particle distances, calculated after integrating the different dynamics for 10 *days*. To fully appreciate the importance of these numbers, in the two final columns we compute the horizontal and vertical average of the total distance

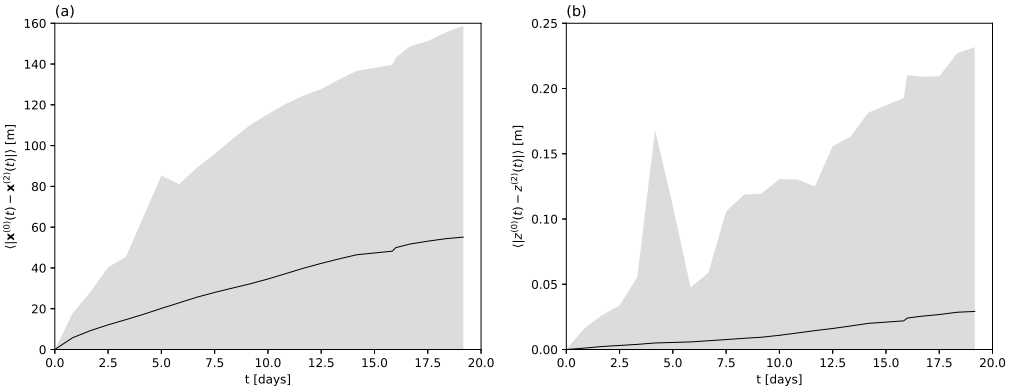

Fig. B.1 Solid line indicates the average horizontal distance d_h^I (a) and the average vertical distance d_v^I (b) of particles released from the same initial location but integrated with equations (2.1) and (B.1) in the NEMO velocity field. Shaded region indicates the range of the distances among the individual pairs of particles.

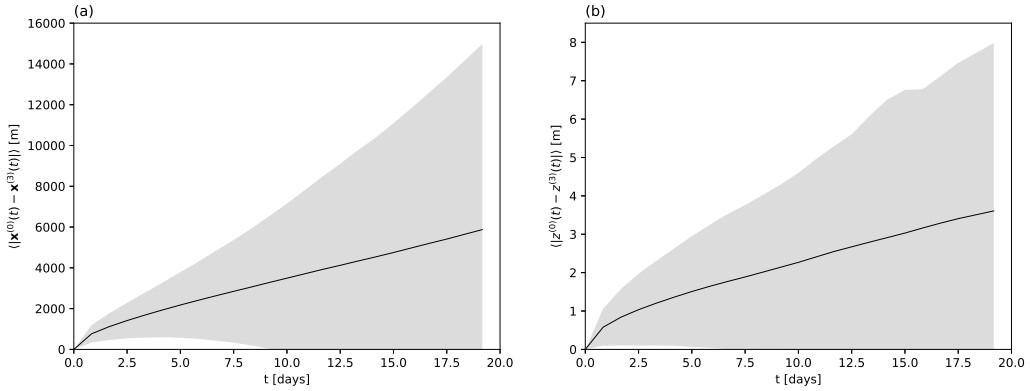

Fig. B.2 Same as Fig. B.1 for the comparison of equations (2.1) and (B.2).

r traveled by the particles (using Eq. (2.1)) during the same interval of time. While the influence of the inertial terms is completely irrelevant both in a relative and an absolute sense for any realistic application, more care has to be taken with regards to the unresolved scales. Although the vertical error associated with the latter remains small, its relative importance hugely increases with decreasing settling velocity. (Indeed, it would tend to infinity for approaching neutral buoyancy.) At the same time, the relative horizontal error is the biggest for the fastest-sinking particles and is well above 10% for them.

We can also observe the time evolution of the d entries of this table in Figs. B.3 and B.4. The overall effect of the unresolved scales is confirmed to be much larger than that of the

β	v_s (10^{-3} m/s)	d_h^I (m)		d_v^I (m)		d_h^W (m)		d_v^W (m)		r_h (m)	r_v (m)
$[0.8, 0.85)$	$[1.78, 1.25)$	60	(0.26%)	0.016	(0.001%)	2675	(11.8%)	2.1	(0.16%)	22601	1291
$[0.85, 0.9)$	$[1.25, 0.79)$	42	(0.14%)	0.010	(0.001%)	2831	(9.7%)	2.0	(0.24%)	29278	870
$[0.9, 0.95)$	$[0.79, 0.37)$	31	(0.08%)	0.009	(0.002%)	3313	(8.0%)	2.1	(0.43%)	41587	493
$[0.95, 1)$	$[0.37, 0)$	16	(0.03%)	0.008	(0.005%)	4668	(8.0%)	2.7	(1.79%)	58320	151

Table B.1 Average horizontal and vertical pairwise particle distances d and single-particle displacements r after an integration time of 10 days. See text. d/r is indicated by percentages in parentheses.

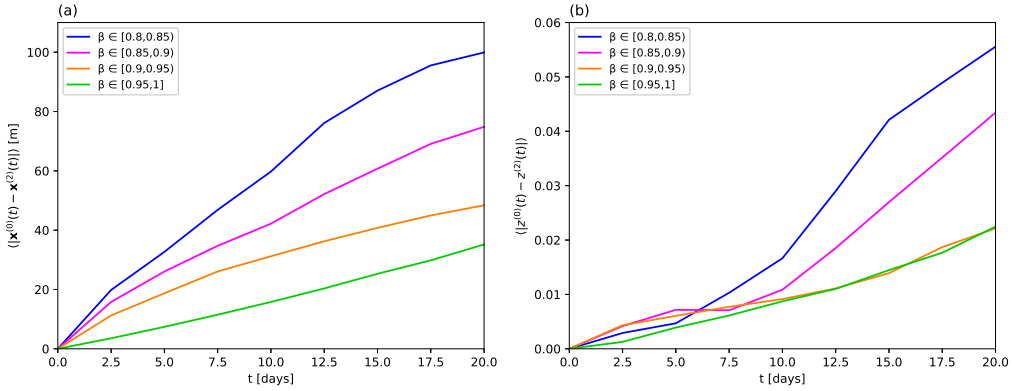

Fig. B.3 Average horizontal distance d_h^I (a) and average vertical distance d_v^I (b) of particles released from the same initial location but integrated with equations (2.1) and (B.1) in the NEMO velocity field. The different lines are obtained from particles from different ranges of densities characterized by the indicated ranges in β.

inertial terms, and the differences between particles with different densities (ranges of β) are less noticeable (except for the smallest densities considered, i.e. $\beta \approx 1$).

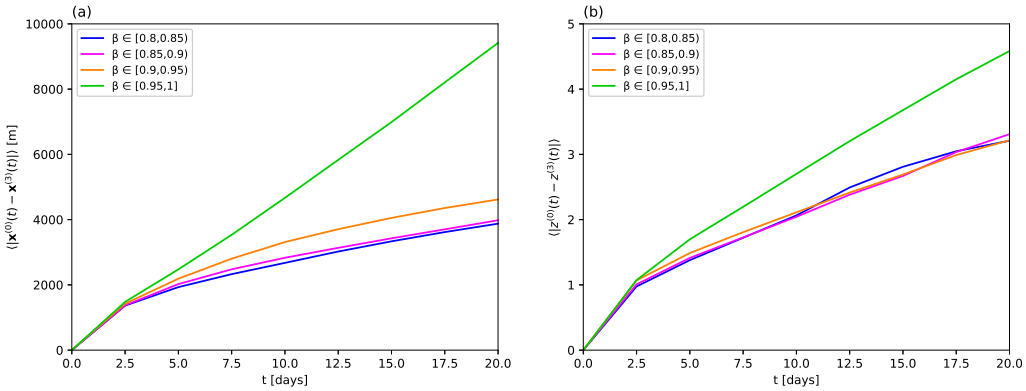

Fig. B.4 Same as Fig. B.3 for the comparison of equations (2.1) and (B.2).

Appendix C

The effect of bathymetry on vertical dispersion

Complementing the analysis of Chapter 2, we investigate here if the finite and spatially varying depth of the basin (the bathymetry) could affect the conclusions in Sect. 2.4.4 about vertical dispersion. The falling particles released from different locations reach the seafloor at different times, and then computing some statistics over these particles involves an increasingly narrow set of particles. Note that the bottom boundary (i.e., the seafloor) extends from the surface (close to the coast) to the deepest point of the basin, it is thus relevant at any time during the simulation. We intend to exclude three different effects arising from the continual removal of particles: (i) distortion of the shape of the distribution close to the boundary, (ii) poor quality of the statistics when many particles have already been lost, (iii) decrease in the geographical area sampled by the particles.

We start with effect (i) by comparing, in Fig. C.1, the variance presented in the main text (Fig. 2.7), computed over all sinking (but not yet sedimented) particles, and that computed over a restricted set of particles. This restricted set contains only those particles at the positions of which the bathymetry Z satisfies $Z > \langle z_i \rangle - 3\sigma_z$, where the average $\langle z_i \rangle$ and the standard deviation σ_z are taken with respect to the original (unrestricted) set of particles. This restriction is adaptive and ensures that the seafloor is sufficiently far for its effect on the particle distribution to be negligible at the positions of all particles kept for the computation. Fig. C.1 shows that the difference in the results between the full set and the restricted one is negligible for all three settling velocities considered, except perhaps for the drop at the very end of the time evolution, after the constant section, in Fig. C.1a. This drop is, however, very short compared to the bulk of the sinking process and thus have minor importance. Furthermore, the distribution of particles so close to the bottom (cf. Fig. 2.9) should anyway be strongly influenced by resuspension and remixing by bottom currents (Kane et al., 2020).

For the rest of the time evolution, we can be confident that a possible distortion of the particle distribution induced by the boundaries has no impact on the variance curves. Such distortion may be present, but the number of particles close to the seafloor is very small at any given time instant (see the small difference between the numbers N of particles considered for the two kinds of computation in Fig. C.1) so that they have a negligible contribution on the originally computed variance. This is a result of the relatively weak dispersion; artifacts might be found for broader distributions, possibly including a hypothetical continuation of the v6 simulation. The time evolution of N in Fig. C.1 also assures us that poor-quality statistics, effect (ii), does not arise until the final drop discussed in the previous paragraph. Except for that very final section, the variance is estimated from a sufficiently large number of particles to keep the relative error of the sample variance (with respect to the population variance) very low. This is so because, under standard assumptions, the ratio between the sample and the population variance should be close to a chi-square random variable with $N-1$ degrees of freedom, divided by $N-1$ (Douillet, 2009).

The time evolution of N also suggests that effect (iii) is avoided as well: in Fig. C.1, there is no sudden drop in the number of particles during the simulations that could result in the changes in the slope of the curves of variance versus time. To further support this conclusion, we compute the time evolution of the variance over the particles initialized in a subregion of the whole Mediterranean, see in Fig. 2.8. In particular, we choose the box of longitudes $[5, 6.9]$ degrees, and latitudes $[37.5, 42]$ degrees, corresponding to the Sea of Sardinia, where the bathymetry is deep enough to prevent particles from reaching the seafloor (except for the very last few time steps of the v153 configuration), so that the horizontal area sampled by the particles approximately remains constant (remember that horizontal displacements are small compared to geographical features).

According to Fig. C.2, the character of the dispersion in the Sea of Sardinia is nearly identical to that in the whole Mediterranean, except after the crossover from normal diffusive to ballistic dispersion in the v153 case (Fig. C.2a). The smaller variance in the velocity should naturally lead to a later crossover to the long-time behavior in the Sea of Sardinia (see Section 2.4.4), it is nevertheless doubtful that the crossover should fall outside the simulation time. As the crossover is not observed, one might speculate that horizontal mixing might just get strong enough to suppress ballistic dispersion, similarly to the v68 case (see the discussion of Fig. 2.7), for which the time evolution of the variance is very similar in the Sea of Sardinia and the whole Mediterranean (Fig. C.2b). Fig. 2.8 suggests that the characteristic patch size is smaller in the western basin of the Mediterranean, including the Sea of Sardinia, than in the (considerably larger) eastern one, which makes inter-patch mixing easier. We conclude that the only substantial difference between the dispersion in the Sea of Sardinia and the whole

Mediterranean may originate from the smaller extension and some special characteristics of the former, and the decrease in the area sampled in the whole-Mediterranean simulation presumably has not effect on the results.

Based on these analyses, we believe that the findings of Section 2.4.4 are unaffected by the boundary and thus have general relevance for oceanic dispersion.

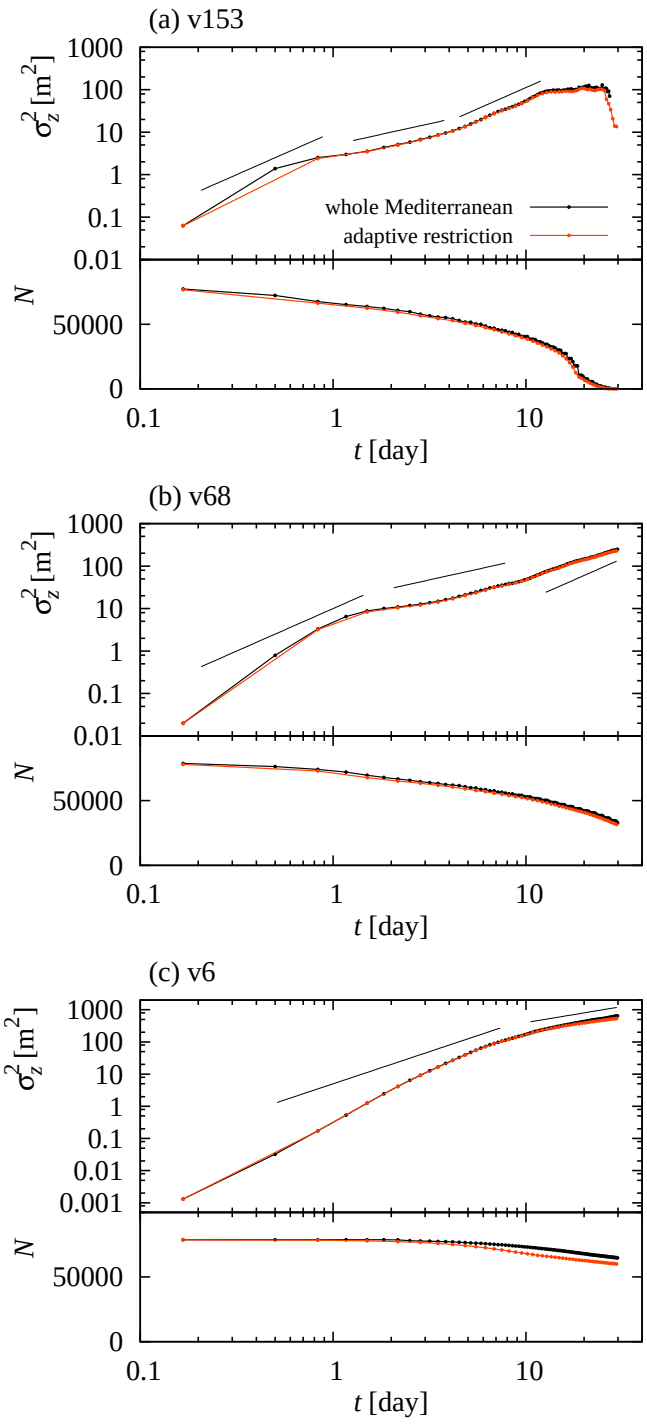

Fig. C.1 Variance of depth reached by all sinking particles (in black) and an adaptively restricted subset of them (in yellow) as a function of time. See text for details. Straight lines represent power laws for reference, with exponents 1 and 2. The number N of particles considered for the computation of the variance is also shown.

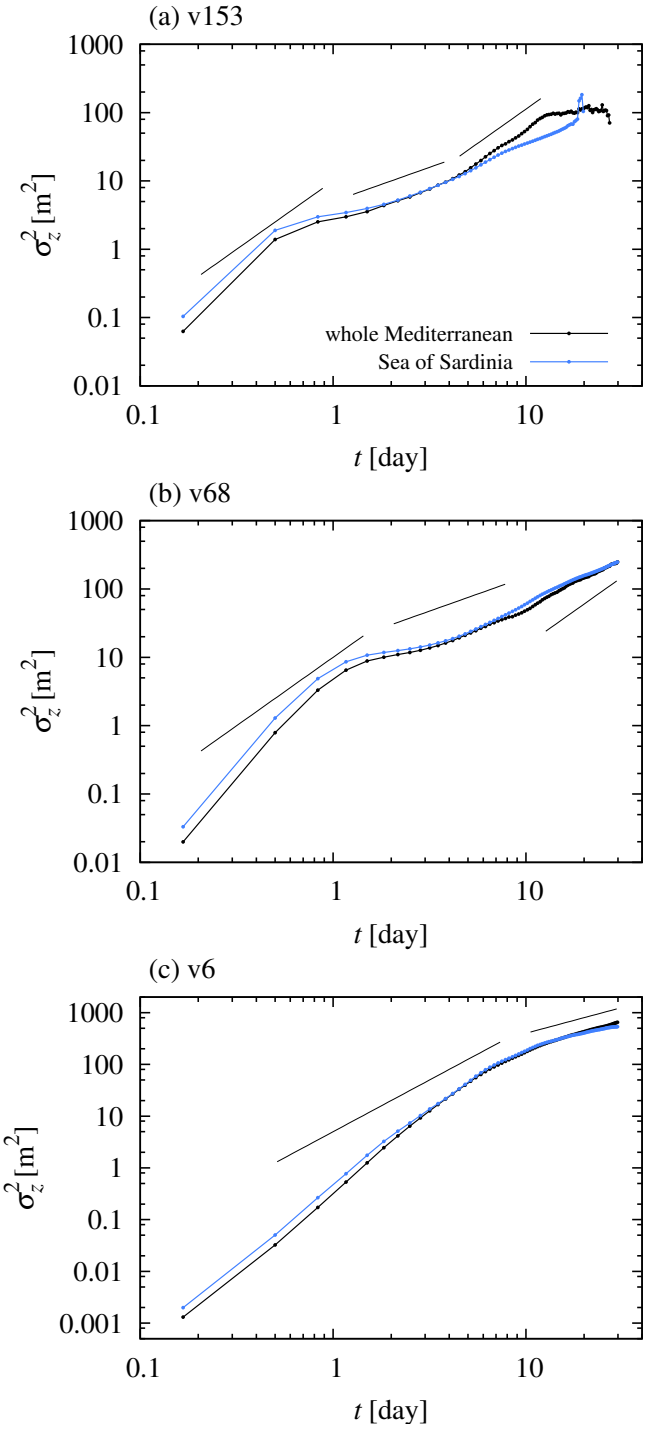

Fig. C.2 Variance of depth reached by all sinking particles (in black) and those initialized in the Sea of Sardinia (in blue; longitudes in $[5, 6.9]$ degrees, and latitudes in $[37.5, 42]$ degrees) as a function of time. See text for details. Straight lines represent power laws for reference, with exponents 1 and 2.

Appendix D

Geometric approach to the fall of an initially horizontal surface

In this Appendix we give further details on the geometry of projection and stretching that is used in the geometric approach in Chapter 3. Some of the expressions presented here were already derived or used in Refs. Drótos et al. (2019), Monroy et al. (2019), Sozza et al. (2020).

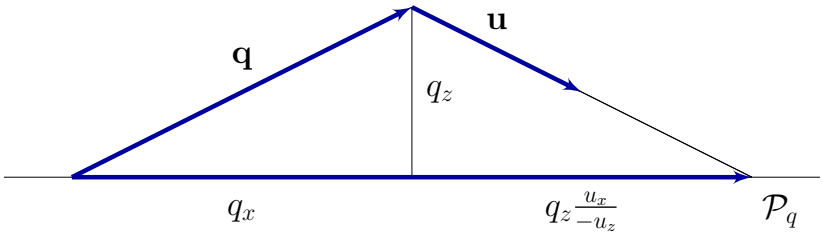

Fig. D.1 Sketch (in a two-dimensional situation) of the footprint or projection in the direction of its motion, $\mathscr{P}\mathbf{q}$, of a vector $\mathbf{q} = (q_x, q_y)$ onto a horizontal collecting layer (in fact a collecting line) when arriving there with velocity $\boldsymbol{u} = (u_x, u_y)$. We have $\mathscr{P}\mathbf{q} = (q_x - q_z u_x/u_z)\hat{\mathbf{x}}$, where $\hat{\mathbf{x}}$ is the unit vector in the direction of the collecting line.

First, we derive expressions for the footprint left by a vector $\mathbf{q}$ on the collecting layer as it arrives in it with a velocity $\boldsymbol{u}$. We will apply the expressions to vectors tangent to the falling surface at some specified point that behave as infinitesimal segments on the surface. Thus the same $\boldsymbol{u}$ applies to the whole vector: $\boldsymbol{u}$ is the velocity field at the moment t_z at which the specified point of the falling surface touches the collecting layer, and evaluated at the contact

location. Figure D.1 shows a sketch of the geometry in a two-dimensional situation, so that the components of the vector are (q_x, q_z) and those of the velocity (u_x, u_z). The horizontal projection $\mathscr{P}\mathbf{q}$ of $\mathbf{q}$ along the direction of motion, or footprint, is made of two parts, q_x and the result of multiplying q_z by the tangent of the angle between $\boldsymbol{u}$ and the vertical, i.e. $q_z u_x/(-u_z)$. Considering also the y component, the projected vector is $\mathscr{P}\mathbf{q} = (q_x - q_z u_x/u_z, q_y - q_z u_y/u_z)$ and the vertical component $(\mathscr{P}q)_z$ is zero. The projection of $\mathbf{q} = (q_x, q_y, q_z)$ onto the direction of motion is a linear operation and thus it can be expressed as the action of a matrix $\mathscr{P}$ on the vector, with

$$\mathscr{P} = \begin{pmatrix} 1 & 0 & -u_x/u_z \\ 0 & 1 & -u_y/u_z \end{pmatrix} . \tag{D.1}$$

A row of zeros can be added to the bottom if $\mathscr{P}\mathbf{q}$ is considered to be embedded in three-dimensional space. An equivalent expression for this projection operator can be written in terms of cross products:

$$\mathscr{P}\mathbf{q} = \hat{\mathbf{z}} \times \left(\mathbf{q} \times \frac{\boldsymbol{u}}{u_z} \right) , \tag{D.2}$$

where $\hat{\boldsymbol{z}}$ is the unit vector in the positive vertical direction.

Let us consider a vector of the form $\boldsymbol{\tau}(t) = \frac{d\phi_{t_0}^{\tau}(\mathbf{x}_0(s))}{ds}$, which is tangent to the falling surface at every time, and points initially (at time t_0) along the direction on the release layer specified by the parameter s. $\bar{\boldsymbol{\tau}} = \bar{\boldsymbol{J}}_{\mathscr{M}} \cdot \boldsymbol{\tau}(t_0)$ is its footprint on the collection layer. Consideration (see Fig. 3.1) of the generation of this footprint as the composition of two transformations, namely the three-dimensional stretching and transport towards the collecting surface, $\boldsymbol{\tau}(t_z) = \boldsymbol{J}_{\mathscr{M}} \cdot \boldsymbol{\tau}(t_0)$, and subsequent projection onto the horizontal along the direction of motion, $\bar{\boldsymbol{\tau}} = \mathscr{P}\boldsymbol{\tau}(t_z)$, gives the following relationship:

$$\bar{\boldsymbol{J}}_{\mathscr{M}} = \mathscr{P}\boldsymbol{J}_{\mathscr{M}} . \tag{D.3}$$

This expression can be derived more formally by applying the chain rule to Eq. (3.4), as done explicitly in Drótos et al. (2019) for the two-dimensional case. Since the singular values of $\mathscr{P}$ are $|\boldsymbol{u}|/|u_z|$ and 1, standard inequalities for singular values of products of matrices Horn and Johnson (1991) allow to show that $\bar{\Lambda}_1 \leq \Lambda_1 |\boldsymbol{u}|/|u_z|$ and $\bar{\Lambda}_1 \bar{\Lambda}_2 \leq |\boldsymbol{u}/u_z| \Lambda_1 \Lambda_2$. This last inequality is however improved by the exact equality in Eq. (3.15).

We now obtain expression (3.13) for the projection factor P entering the density factor. We first note that $\bar{\boldsymbol{\tau}}_{\boldsymbol{x}} = \mathscr{P}\boldsymbol{\tau}_x(t_z)$ and $\bar{\boldsymbol{\tau}}_{\boldsymbol{y}} = \mathscr{P}\boldsymbol{\tau}_y(t_z)$. Thus, we can elaborate the expression

for the density factor in Eq. (3.9) (we omit the time variable t_z to simplify the notation):

$$\begin{aligned}
F^{-1} &= |\bar{\boldsymbol{\tau}}_x \times \bar{\boldsymbol{\tau}}_y| = |\mathscr{P}\boldsymbol{\tau}_x \times \mathscr{P}\boldsymbol{\tau}_y| \\
&= \left| \left(\hat{\boldsymbol{z}} \times \left(\boldsymbol{\tau}_x \times \frac{\boldsymbol{u}}{u_z} \right) \right) \times \left(\hat{\boldsymbol{z}} \times \left(\boldsymbol{\tau}_y \times \frac{\boldsymbol{u}}{u_z} \right) \right) \right| \\
&= \frac{1}{u_z^2} \left| (\boldsymbol{\tau}_x(\hat{\boldsymbol{z}} \cdot \boldsymbol{u}) - \boldsymbol{u}(\hat{\boldsymbol{z}} \cdot \boldsymbol{\tau}_x) \times (\boldsymbol{\tau}_y(\hat{\boldsymbol{z}} \cdot \boldsymbol{u}) - \boldsymbol{u}(\hat{\boldsymbol{z}} \cdot \boldsymbol{\tau}_y)) \right| \\
&= \frac{1}{u_z^2} \left| (\boldsymbol{\tau}_x u_z - \boldsymbol{u}(\tau_x)_z) \times (\boldsymbol{\tau}_y u_z - \boldsymbol{u}(\tau_y)_z) \right| \\
&= \frac{1}{|u_z|} \left| u_z(\boldsymbol{\tau}_x \times \boldsymbol{\tau}_y) + (\tau_x)_z(\boldsymbol{\tau}_y \times \boldsymbol{u}) - (\tau_y)_z(\boldsymbol{\tau}_x \times \boldsymbol{u}) \right| \\
&= \left| \frac{(\boldsymbol{\tau}_x \times \boldsymbol{\tau}_y) \cdot \boldsymbol{u}}{u_z} \, \hat{\boldsymbol{z}} \right| \\
&= \left| \frac{\hat{\mathbf{n}} \cdot \boldsymbol{u}}{u_z} \right| \left| \boldsymbol{\tau}_x \times \boldsymbol{\tau}_y \right| \qquad \text{(D.4)}
\end{aligned}$$

Comparing with Eqs. (3.11) and (3.12) we identify the projection factor $P = |u_z/(\hat{\mathbf{n}} \cdot \boldsymbol{u})|$, thus demonstrating Eq. (3.13).

References

Andrady, A. L. (2015). Persistence of plastic litter in the oceans. In Bergmann, M., Gutow, L., and Klages, M., editors, *Marine Anthropogenic Litter*, pages 57–72. Springer International Publishing, Cham.

Andrady, A. L. (2017). The plastic in microplastics: A review. *Marine Pollution Bulletin*, 119(1):12 – 22.

Arístegui, J., Hernández-León, S., Montero, M. F., and Gómez, M. (2001). The seasonal planktonic cycle in coastal waters of the Canary Islands. *Scientia Marina*, 65:51–58.

Arthur, C., Baker, J., and Bamford, H. (2009). Proceedings of the international research workshop on the occurrence, effects and fate of microplastic marine debris. NOAA Technical Memorandum NOS-OR&R30.

Arístegui, J., Barton, E. D., Álvarez Salgado, X. A., Santos, A. M. P., Figueiras, F. G., Kifani, S., Hernández-León, S., Mason, E., Machú, E., and Demarcq, H. (2009). Sub-regional ecosystem variability in the Canary current upwelling. *Progress in Oceanography*, 83(1):33–48.

Arístegui, J., Sangrá, P., Hernández-León, S., Cantón, M., Hernández-Guerra, A., and Kerling, J. (1994). Island-induced eddies in the Canary islands. *Deep Sea Research Part I: Oceanographic Research Papers*, 41(10):1509–1525.

Aurell, E., Boffetta, G., Crisanti, A., Paladin, G., and Vulpiani, A. (1997). Predictability in the large: an extension of the concept of Lyapunov exponent. *Journal of Physics A: Mathematical and General*, 30(1):1–26.

Auton, T. R., Hunt, J. C. R., and Prud.Homme, M. (1988). The force exerted on a body in inviscid unsteady non-uniform rotational flow. *Journal of Fluid Mechanics*, 197:241–257.

Bagaev, A., Mizyuk, A., Khatmullina, L., Isachenko, I., and Chubarenko, I. (2017). Anthropogenic fibres in the Baltic sea water column: Field data, laboratory and numerical testing of their motion. *Science of The Total Environment*, 599-600:560 – 571.

Bakun, A. and Nelson, C. S. (1991). The seasonal cycle of wind-stress curl in subtropical eastern boundary current regions. *Journal of Physical Oceanography*, 21(12):1815 – 1834.

Balachandar, S. and Eaton, J. K. (2010). Turbulent dispersed multiphase flow. *Annu. Rev. Fluid. Mech.*, 42(1):111–133.

Balkovsky, E., Falkovich, G., and Fouxon, A. (2001). Intermittent distribution of inertial particles in turbulent flows. *Physical Review Letters*, 86(13):2790.

Ballent, A., Pando, S., Purser, A., Juliano, M. F., and Thomsen, L. (2013). Modelled transport of benthic marine microplastic pollution in the Nazaré Canyon. *Biogeosciences*, 10(12):7957–7970.

Barber, M. J. (2007). Modularity and community detection in bipartite networks. *Phys. Rev. E*, 76:066102.

Barrows, A., Cathey, S., and Petersen, C. (2018). Marine environment microfiber contamination: Global patterns and the diversity of microparticle origins. *Environmental Pollution*, 237:275 – 284.

Batchelor, G. K. (2000). An introduction to fluid dynamics.

Bergmann, M., Wirzberger, V., Krumpen, T., Lorenz, C., Primpke, S., Tekman, M. B., and Gerdts, G. (2017). High quantities of microplastic in Arctic deep-sea sediments from the Hausgarten observatory. *Environmental Science & Technology*, 51(19):11000–11010. PMID: 28816440.

Berloff, P. S. and McWilliams, J. C. (2002). Material transport in oceanic gyres. Part II: Hierarchy of stochastic models. *Journal of Physical Oceanography*, 32(3):797–830.

Bettencourt, J. H., López, C., and Hernández-García, E. (2012). Oceanic three-dimensional Lagrangian coherent structures: A study of a mesoscale eddy in the Benguela upwelling region. *Ocean Modelling*, 51:73–83.

Bettencourt, J. H., López, C., and Hernández-García, E. (2013). Characterization of coherent structures in three-dimensional turbulent flows using the finite-size Lyapunov exponent. *Journal of Physics A: Mathematical and Theoretical*, 46(25):254022.

Bettencourt, J. H., López, C., Hernández-García, E., Montes, I., Sudre, J., Dewitte, B., Paulmier, A., and Garçon, V. (2015). Boundaries of the Peruvian oxygen minimum zone shaped by coherent mesoscale dynamics. *Nature Geoscience*, 8(12):937–940.

Bettencourt, J. H., Rossi, V., Hernández-García, E., Marta-Almeida, M., and López, C. (2017). Characterization of the structure and cross-shore transport properties of a coastal upwelling filament using three-dimensional finite-size Lyapunov exponents. *Journal of Geophysical Research: Oceans*, 122(9):7433–7448.

Bettencourt, J. P. H. (2014). Three dimensional Lagrangian structures in turbulent flows: application to oceanic processes. *PhD Thesis, University of the Balearic Islands*.

Blondel, V. D., Guillaume, J.-L., Lambiotte, R., and Lefebvre, E. (2008). Fast unfolding of communities in large networks. *Journal of Statistical Mechanics: Theory and Experiment*, 2008(10):P10008.

Boffetta, G., Lacorata, G., Redaelli, G., and Vulpiani, A. (2001). Detecting barriers to transport: a review of different techniques. *Physica D: Nonlinear Phenomena*, 159(1):58–70.

Bohlin, L., Edler, D., Lancichinetti, A., and Rosvall, M. (2014). Community detection and visualization of networks with the map equation framework. In Ding, Y. and Rousseau, R., editors, *Measuring Scholarly Impact: Methods and Practice*, pages 3–34. Springer International Publishing, Cham.

Bollt, E. M. and Santitissadeekorn, N. (2013). *Applied and Computational Measurable Dynamics*. SIAM.

Bond, T., Ferrandiz-Mas, V., Felipe-Sotelo, M., and van Sebille, E. (2018). The occurrence and degradation of aquatic plastic litter based on polymer physicochemical properties: A review. *Critical Reviews in Environmental Science and Technology*, 48(7-9):685–722.

Boyd, P. W., Claustre, H., Levy, M., Siegel, D. A., and Weber, T. (2019). Multi-faceted particle pumps drive carbon sequestration in the ocean. *Nature*, 568(7752):327–335.

Buesseler, K. O., Antia, A. N., Chen, M., Fowler, S. W., Gardner, W. D., Gustafsson, O., Harada, K., Michaels, A. F., Rutgers van der Loeff, M., Sarin, M., Steinberg, D. K., and Trull, T. (2007). An assessment of the use of sediment traps for estimating upper ocean particle fluxes. *Journal of Marine Research*, 65(3):345–416.

Caldarelli, G. (2007). *Scale-free networks: complex webs in nature and technology*. Oxford University Press.

Carr, S. A. (2017). Sources and dispersive modes of micro-fibers in the environment. *Integrated Environmental Assessment and Management*, 13(3):466–469.

Cartwright, J. H. E., Feudel, U., Károlyi, G., de Moura, A., Piro, O., and Tél, T. (2010). Dynamics of finite-size particles in chaotic fluid flows. In Thiel, M., Kurths, J., Romano, M. C., Károlyi, G., and Moura, A., editors, *Nonlinear Dynamics and Chaos: Advances and Perspectives*, pages 51–87. Springer Berlin Heidelberg, Berlin, Heidelberg.

Cencini, M. and Vulpiani, A. (2013). Finite size Lyapunov exponent: review on applications. *Journal of Physics A: Mathematical and Theoretical*, 46(25):254019.

Chen, B., Li, J., and Ding, R. (2006). Nonlinear local Lyapunov exponent and atmospheric predictability research. *Science in China Series D: Earth Sciences*, 49(10):1111–1120.

Choy, C. A., Robison, B. H., Gagne, T. O., Erwin, B., Firl, E., Halden, R. U., Hamilton, J. A., Katija, K., Lisin, S. E., Rolsky, C., and Kyle, S. V. H. (2019). The vertical distribution and biological transport of marine microplastics across the epipelagic and mesopelagic water column. *Scientific reports*, 9(1):1–9.

Chubarenko, I., Bagaev, A., Zobkov, M., and Esiukova, E. (2016). On some physical and dynamical properties of microplastic particles in marine environment. *Marine Pollution Bulletin*, 108(1):105–112.

Collins, J. R., Edwards, B. R., Thamatrakoln, K., Ossolinski, J. E., DiTullio, G. R., Bidle, K. D., Doney, S. C., and Van Mooy, B. A. S. (2015). The multiple fates of sinking particles in the North Atlantic ocean. *Global Biogeochemical Cycles*, 29(9):1471–1494.

Corcoran, P. L. (2015). Benthic plastic debris in marine and fresh water environments. *Environ. Sci.: Processes Impacts*, 17:1363–1369.

Cózar, A., Echevarría, F., González-Gordillo, J. I., Irigoien, X., Úbeda, B., Hernández-León, S., Palma, Á. T., Navarro, S., García-de Lomas, J., Ruiz, A., Fernández-de Puelles, M. L., and Duarte, C. M. (2014). Plastic debris in the open ocean. *Proceedings of the National Academy of Sciences*, 111(28):10239–10244.

Cózar, A., Sanz-Martín, M., Martí, E., González-Gordillo, J. I., Ubeda, B., Gálvez, J. A., Irigoien, X., and Duarte, C. M. (2015). Plastic accumulation in the Mediterranean sea. *PLOS ONE*, 10(4):e0121762.

Danon, L., Díaz-Guilera, A., Duch, J., and Arenas, A. (2005). Comparing community structure identification. *Journal of Statistical Mechanics: Theory and Experiment*, 2005(09):P09008–P09008.

de la Fuente, R., Drótos, G., Hernández-García, E., and López, C. (2021a). Network and geometric characterization of three-dimensional fluid transport between two layers. *Phys. Rev. E*, 104:065111.

de la Fuente, R., Drótos, G., Hernández-García, E., López, C., and van Sebille, E. (2021b). Sinking microplastics in the water column: simulations in the Mediterranean sea. *Ocean Science*, 17(2):431–453.

De La Rocha, C. L. and Passow, U. (2007). Factors influencing the sinking of POC and the efficiency of the biological carbon pump. *Deep Sea Research Part II: Topical Studies in Oceanography*, 54(5):639–658.

de Madron, X. D., Castaing, P., Nyffeler, F., and Courp, T. (1999). Slope transport of suspended particulate matter on the Aquitanian margin of the Bay of Biscay. *Deep Sea Research Part II: Topical Studies in Oceanography*, 46(10):2003–2027.

Delandmeter, P. and van Sebille, E. (2019). The Parcels v2.0 Lagrangian framework: new field interpolation schemes. *Geoscientific Model Development*, 12(8):3571–3584.

Dellnitz, M., Froyland, G., and Junge, O. (2001). The algorithms behind GAIO - set oriented numerical methods for dynamical systems. In Fiedler, B., editor, *Ergodic Theory, Analysis, and Efficient Simulation of Dynamical Systems*, pages 145–174, Berlin, Heidelberg. Springer Berlin Heidelberg.

Dombre, T., Frisch, U., Greene, J. M., Hénon, M., Mehr, A., and Soward, A. M. (1986). Chaotic streamlines in the ABC flows. *Journal of Fluid Mechanics*, 167:353–391.

Douillet, P. L. (2009). Sampling distribution of the variance. In *Proceedings of the 2009 Winter Simulation Conference (WSC)*, pages 403–414. IEEE.

Dris, R., Gasperi, J., Saad, M., Mirande, C., and Tassin, B. (2016). Synthetic fibers in atmospheric fallout: A source of microplastics in the environment? *Marine Pollution Bulletin*, 104(1):290 – 293.

Drótos, G., Monroy, P., Hernández-García, E., and López, C. (2019). Inhomogeneities and caustics in passive particle sedimentation in incompressible flows. *Chaos: An Interdisciplinary Journal of Nonlinear Science*, 29(1):013115.

Eakins, B. and Sharman, G. (2010). Volumes of the world's oceans from ETOPO1. NOAA National Geophysical Data Center, Boulder,CO.

Egger, M., Sulu-Gambari, F., and Lebreton, L. (2020). First evidence of plastic fallout from the North Pacific garbage patch. *Scientific reports*, 10(1):1–10.

Enders, K., Lenz, R., Stedmon, C. A., and Nielsen, T. G. (2015). Abundance, size and polymer composition of marine microplastics $\geq 10\mu$m in the Atlantic ocean and their modelled vertical distribution. *Marine Pollution Bulletin*, 100(1):70 – 81.

Erni-Cassola, G., Gibson, M. I., Thompson, R. C., and Christie-Oleza, J. A. (2017). Lost, but found with Nile red: A novel method for detecting and quantifying small microplastics (1 mm to 20 μm) in environmental samples. *Environmental Science & Technology*, 51(23):13641–13648. PMID: 29112813.

Erni-Cassola, G., Zadjelovic, V., Gibson, M. I., and Christie-Oleza, J. A. (2019). Distribution of plastic polymer types in the marine environment; a meta-analysis. *Journal of Hazardous Materials*, 369:691–698.

Evans, P. R. (2001). Rotations and rotation matrices. *Acta Crystallographica Section D*, 57(10):1355–1359.

Everett, M. and Borgatti, S. (2013). The dual-projection approach for two-mode networks. *Social Networks*, 35(2):204–210. Special Issue on Advances in Two-mode Social Networks.

Falkovich, G., Fouxon, A., and Stepanov, M. (2002). Acceleration of rain initiation by cloud turbulence. *Nature*, 419(6903):151–154.

Faxén, H. (1922). Der widerstand gegen die bewegung einer starren kugel in einer zähen flüssigkeit, die zwischen zwei parallelen ebenen wänden eingeschlossen ist. *Annalen der Physik*, 373(10):89–119.

Filella, M. (2015). Questions of size and numbers in environmental research on microplastics: methodological and conceptual aspects. *Environmental Chemistry*, 12:527–538.

Fischer, G., Neuer, S., Ramondenc, S., Müller, T. J., Donner, B., Ruhland, G., Ratmeyer, V., Meinecke, G., Nowald, N., Klann, M., and Wefer, G. (2020). Long-term changes of particle flux in the Canary basin between 1991 and 2009 and comparison to sediment trap records off Mauritania. *Frontiers in Earth Science*, 8:280.

Fischer, V., Elsner, N. O., Brenke, N., Schwabe, E., and Brandt, A. (2015). Plastic pollution of the Kuril–Kamchatka trench area (NW Pacific). *Deep Sea Research Part II: Topical Studies in Oceanography*, 111:399 – 405.

Froyland, G. and Dellnitz, M. (2003). Detecting and locating near-optimal almost-invariant sets and cycles. *SIAM Journal on Scientific Computing*, 24(6):1839–1863.

Froyland, G., Horenkamp, C., Rossi, V., and van Sebille, E. (2015). Studying an Agulhas ring's long-term pathway and decay with finite-time coherent sets. *Chaos: An Interdisciplinary Journal of Nonlinear Science*, 25(8):083119.

Froyland, G. and Padberg, K. (2009). Almost-invariant sets and invariant manifolds - connecting probabilistic and geometric descriptions of coherent structures in flows. *Physica D: Nonlinear Phenomena*, 238(16):1507–1523.

Froyland, G., Padberg, K., England, M. H., and Treguier, A. M. (2007). Detection of coherent oceanic structures via transfer operators. *Phys. Rev. Lett.*, 98:224503.

Froyland, G., Santitissadeekorn, N., and Monahan, A. (2010). Transport in time-dependent dynamical systems: Finite-time coherent sets. *Chaos: An Interdisciplinary Journal of Nonlinear Science*, 20(4):043116.

Froyland, G., Stuart, R. M., and van Sebille, E. (2014). How well-connected is the surface of the global ocean? *Chaos: An Interdisciplinary Journal of Nonlinear Science*, 24(3):033126.

Gago, J., Carretero, O., Filgueiras, A., and Viñas, L. (2018). Synthetic microfibers in the marine environment: A review on their occurrence in seawater and sediments. *Marine Pollution Bulletin*, 127:365 – 376.

Ganser, G. H. (1993). A rational approach to drag prediction of spherical and nonspherical particles. *Powder Technology*, 77(2):143 – 152.

Gatignol, R. (1983). The Faxén formulae for a rigid particle in an unsteady non-uniform Stokes flow. *J. Mec. Theor. Appl.*, 1(1):143–160.

GEBCO Compilation Group (2020). General Bathymetric Chart of the Oceans (GEBCO) grid. doi: 10.5285/a29c5465-b138-234d-e053-6c86abc040b9.

Girvan, M. and Newman, M. E. J. (2002). Community structure in social and biological networks. *Proceedings of the National Academy of Sciences*, 99(12):7821–7826.

Goldberg, E. D. (1997). Plasticizing the seafloor: An overview. *Environmental Technology*, 18(2):195–201.

Guimerà, R., Sales-Pardo, M., and Amaral, L. A. N. (2007). Module identification in bipartite and directed networks. *Phys. Rev. E*, 76:036102.

Hailegeorgis, D., Lachkar, Z., Rieper, C., and Gruber, N. (2020). A lagrangian study of the contribution of the canary coastal upwelling to the open north atlantic nitrogen budget. *Biogeosciences Discussions*, pages 1–40.

Haller, G. (2000). Finding finite-time invariant manifolds in two-dimensional velocity fields. *Chaos: An Interdisciplinary Journal of Nonlinear Science*, 10(1):99–108.

Haller, G. (2001). Distinguished material surfaces and coherent structures in three-dimensional fluid flows. *Physica D: Nonlinear Phenomena*, 149(4):248–277.

Haller, G. (2015). Lagrangian coherent structures. *Annual Review of Fluid Mechanics*, 47(1):137–162.

Haller, G. and Sapsis, T. (2008). Where do inertial particles go in fluid flows? *Physica D: Nonlinear Phenomena*, 237(5):573–583.

Haller, G. and Yuan, G. (2000). Lagrangian coherent structures and mixing in two-dimensional turbulence. *Physica D: Nonlinear Phenomena*, 147(3):352–370.

Hardy, J. (1982). The sea surface microlayer: Biology, chemistry and anthropogenic enrichment. *Progress in Oceanography*, 11(4):307 – 328.

Haszpra, T. (2019). Intricate features in the lifetime and deposition of atmospheric aerosol particles. *Chaos: An Interdisciplinary Journal of Nonlinear Science*, 29(7):071103.

Haszpra, T. and Tél, T. (2011). Volcanic ash in the free atmosphere: A dynamical systems approach. *Journal of Physics: Conference Series*, 333:012008.

Hernández-Carrasco, I. (2013). Horizontal transport and mixing and their connection with dynamical and biologic processes in the ocean. *PhD Thesis, University of the Balearic Islands*.

Heussner, S., de Madron, X. D., Calafat, A., Canals, M., Carbonne, J., Delsaut, N., and Saragoni, G. (2006). Spatial and temporal variability of downward particle fluxes on a continental slope: Lessons from an 8-yr experiment in the Gulf of Lions (NW Mediterranean). *Marine Geology*, 234(1-4):63–92.

Hidalgo-Ruz, V., Gutow, L., Thompson, R. C., and Thiel, M. (2012). Microplastics in the marine environment: A review of the methods used for identification and quantification. *Environmental Science & Technology*, 46(6):3060–3075. PMID: 22321064.

Honjo, S., Eglinton, T. I., Taylor, C. D., Ulmer, K. M., Sievert, S. M., Bracher, A., German, C. R., Edgcomb, V., Francois, R., Iglesias-Rodriguez, M. D., et al. (2014). Understanding the role of the biological pump in the global carbon cycle: an imperative for ocean science. *Oceanography*, 27(3):10–16.

Horn, R. A. and Johnson, C. R. (1991). *Topics in Matrix Analysis*. Cambridge University Press.

Horton, A. A. and Dixon, S. J. (2018). Microplastics: An introduction to environmental transport processes. *Wiley Interdisciplinary Reviews: Water*, 5(2):e1268.

Ivar do Sul, J. A., Costa, M. F., Barletta, M., and Cysneiros, F. J. A. (2013). Pelagic microplastics around an archipelago of the equatorial Atlantic. *Marine Pollution Bulletin*, 75(1):305–309.

Jambeck, J. R., Geyer, R., Wilcox, C., Siegler, T. R., Perryman, M., Andrady, A., Narayan, R., and Law, K. L. (2015). Plastic waste inputs from land into the ocean. *Science*, 347(6223):768–771.

Jayasiri, H., Purushothaman, C., and Vennila, A. (2013). Plastic litter accumulation on high-water strandline of urban beaches in Mumbai, India. *Environmental monitoring and assessment*, 185(9):7709–7719.

Jiménez, J. (1997). Ocean turbulence at millimeter scales. *Scientia Marina*, 61(1):47–56.

Kaandorp, M. L. A., Dijkstra, H. A., and van Sebille, E. (2020). Closing the Mediterranean marine floating plastic mass budget: Inverse modeling of sources and sinks. *Environmental Science & Technology*, 54(19):11980–11989. PMID: 32852202.

Kaiser, D., Estelmann, A., Kowalski, N., Glockzin, M., and Waniek, J. J. (2019). Sinking velocity of sub-millimeter microplastic. *Marine Pollution Bulletin*, 139:214 – 220.

Kaiser, D., Kowalski, N., and Waniek, J. J. (2017). Effects of biofouling on the sinking behavior of microplastics. *Environmental Research Letters*, 12(12):124003.

Kane, I. A. and Clare, M. A. (2019). Dispersion, accumulation, and the ultimate fate of microplastics in deep-marine environments: A review and future directions. *Frontiers in Earth Science*, 7:80.

Kane, I. A., Clare, M. A., Miramontes, E., Wogelius, R., Rothwell, J. J., Garreau, P., and Pohl, F. (2020). Seafloor microplastic hotspots controlled by deep-sea circulation. *Science*, 6495:1140–1145.

Kaneko, S., Nakamura, T., Inada, F., Kato, M., Ishihara, K., Nishihara, T., and Langthjem, M. A. (2014). Chapter 8 - vibrations in fluid–structure interaction systems. In *Flow-induced Vibrations*, pages 359 – 401. Academic Press, Oxford, UK, second edition edition.

Kanhai, L. D. K., Gårdfeldt, K., Lyashevska, O., Hassellöv, M., Thompson, R. C., and O'Connor, I. (2018). Microplastics in sub-surface waters of the Arctic central basin. *Marine Pollution Bulletin*, 130:8 – 18.

Kershaw, P. and Rochman, C. (2015). Sources, fate and effects of microplastics in the marine environment: Part 2 of a global assessment. *Reports and Studies-IMO/FAO/Unesco-IOC/WMO/IAEA/UN/UNEP Joint Group of Experts on the Scientific Aspects of Marine Environmental Protection (GESAMP) Eng No. 93*.

Khatmullina, L. and Isachenko, I. (2017). Settling velocity of microplastic particles of regular shapes. *Marine Pollution Bulletin*, 114(2):871 – 880.

Kooi, M. and Koelmans, A. A. (2019). Simplifying microplastic via continuous probability distributions for size, shape, and density. *Environmental Science & Technology Letters*, 6(9):551–557.

Kooi, M., Nes, E. H. v., Scheffer, M., and Koelmans, A. A. (2017). Ups and downs in the ocean: Effects of biofouling on vertical transport of microplastics. *Environmental Science & Technology*, 51(14):7963–7971. PMID: 28613852.

Kowalski, N., Reichardt, A. M., and Waniek, J. J. (2016). Sinking rates of microplastics and potential implications of their alteration by physical, biological, and chemical factors. *Marine Pollution Bulletin*, 109(1):310 – 319.

Kukulka, T., Proskurowski, G., Morét-Ferguson, S., Meyer, D. W., and Law, K. L. (2012). The effect of wind mixing on the vertical distribution of buoyant plastic debris. *Geophysical Research Letters*, 39(7):L07601.

Kvale, K., Prowe, A., Chien, C.-T., Landolfi, A., and Oschlies, A. (2020). The global biological microplastic particle sink. *Scientific reports*, 10(1):1–12.

Lacorata, G., Aurell, E., and Vulpiani, A. (2001). Drifter dispersion in the Adriatic sea: Lagrangian data and chaotic model. *Annales Geophysicae*, 19(1):121–129.

Lancichinetti, A. and Fortunato, S. (2009). Community detection algorithms: A comparative analysis. *Phys. Rev. E*, 80:056117.

Lebreton, L., Slat, B., Ferrari, F., Sainte-Rose, B., Aitken, J., Marthouse, R., Hajbane, S., Cunsolo, S., Schwarz, A., Levivier, A., Noble, K., Debeljak, P., Maral, H., Schoeneich-Argent, R., Brambini, R., and Reisser, J. (2018). Evidence that the great Pacific garbage patch is rapidly accumulating plastic. *Scientific Reports*, 8(1):1–15.

Leith, D. (1987). Drag on nonspherical objects. *Aerosol Science and Technology*, 6(2):153–161.

Lindeque, P. K., Cole, M., Coppock, R. L., Lewis, C. N., Miller, R. Z., Watts, A. J., Wilson-McNeal, A., Wright, S. L., and Galloway, T. S. (2020). Are we underestimating microplastic abundance in the marine environment? a comparison of microplastic capture with nets of different mesh-size. *Environmental Pollution*, 265:114721.

Liu, G., Bracco, A., and Passow, U. (2018). The influence of mesoscale and submesoscale circulation on sinking particles in the northern Gulf of Mexico. *Elementa, Science of the Anthropocene*, 6:36.

Liubartseva, S., Coppini, G., Lecci, R., and Clementi, E. (2018). Tracking plastics in the Mediterranean: 2D Lagrangian model. *Marine Pollution Bulletin*, 129(1):151 – 162.

Long, M., Moriceau, B., Gallinari, M., Lambert, C., Huvet, A., Raffray, J., and Soudant, P. (2015). Interactions between microplastics and phytoplankton aggregates: impact on their respective fates. *Marine Chemistry*, 175:39–46.

M. Mancho, A., Small, D., Wiggins, S., and Ide, K. (2003). Computation of stable and unstable manifolds of hyperbolic trajectories in two-dimensional, aperiodically time-dependent vector fields. *Physica D: Nonlinear Phenomena*, 182(3):188–222.

Macias, D., Cózar, A., Garcia-Gorriz, E., González-Fernández, D., and Stips, A. (2019). Surface water circulation develops seasonally changing patterns of floating litter accumulation in the Mediterranean sea. a modelling approach. *Marine Pollution Bulletin*, 149:110619.

Madec, G. (2008). the NEMO team. *Note du Pôle de modélisation, Institut Pierre-Simon Laplace (IPSL), France, NEMO ocean engine*, 27.

Madec, G. and Imbard, M. (1996). A global ocean mesh to overcome the North Pole singularity. *Climate Dynamics*, 12(6):381–388.

Martin, J., Lusher, A., Thompson, R. C., and Morley, A. (2017). The deposition and accumulation of microplastics in marine sediments and bottom water from the Irish continental shelf. *Scientific Reports*, 7:10772.

Mason, E. (2009). *High-resolution modelling of the Canary Basin oceanic circulation*. PhD thesis, University of Las Palmas de Gran Canaria.

Maxey, M. R. and Riley, J. J. (1983). Equation of motion for a small rigid sphere in a nonuniform flow. *The Physics of Fluids*, 26(4):883–889.

McMillen, T., Xin, J., Yu, Y., and Zlatoš, A. (2016). Ballistic orbits and front speed enhancement for ABC flows. *SIAM Journal on Applied Dynamical Systems*, 15(3):1753–1782.

Meccia, V. L., Simoncelli, S., and Sparnocchia, S. (2016). Decadal variability of the turner angle in the Mediterranean sea and its implications for double diffusion. *Deep Sea Research Part I: Oceanographic Research Papers*, 114:64–77.

Melamed, D. (2014). Community structures in bipartite networks: A dual-projection approach. *PLOS ONE*, 9(5):1–5.

Michaelides, E. E. (2003). Hydrodynamic Force and Heat/Mass Transfer From Particles, Bubbles, and Drops—The Freeman Scholar Lecture . *Journal of Fluids Engineering*, 125(2):209–238.

Michels, J., Stippkugel, A., Lenz, M., Wirtz, K., and Engel, A. (2018). Rapid aggregation of biofilm-covered microplastics with marine biogenic particles. *Proceedings of the Royal Society B: Biological Sciences*, 285(1885):20181203.

Monroy, P., Drótos, G., Hernández-García, E., and López, C. (2019). Spatial inhomogeneities in the sedimentation of biogenic particles in ocean flows: Analysis in the Benguela region. *Journal of Geophysical Research: Oceans*, 124(7):4744–4762.

Monroy, P., Hernández-García, E., Rossi, V., and López, C. (2017). Modeling the dynamical sinking of biogenic particles in oceanic flow. *Nonlinear Processes in Geophysics*, 24(2):293–305.

Mountford, A. and Morales Maqueda, M. (2019). Eulerian modeling of the three-dimensional distribution of seven popular microplastic types in the global ocean. *Journal of Geophysical Research: Oceans*, 124(12):8558–8573.

Neuer, S., Freudenthal, T., Davenport, R., Llinâs, O., and Rueda, M. J. M. (2002). Seasonality of surface water properties and particle flux along a productivity gradient off NW Africa. *Deep-sea Research Part I, i-topical Studies in Oceanography*, 49:3561–3576.

Neuer, S., Ratmeyer, V., Davenport, R., Fischer, G., and Wefer, G. (1997). Deep water particle flux in the Canary island region: seasonal trends in relation to long-term satellite derived pigment data and lateral sources. *Deep Sea Research Part I: Oceanographic Research Papers*, 44(8):1451–1466.

Neufeld, Z. and Hernández-García, E. (2009). *Chemical and biological processes in fluid flows: a dynamical systems approach*. Imperial College Press, London, UK.

Newman, M. E. J. (2004a). Analysis of weighted networks. *Phys. Rev. E*, 70:056131.

Newman, M. E. J. (2004b). Fast algorithm for detecting community structure in networks. *Physical Review E*, 69(6):066133.

Newman, M. E. J. (2010). *Networks: An Introduction*. Oxford University Press.

Newman, M. E. J. and Girvan, M. (2004). Finding and evaluating community structure in networks. *Phys. Rev. E*, 69:026113.

Nooteboom, P. D., Bijl, P. K., van Sebille, E., von der Heydt, A. S., and Dijkstra, H. A. (2019). Transport bias by ocean currents in sedimentary microplankton assemblages: Implications for paleoceanographic reconstructions. *Paleoceanography and Paleoclimatology*, 34(7):1178–1194.

Nooteboom, P. D., Delandmeter, P., van Sebille, E., Bijl, P. K., Dijkstra, H. A., and von der Heydt, A. S. (2020). Resolution dependency of sinking Lagrangian particles in ocean general circulation models. *PLOS ONE*, 15(9):e0238650.

Okubo, A. (1971). Oceanic diffusion diagrams. *Deep Sea Research and Oceanographic Abstracts*, 18(8):789 – 802.

Omand, M. M., Govindarajan, R., He, J., and Mahadevan, A. (2020). Sinking flux of particulate organic matter in the oceans: Sensitivity to particle characteristics. *Scientific reports*, 10(1):1–16.

Ottino, J. M. and Ottino, J. (1989). *The kinematics of mixing: stretching, chaos, and transport*, volume 3. Cambridge university press.

Passow, U. and Carlson, C. A. (2012). The biological pump in a high CO2 world. *Marine Ecology Progress Series*, 470:249–271.

Pawlowicz, R. (2010). What every oceanographer needs to know about TEOS-10 (the TEOS-10 Primer). Available at www.TEOS-10.org.

Peacock, T. and Dabiri, J. (2010). Introduction to focus issue: Lagrangian coherent structures. *Chaos: An Interdisciplinary Journal of Nonlinear Science*, 20(1):017501.

Pedrotti, M. L., Petit, S., Elineau, A., Bruzaud, S., Crebassa, J.-C., Dumontet, B., Martí, E., Gorsky, G., and Cózar, A. (2016). Changes in the floating plastic pollution of the Mediterranean sea in relation to the distance to land. *PloS one*, 11(8):e0161581.

Pelegrí, J., Arístegui, J., Cana, L., González-Dávila, M., Hernández-Guerra, A., Hernández-León, S., Marrero-Díaz, A., Montero, M., Sangrà, P., and Santana-Casiano, M. (2005). Coupling between the open ocean and the coastal upwelling region off northwest Africa: water recirculation and offshore pumping of organic matter. *Journal of Marine Systems*, 54(1):3–37. A general study of the Spanish North Atlantic boundaries: an interdisciplinary approach.

Peng, X., Chen, M., Chen, S., Dasgupta, S., Xu, H., Ta, K., Du, M., Li, J., Guo, Z., and Bai, S. (2018). Microplastics contaminate the deepest part of the world's ocean. *Geochemical Perspectives Letters*, 9:1–5.

Poulain, M., Mercier, M. J., Brach, L., Martignac, M., Routaboul, C., Perez, E., Desjean, M. C., and Ter Halle, A. (2018). Small microplastics as a main contributor to plastic mass balance in the North Atlantic subtropical gyre. *Environmental Science & Technology*, 53(3):1157–1164.

Provenzale, A. (1999). Transport by coherent barotropic vortices. *Annual Review of Fluid Mechanics*, 31(1):55–93.

Ramasco, J. J. and Morris, S. A. (2006). Social inertia in collaboration networks. *Phys. Rev. E*, 73:016122.

Reineccius, J., Appelt, J.-S., Hinrichs, T., Kaiser, D., Stern, J., Prien, R. D., and Waniek, J. J. (2020). Abundance and characteristics of microfibers detected in sediment trap material from the deep subtropical North Atlantic ocean. *Science of The Total Environment*, 738:140354.

Reynolds, A. M. (2002). On Lagrangian stochastic modelling of material transport in oceanic gyres. *Physica D*, 172:124–138.

Riley, J. S., Sanders, R., Marsay, C., Le Moigne, F. A. C., Achterberg, E. P., and Poulton, A. J. (2012). The relative contribution of fast and slow sinking particles to ocean carbon export. *Global Biogeochemical Cycles*, 26(1).

Rosvall, M. and Bergstrom, C. T. (2008). Maps of random walks on complex networks reveal community structure. *Proceedings of the National Academy of Sciences*, 105(4):1118–1123.

Sabine, C. L., Feely, R. A., Gruber, N., Key, R. M., Lee, K., Bullister, J. L., Wanninkhof, R., Wong, C. S., Wallace, D. W. R., Tilbrook, B., Millero, F. J., Peng, T.-H., Kozyr, A., Ono, T., and Rios, A. F. (2004). The oceanic sink for anthropogenic CO2. *Science*, 305(5682):367–371.

Samelson, R. (2013). Lagrangian motion, coherent structures, and lines of persistent material strain. *Annual Review of Marine Science*, 5(1):137–163.

Samelson, R. M. and Wiggins, S. (2006). *Lagrangian transport in geophysical jets and waves: The dynamical systems approach*, volume 31. Springer Science & Business Media.

Sandulescu, M., Hernández-García, E., López, C., and Feudel, U. (2006). Kinematic studies of transport across an island wake, with application to the Canary islands. *Tellus A: Dynamic Meteorology and Oceanography*, 58(5):605–615.

Sandulescu, M., López, C., Hernández-García, E., and Feudel, U. (2007). Plankton blooms in vortices: the role of biological and hydrodynamic timescales. *Nonlinear Processes in Geophysics*, 14(4):443–454.

Sangrà, P., Pascual, A., Ángel Rodríguez-Santana, Machín, F., Mason, E., McWilliams, J. C., Pelegrí, J. L., Dong, C., Rubio, A., Arístegui, J., Ángeles Marrero-Díaz, Hernández-Guerra, A., Martínez-Marrero, A., and Auladell, M. (2009). The Canary eddy corridor: A major pathway for long-lived eddies in the subtropical North Atlantic. *Deep Sea Research Part I: Oceanographic Research Papers*, 56(12):2100–2114.

Santitissadeekorn, N., Froyland, G., and Monahan, A. (2010). Optimally coherent sets in geophysical flows: A transfer-operator approach to delimiting the stratospheric Polar vortex. *Phys. Rev. E*, 82:056311.

Seong, J. C., Mulcahy, K. A., and Usery, E. L. (2002). The sinusoidal projection: A new importance in relation to global image data. *The Professional Geographer*, 54(2):218–225.

Ser-Giacomi, E., Baudena, A., Rossi, V., Follows, M., Clayton, S., Vasile, R., López, C., and Hernández-García, E. (2021). Lagrangian betweenness as a measure of bottlenecks in dynamical systems with oceanographic examples. *Nature Communications*, 12(1):4935.

Ser-Giacomi, E., Rodríguez-Méndez, V., López, C., and Hernández-García, E. (2017). Lagrangian flow network approach to an open flow model. *The European Physical Journal Special Topics*, 226(9):2057–2068.

Ser-Giacomi, E., Rossi, V., López, C., and Hernández-García, E. (2015a). Flow networks: A characterization of geophysical fluid transport. *Chaos: An Interdisciplinary Journal of Nonlinear Science*, 25(3):036404.

Ser-Giacomi, E., Vasile, R., Hernández-García, E., and López, C. (2015b). Most probable paths in temporal weighted networks: An application to ocean transport. *Phys. Rev. E*, 92:012818.

Ser-Giacomi, E., Vasile, R., Recuerda, I., Hernández-García, E., and López, C. (2015c). Dominant transport pathways in an atmospheric blocking event. *Chaos: An Interdisciplinary Journal of Nonlinear Science*, 25(8):087413.

Shadden, S. C., Lekien, F., and Marsden, J. E. (2005). Definition and properties of Lagrangian coherent structures from finite-time Lyapunov exponents in two-dimensional aperiodic flows. *Physica D: Nonlinear Phenomena*, 212(3):271–304.

Siegel, D. and Deuser, W. (1997). Trajectories of sinking particles in the Sargasso sea: modeling of statistical funnels above deep-ocean sediment traps. *Deep-Sea Research I*, 44:1519–1541.

Solomon, O. O. and Palanisami, T. (2016). Microplastics in the marine environment: Current status, assessment methodologies, impacts and solutions. *Journal of Pollution Effects and Control*, 4:1–13.

Song, Y. K., Hong, S. H., Jang, M., Han, G. M., Jung, S. W., and Shim, W. J. (2017). Combined effects of uv exposure duration and mechanical abrasion on microplastic fragmentation by polymer type. *Environmental Science & Technology*, 51(8):4368–4376. PMID: 28249388.

Song, Y. K., Hong, S. H., Jang, M., Kang, J.-H., Kwon, O. Y., Han, G. M., and Shim, W. J. (2014). Large accumulation of micro-sized synthetic polymer particles in the sea surface microlayer. *Environmental Science & Technology*, 48(16):9014–9021. PMID: 25059595.

Soto-Navarro, J., Jordá, G., Deudero, S., Alomar, C., Amores, A., and Compa, M. (2020). 3D hotspots of marine litter in the Mediterranean: A modeling study. *Marine Pollution Bulletin*, 155:111159.

Sozza, A., Drótos, G., Hernández-García, E., and López, C. (2020). Accumulated densities of sedimenting particles in turbulent flows. *Physics of Fluids*, 32(7):075104.

Stabholz, M., Durrieu de Madron, X., Canals, M., Khripounoff, A., Taupier-Letage, I., Testor, P., Heussner, S., Kerhervé, P., Delsaut, N., Houpert, L., et al. (2013). Impact of open-ocean convection on particle fluxes and sediment dynamics in the deep margin of the Gulf of Lions. *Biogeosciences*, 10(2):1097–1116.

Stocker, T. (2014). *Climate change 2013: the physical science basis: Working Group I contribution to the Fifth assessment report of the Intergovernmental Panel on Climate Change*. Cambridge university press.

Stolle, C., Nagel, K., Labrenz, M., and Jürgens, K. (2010). Succession of the sea-surface microlayer in the coastal Baltic sea under natural and experimentally induced low-wind conditions. *Biogeosciences*, 7:2975–2988.

Suaria, G., Avio, C. G., Mineo, A., Lattin, G. L., Magaldi, M. G., Belmonte, G., Moore, C. J., Regoli, F., and Aliani, S. (2016). The Mediterranean plastic soup: synthetic polymers in Mediterranean surface waters. *Scientific reports*, 6(1):1–10.

Sulman, M. H., Huntley, H. S., Lipphardt, B., and Kirwan, A. (2013). Leaving flatland: Diagnostics for Lagrangian coherent structures in three-dimensional flows. *Physica D: Nonlinear Phenomena*, 258:77–92.

Thompson, R. C., Olsen, Y., Mitchell, R. P., Davis, A., Rowland, S. J., John, A. W., McGonigle, D., Russell, A. E., et al. (2004). Lost at sea: where is all the plastic? *Science(Washington)*, 304(5672):838.

Turner, A. and Holmes, L. (2011). Occurrence, distribution and characteristics of beached plastic production pellets on the island of Malta (central Mediterranean). *Marine Pollution Bulletin*, 62(2):377–381.

Valdés, L. and Déniz-González, I. e. (2015). Oceanographic and biological features in the Canary Current Large Marine Ecosystem. *IOC-UNESCO, Paris. IOC Technical Series*, 115(383pp).

van Cauwenberghe, L., Vanreusel, A., Mees, J., and Janssen, C. R. (2013). Microplastic pollution in deep-sea sediments. *Environmental Pollution*, 182:495 – 499.

van Sebille, E., Aliani, S., Law, K. L., Maximenko, N., Alsina, J. M., Bagaev, A., Bergmann, M., Chapron, B., Chubarenko, I., Cózar, A., Delandmeter, P., Egger, M., Fox-Kemper, B., Garaba, S. P., Goddijn-Murphy, L., Hardesty, B. D., Hoffman, M. J., Isobe, A., Jongedijk, C. E., Kaandorp, M. L. A., Khatmullina, L., Koelmans, A. A., Kukulka, T., Laufkötter, C., Lebreton, L., Lobelle, D., Maes, C., Martinez-Vicente, V., Maqueda, M. A. M., Poulain-Zarcos, M., Rodríguez, E., Ryan, P. G., Shanks, A. L., Shim, W. J., Suaria, G., Thiel, M., van den Bremer, T. S., and Wichmann, D. (2020). The physical oceanography of the transport of floating marine debris. *Environmental Research Letters*, 15(2):023003.

Van Sebille, E., Spathi, C., and Gilbert, A. (2016). The ocean plastic pollution challenge: towards solutions in the UK. *Grant. Brief. Pap*, 19:1–16.

van Sebille, E., Wilcox, C., Lebreton, L., Maximenko, N., Hardesty, B. D., van Franeker, J. A., Eriksen, M., Siegel, D., Galgani, F., and Law, K. L. (2015). A global inventory of small floating plastic debris. *Environmental Research Letters*, 10(12):124006.

Vannitsem, S. (2017). Predictability of large-scale atmospheric motions: Lyapunov exponents and error dynamics. *Chaos: An Interdisciplinary Journal of Nonlinear Science*, 27(3):032101.

Vidal, A. S., Pasqual, C., Kerhervé, P., Heussner, S., Calafat, A., Palanques, A., Durrieu de Madron, X., Canals, M., and Puigc, P. (2009). Across margin export of organic matter by cascading events traced by stable isotopes, northwestern Mediterranean sea. *Limnology and Oceanography*, 54(5):1488–1500.

Voth, G. A. and Soldati, A. (2017). Anisotropic particles in turbulence. *Annual Review of Fluid Mechanics*, 49(1):249–276.

Wichmann, D., Delandmeter, P., and van Sebille, E. (2019). Influence of near-surface currents on the global dispersal of marine microplastic. *Journal of Geophysical Research: Oceans*, 124(8):6086–6096.

Wiggins, S. (2005). The dynamical systems approach to lagrangian transport in oceanic flows. *Annual Review of Fluid Mechanics*, 37(1):295–328.

Wiggins, S. (2013). *Chaotic transport in dynamical systems*, volume 2. Springer Science & Business Media.

Woodall, L. C., Sanchez-Vidal, A., Canals, M., Paterson, G. L., Coppock, R., Sleight, V., Calafat, A., Rogers, A. D., Narayanaswamy, B. E., and Thompson, R. C. (2014). The deep sea is a major sink for microplastic debris. *Royal Society Open Science*, 1(4):140317.

Wooster, W., Bakun, A., and McLain, D. (1976). Seasonal upwelling cycle along the eastern boundary of the North Atlantic. *Journal of Marine Research*, 34(2):131–141.

Wright, S., Ulke, J., Font, A., Chan, K., and Kelly, F. (2020). Atmospheric microplastic deposition in an urban environment and an evaluation of transport. *Environment International*, 136:105411.

Wright, S. L., Rowe, D., Thompson, R. C., and Galloway, T. S. (2013a). Microplastic ingestion decreases energy reserves in marine worms. *Current Biology*, 23(23):R1031–R1033.

Wright, S. L., Thompson, R. C., and Galloway, T. S. (2013b). The physical impacts of microplastics on marine organisms: A review. *Environmental Pollution*, 178:483–492.

Ye, S. and Andrady, A. L. (1991). Fouling of floating plastic debris under Biscayne Bay exposure conditions. *Marine Pollution Bulletin*, 22(12):608–613.

Zhou, T., Ren, J., Medo, M. c. v., and Zhang, Y.-C. (2007). Bipartite network projection and personal recommendation. *Phys. Rev. E*, 76:046115.

Álvarez Salgado, X., Labarta, U., Fernández-Reiriz, M., Figueiras, F., Rosón, G., Piedracoba, S., Filgueira, R., and Cabanas, J. (2008). Renewal time and the impact of harmful algal blooms on the extensive mussel raft culture of the Iberian coastal upwelling system (SW Europe). *Harmful Algae*, 7(6):849–855.

Álvaro Peliz, Rosa, T. L., Santos, A. P., and Pissarra, J. L. (2002). Fronts, jets, and counter-flows in the Western Iberian upwelling system. *Journal of Marine Systems*, 35(1):61–77.